

Aus dem Medizinischen Zentrum für Radiologie
Sektion für Medizinische Physik
Geschäftsführender Direktor: Prof. Dr. K. J. Klose
des Fachbereichs Medizin der Philipps-Universität Marburg
In Zusammenarbeit mit dem Universitätsklinikum Gießen und Marburg GmbH,
Standort Marburg

Clinical Dosimetry in Photon Radiotherapy – a Monte Carlo Based Investigation

Inaugural Dissertation
zur Erlangung des Doktorgrades der Humanbiologie
(Dr. rer. physiol.)

dem Fachbereich Medizin der Philipps-Universität Marburg
vorgelegt von

Jörg Wulff
aus München

Marburg, 2010

für Klemens

Angenommen vom Fachbereich Medizin der Philipps-Universität Marburg
am 15.01.2010

Gedruckt mit der Genehmigung des Fachbereichs

Dekan: Prof. Dr. M. Rothmund

Referent: Prof. Dr. Dr. J. T. Heverhagen

Korreferent: Prof. Dr. Dr. G. Kraft (Darmstadt)

Prüfungsausschuss:

Prof. Dr. H. Schäfer

Prof. Dr. Dr. J. T. Heverhagen

Prof. Dr. H. J. Jansch (Fachbereich Physik)

Contents

1. INTRODUCTION AND THEORETICAL FOUNDATION	8
1.1. Necessity for Improving Accuracy in Dosimetry	8
1.2. Outline	9
1.3. Physics of Ionizing Radiation	10
1.3.1. Electron and Positron Interactions	10
1.3.2. Photon Interactions	11
1.3.3. Definition of Dosimetric Quantities	12
1.4. Clinical Radiation Dosimetry	14
1.4.1. General Concepts	14
1.4.2. Ionization Chamber Dosimetry	16
1.4.3. Cavity Theory	17
1.4.4. Dosimetry Protocols	21
1.4.5. Non-Reference Conditions	23
1.4.6. Other Types of Detectors	25
1.5. Monte Carlo Simulations of Radiation Transport	26
1.5.1. General Introduction and Historical Background	26
1.5.2. The EGSnrc Code System	27
1.5.3. Simulation of Photon and Electron Transport	28
1.5.4. Variance-Reduction Techniques - General Concepts	29
1.5.5. Ionization Chamber Calculations	31
1.5.6. Simulation of Linear Accelerators	33
2. METHODS FOR INVESTIGATION OF DOSIMETRY	37
2.1. Increasing Efficiency	37
2.1.1. Ionization Chamber Calculations in Photon Beams	37
2.1.2. Fast kerma-Based Calculations	44
2.1.3. Parallel Computing with the EGSnrc Monte Carlo Code	46
2.2. Ionization Chamber Calculations for Reference Dosimetry	46
2.2.1. Photon Spectra	46
2.2.2. Calculation of Perturbation and Beam-Quality Correction Factors	47
2.2.3. Uncertainty Estimation for Calculated Correction Factors	51
2.3. Ionization Chambers under Non-Reference Conditions	53
2.3.1. Modeling a Linear Accelerator Head	54
2.3.2. Ionization Chamber in the 6 MV Field of a Linear Accelerator	57
2.3.3. Ionization Chambers and Other Detectors Under Charged Particle Dis-Equilibrium in the Penumbra of a Photon Beam	57
3. RESULTS AND DISCUSSION	60
3.1. Increasing Efficiency	60
3.1.1. Ionization Chamber Related Calculations in Photon Beams	60
3.1.2. Fast kerma-Based Calculations	63

3.2. Calculations for Reference Dosimetry	63
3.2.1. Perturbation Factors	64
3.2.2. Uncertainty-Estimation for Calculated Correction Factors	73
3.2.3. Summary	77
3.3. Non-Reference Conditions	77
3.3.1. Modeling the Siemens KD Linear Accelerator	77
3.3.2. Ionization Chambers in the 6 MV Field of a Linear Accelerator	83
3.3.3. Charged Particle Dis-Equilibrium in the Penumbra	87
3.3.4. Summary	93
4. SUMMARY AND CONCLUSION	94
5. Abstract	97
6. Zusammenfassung	99
A. Einführung zur Monte-Carlo Simulation von Strahlungstransport	101
Bibliography	123
List of Tables	124
List of Figures	125
List of Abbreviations	127
Danksagung	I
Publikationsliste	II

1. INTRODUCTION AND THEORETICAL FOUNDATION

1.1. Necessity for Improving Accuracy in Dosimetry

Radiotherapy as an important form of cancer treatment aims at the eradication of tumour cells with the use of ionizing radiation. A consistent quality assurance procedure is mandatory to ensure the accurate dose delivery to a tumour volume and to avoid any unnecessary harm to normal tissue. A central point of quality assurance is the exact knowledge of the delivered radiation dose to the patient.

The tumour control and the normal tissue complication probability have a sigmoidal dependence on radiation dose. A hypothetical dose effect relation is schematically shown in figure 1.1. The characteristic dose effect curves for tumour control and normal tissue complication with their steep gradients require the accurate knowledge of dose to the patient. Any uncertainty on delivered dose may either result in an underdosage of the tumour or a complication for normal tissue. The generally accepted total uncertainty, which needs to be maintained in radiotherapy, amounts to 5% and includes all uncertainties of the dose delivery process (Papanikolaou et al., 2004).

There is a large variation in the reported slopes in the dose effect curves, but it has been reported that even a 1% dose accuracy improvement can result in a 2% increase in cure rate for early stage tumours (Boyer and Schultheiss, 1988). Besides the quality of an individual treatment, any attempt to improve the knowledge of dose effect relations, based on epidemiological studies, will require a reduced uncertainty in the dose delivered during radiation treatment.

One crucial contribution to the overall uncertainty is the determination of dose under reference conditions in a clinical therapy beam and is currently expected to be $\sim 2\%$ (1 standard deviation). A reduction to 1% is aimed at for the future (Papanikolaou et al., 2004). The origin of this uncertainty can be retraced to theories of ionization chamber dosimetry applied in the current protocols and the data presently available.

Modern radiation techniques employing small fields such as stereotactic radiotherapy provide good conformity to tumour volumes and allow sparing of organs at risk. In intensity modulated radiation therapy (IMRT) non-uniform fields are composed of many small elementary fields and a larger part of total dose to the patient is delivered in these small field segments (Bortfeld, 2006). The application of these advanced radiotherapy techniques challenges the established protocols for dosimetry under reference conditions while aiming at the highest precision. Generally it is questionable if the mentioned $\sim 2\%$ uncertainty holds for dosimetry under non-reference conditions with the application of current dosimetry concepts.

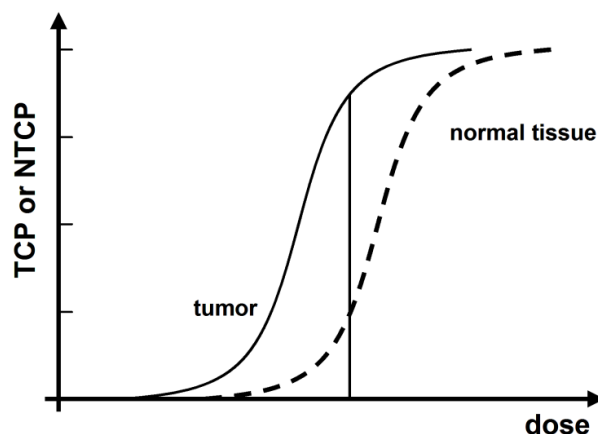


Figure 1.1.: Schematic illustration of tumour control probability (TCP) and the probability of normal tissue complication (NTCP) as a function of dose. The vertical line indicates a certain dose in the steep part of both effects responding to dose. Uncertainties in delivered dose might worsen the clinical outcome due to either reduction of TCP or increase of NTCP.

1.2. Outline

Starting with some general and brief introduction to the physics of ionizing radiation, the concepts of clinical ionizing radiation are presented in chapter 1. This chapter also gives an introduction to the numerical Monte Carlo methods for the simulation of radiation transport and their application to calculations for clinical dosimetry.¹ In chapter 2 the developed methods for the efficient simulation of ionization chamber dosimetry are introduced. The methodology for the simulation of a clinical linear accelerator model is explained. Chapter 3 presents and discusses the results of the investigation of ionization chamber dosimetry under reference and a comparison to existing data in dosimetry protocols. An analysis of systematic uncertainties is presented. The development of a linear accelerator model and its validation is described. The calculations under non-reference dosimetry in the field of the linear accelerator model as well as in idealized conditions of charged particle dis-equilibrium are presented. A general conclusion and summary is given in chapter 4.

¹Please note that a more detailed introduction to Monte Carlo simulations of radiation transport is given in the appendix (in German language).

1.3. Physics of Ionizing Radiation

In the following some basic principles and quantities in the context of ionizing radiation are given. This is not intended to be complete review, it rather serves as a brief introduction that covers the topics needed in the later chapters. For more details the reader is referred to appropriate textbooks, e.g. Attix (2004), Podgorsak (2006) or Reich (1990).

1.3.1. Electron and Positron Interactions

When charged particles² pass medium they interact with the absorber atoms through Coulomb interactions with atoms' nuclei and orbital electrons. Collisions may be elastic when only a change of direction occurs or inelastic when further energy is transferred. Types of interaction can be distinguished.

- electron-orbital electron (collisional) interactions, where ionization with ejection of the orbital-electron or excitation of the absorber atom follows; ejected electrons carrying enough energy for traveling a certain distance away from the point of interaction are called δ - or *knock-on* electrons; the ionized atom will return to its ground state with the emission of characteristic x-rays or Auger-electrons
- electron-orbital and electron-nucleus (radiative) interaction, where scattering and energy loss by production of radiative photons (Bremsstrahlung) results
- soft interaction with the whole atom, where virtually none or only a small amount of energy is lost, still being the most numerous type of interaction

Energy losses per unit length x are described by the stopping powers $S = dE/dx$ of a material, or more frequently used as mass stopping power S/ρ with medium's density ρ . The total stopping power consists of collisional and radiative contributions (see above). The radiative photons travel far before being absorbed and as will be discussed below (see eq. 1.5) local absorbed dose is directly proportional to the collisional part of the stopping powers. A brief look at the underlying equation for the description of the collisional stopping powers S_{col} for electrons and positrons is helpful for later discussions. Following ICRU Report No.37 (ICRU, 1984) S_{col} is given by

$$\frac{S_{col}}{\rho} = \frac{2\pi r_e^2 m c^2}{u} \frac{1}{\beta^2} \frac{Z}{A} \left[\ln(E/I)^2 + \ln(1 + \tau/2) + F^\pm(\tau) - \delta \right] \quad (1.1)$$

where r_e is the classical electron radius, m is the mass of the electron, c is the velocity of light, u is the atomic mass, β is the ratio of particle velocity to the velocity of light, Z is the atomic number. A is the atomic weight, E is the kinetic energy of the electron, I is the mean excitation energy of the absorber atom, F^\pm is an auxiliary function for electrons (-) and positrons (+), τ is the ratio of kinetic energy E of the electron to its rest energy and δ is density-effect correction.

²In the context of photon dosimetry, charged particles are considered to be electrons or positrons. Within the following no distinction between electrons and positrons is drawn, i.e. electrons are used as a synonym for both.

Except for some simple atomic gases, the mean excitation energy I is determined from experimental data. Thus, it cannot be calculated directly and the value of the stopping power underlies some measurement uncertainties (ICRU, 1984), a fact that must be kept in mind for the calculations based on these data. The density-effect reduces the collisional stopping power by polarization of the medium due to fast electrons. The electromagnetic Coulomb-field acting between the electron and atoms distant from the electron track is reduced in dense media. This effect depends on the density of the material and further on the energy of the electron. Different models for the calculation of the density-effect exist and thus the stopping powers depend on these calculations (ICRU, 1984), causing another source of uncertainty for the value of S_{col} .

Due to the finite range of created δ -electrons the *restricted collisional stopping power* L is introduced. It defines the energy loss per unit length in excitation and ionization, where the energy transferred is smaller than a chosen limit Δ . Hence Δ corresponds to a certain vicinity of the electron's track, where energy is absorbed.

Range of electrons

The range of electrons varies stochastically, depending on individual interactions taking place. One analytical concept for range estimation (different from depth of penetration) is the "continuous slowing down approximation" (CSDA), where the range R is calculated by integrating the reciprocal total stopping power S

$$R_{CSDA} = \int_0^{E_0} \left(\frac{S}{\rho} \right)^{-1} dE \quad (1.2)$$

The actual range of electrons will usually be somewhat smaller (see chapter 3.2.1.5), since discrete creation of secondary particles with certain energy occurs. The *depth of penetration* is further decreased due to the curved trajectories of an electron scattered in medium.

1.3.2. Photon Interactions

For the energies applied in radiotherapy, photons may undergo coherent (Rayleigh) scattering, photoelectric absorption, incoherent (Compton) scattering or production of an electron/positron pair in the electromagnetic field of atoms. The number of photons passing a certain thickness of media is decreased exponentially by these interactions.

The photoelectric effect results when a photon interacts with a tightly bound electron (binding energy in the range of the photon's energy). The photon disappears while the atomic electron is ejected, carrying a kinetic energy equal to the energy of the incident photon, decreased by the binding energy. As a result, the atom left in excited state with a vacancy in the ionized shell, relaxes with the emission of fluorescent photons (or Auger-electrons). In the case of Rayleigh scattering no energy is transferred between the initial photon and the bound orbital electron. Still it has a contribution to the total attenuation of a photons beam. The Compton effect occurs between a photon and an essentially free electron (binding energy much smaller than energy of incident photon). The photon loses a part of its energy and a recoil electron is ejected from the atom shell. In the pair

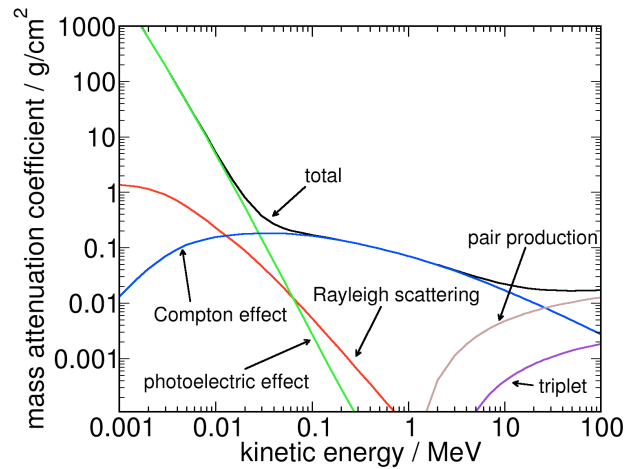


Figure 1.2.: Photon mass attenuation coefficient for water as a function of energy. The contributions of individual interaction types are shown. Data is taken from the XCOM data base (Berger et al., 1999).

production process the photon disappears when an electron/positron pair is created in the nuclear Coulomb field with kinetic energy of the photons energy minus two times the electrons/positrons rest mass of 511 keV. If the energy is more than four times the rest mass, a pair production might occur in the field of orbital electrons. This process is called triplet production, since three particles are resulting (electron/positron plus the orbital electron). At energies above 10 MeV photo nuclear reactions can occur, when the high energy photon is absorbed by the nucleus of an atom, resulting in the emission of a neutron or proton.

The probability for the occurrence of the single processes and the resulting change of energy and direction of created particles and the incident photon is governed by the differential cross sections. They depend on the atomic number of the medium and the energy of the photon and are based on theoretical or semi-empirical values (Hubbell, 2006). The total cross section μ sums the coefficients of the individual interactions, usually ignoring the minor contribution due to the mentioned photo nuclear reactions. In figure 1.2 the mass attenuation coefficient for water is shown including the contribution of single interaction mechanisms.

1.3.3. Definition of Dosimetric Quantities

1.3.3.1. Kerma

Photons as indirectly ionizing radiation transfer energy dE_{tr} to secondary charged particles, which subsequently release their energy in the medium with a mass dm . A conceptual description of this first step of liberating kinetic energy is given by the quantity *kerma* “kinetic energy relaxed per unit mass” (Attix, 2004; Loevinger, 1981). It is easily connected to the fluence Φ of photons of energy E and the mass-energy transfer coefficient μ_{tr}

$$K = \frac{dE_{tr}}{dm} = \Phi \cdot E \cdot \frac{\mu_{tr}}{\rho} \quad (1.3)$$

The quantity is given in J/kg and is denoted as Gy^3 . For a polyenergetic spectrum of photons the kerma is the sum of all fluence contributions differential in energy and the corresponding energy transfer coefficients. The concept of kerma does not concern as to what happens with this energy after it is released. Taking only the fraction of energy into account, which leads to local⁴ energy depositions corrected for energy-losses due to Bremsstrahlung (radiative fraction \bar{g}), equation 1.3 with μ_{en} as the energy absorption coefficient becomes

$$K_{col} = \Phi \cdot E \cdot \frac{\mu_{en}}{\rho} = \Phi \cdot E \cdot \frac{\mu_{tr}}{\rho} \cdot (1 - \bar{g}) \quad (1.4)$$

and describes the part of kerma resulting from collisions of created secondary electrons.

1.3.3.2. Absorbed Dose and Charged-Particle Equilibrium

The absorbed dose in medium D_{med} is connected to the electron fluence spectrum⁵ Φ_E in the medium as

$$D_{med} = \Phi \left(\frac{\bar{S}_{col}}{\rho} \right)_{med} \quad (1.5)$$

with the averaged collisional stopping power of the medium $\left(\frac{\bar{S}_{col}}{\rho} \right)_{med}$ and is given in Gy .

For a primary photon beam, the fluence of electrons is given by all secondary electrons liberated in the neighbourhood of the point of interaction. Due to the range of electrons, absorbed dose cannot uniquely be described by the photon fluence as in the case of kerma (see above). Still, a ratio $\beta = D/K_{col}$ between dose and the collisional part of kerma can be defined. Figure 1.3 illustrates the relationship. In the hypothetical situation where charged particle equilibrium (CPE) is established and no photon attenuation occurs β equals unity. CPE exists in a volume, if each charged particle of given energy leaving the volume is replaced by an identical particle. For a primary photon beam this situation would be achieved at the depth beyond the maximum range of secondary electrons along the direction of primary photons. Due to the attenuation of photons in reality, a complete CPE is never achieved, but a transient CPE (TCPE) can be defined with $\beta > 1$.

According to Attix (2004) the dose under TCPE can be expressed as

$$D \stackrel{TCPE}{=} K_{col} \cdot e^{\mu' \bar{x}} \quad (1.6)$$

where μ' is the common slope of D and K_{col} and \bar{x} is the mean range of the secondary electrons along the direction of the primary photon. If the slope of the collision kerma

³The unit *Gray* is named after the British Physicist Louis Harold Gray (1905-1965).

⁴Due to the range of electrons the term *local* is rather ambiguous, but distinguished from the far-reaching Bremsstrahlung.

⁵Even for initial monoenergetic electrons a spectrum results as it is slowing down within the medium.

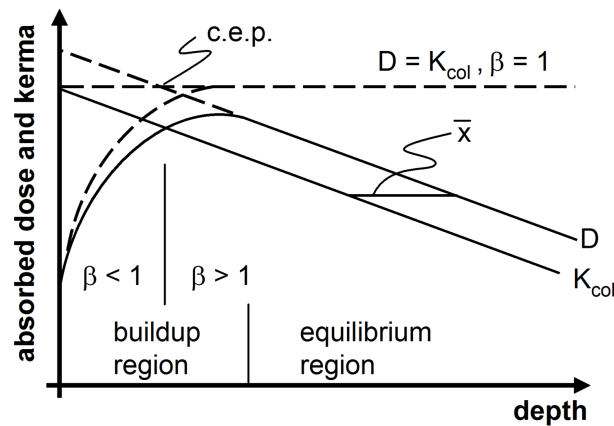


Figure 1.3.: Illustration of the relationship between absorbed dose D and collisional kerma K_{col} . A photon beam enters the medium from the left. The buildup region spans from the surface to a depth larger than the maximum range of secondary electrons. If no attenuation of primary photons is assumed the electronic or charged particle equilibrium (CPE) is reached and $\beta = 1$ (dashed line). Otherwise kerma and dose are attenuated exponentially (solid curves) and transient CPE (TCPE) is achieved. In the TCPE and depth-dose beyond the effective center of electron production (c.e.p.) D is larger than K_{col} and thus $\beta > 1$. \bar{x} is the mean range of electrons transporting energy in the direction of the primary beam. Based on Loevinger (1981).

and dose as a function of depth are equal, the ratio of kerma and dose is independent of depth and a systematic shift of both curves results (see fig. 1.3).

For a beam of finite size the CPE is also disturbed at the field boundaries. Due to their *lateral* range, electrons carry some energy out of the field even where no primary photons exist, the range of electrons being dependent on their kinetic energy.

1.4. Clinical Radiation Dosimetry

1.4.1. General Concepts

The estimation of dose to the patient involves several steps. Usually calibrated ionization chambers, whose calibration coefficient can be traced back to national standard laboratories⁶, are used for dosimetry in a clinic. In external beam radiotherapy, linear accelerators (linacs) are applied for treatment and their output needs to be known to enable the delivery of a specified dose to a reference point per monitor unit. The procedures for reference dosimetry are specified in national and international “dosimetry protocols” or “codes of practice” (Andreo et al., 2001; Almond et al., 1999; DIN6800-2, 2008). The estimation

⁶The Physikalisch-Technische Bundesanstalt in Braunschweig (PTB) fulfills Germany’s obligations for a national primary standard laboratory.

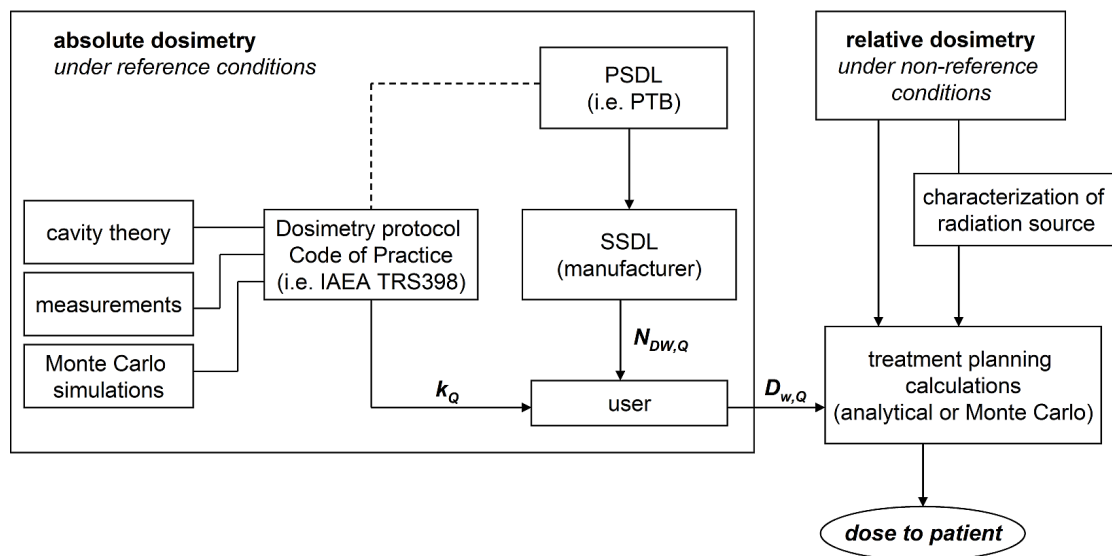


Figure 1.4.: Concept of clinical dosimetry in radiation therapy. Explanation is given in the text.

of individual dose distributions to the patient during treatment is based on calculation models of treatment planning systems. These are connected to the measured dose value under the mentioned reference conditions. Validation and commissioning of any planning system is based on upon measurements of dose distributions from the linac under various conditions.

The general concept of clinical dosimetry in the context of radiation therapy is illustrated in figure 1.4. Two procedures can be distinguished, namely *absolute* (or *reference dosimetry*) and *relative dosimetry*. The former summarizes the steps needed to determine the absolute dose in terms of dose to water D_w under well defined reference conditions. The user employs ionization chambers, calibrated at a secondary standard laboratory (SSDL), which is usually the manufacturer itself. The corresponding calibration coefficient $N_{D,w}$ is traceable to a primary standard laboratory. Usually this national institution is at least in parts involved in the national definition of dosimetry protocols. The dosimetry protocols deliver data for the necessary beam quality correction factors k_Q which are needed since the calibration beam quality generally differs from the quality of the user's beam. The data for the beam quality correction factor k_Q is based on theories describing the measurement of dose, on measurements and possibly on Monte Carlo simulations.

Besides its necessity in recurrent quality assurance measurements, relative dosimetry is needed for the characterization of the treatment machine as a radiation source. Treatment planning systems use the results of absolute and relative dosimetry for the calculation of dose to the patient, either being based on analytical or on direct Monte Carlo calculations.

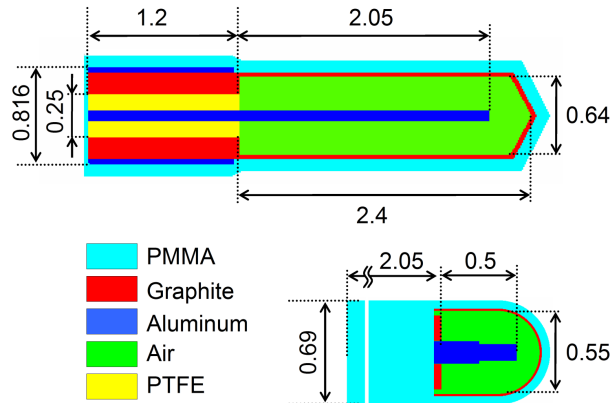


Figure 1.5.: cross section through models of typical thimble chambers: NE2571 Farmer chamber (top) with a sensitive air volume of 0.6 cm^3 and PTW31010 'semi-flex' (bottom) with 0.125 cm^3 . The air volume is surrounded by the chamber wall and stem construction. PMMA is poly-methyl-methacrylate and PTFE is teflon. Dimensions are given in cm.

1.4.2. Ionization Chamber Dosimetry

In principle any physical direct or indirect effect of ionizing radiation can be used to determine the absorbed dose in medium. These effects might be ionizing of gas or solids, emission of light, blackening of photographic film or some chemical change. Calorimetry, which connects the heat increase resulting from radiation energy absorption to absorbed dose, is a direct and precise method for dose measurement, but requires strictly controlled measurement conditions.

The commonly used detectors in clinical radiation dosimetry are air-filled ionization chambers, which are inexpensive, provide reproducibly a direct reading and are able to precisely measure the absorbed dose under certain defined conditions. The transfer of energy during interactions of radiation with the air molecules inside the chamber results in ion pairs, which can be quantified in terms of an electric current measured by an electrometer. This current arises in the high voltage electric field between two electrodes of the chamber. Generally two different designs are used in clinical dosimetry to form these two electrodes: parallel or cylindrical. A plane parallel chamber consists of two separated electrodes parallel to each other and perpendicular to the primary beam direction, leaving an air-filled gap in between, which serves as the sensitive volume. This type of chamber is usually recommended for high energy electron dosimetry. In photon dosimetry cylindrically shaped ionization chambers (also known as thimble or compact chambers) are used. They consist of a cylindrical air volume with a central electrode inside and a surrounding cylindrical wall perpendicular to the primary beam direction (see fig. 1.5).

Knowing the energy needed to create an ion pair in air W_{air} , the volume of the cavity V and the density of the gas ρ , the dose to the detector's cavity D_c is given by the value of the total charge Q_{ion} of the ions of one sign created in the air cavity:

$$D_c = \frac{Q_{ion}}{\rho V} \cdot \frac{W_{air}}{e} \quad (1.7)$$

Under the assumption that proportionality exists, a factor f can be introduced to determine the desired dose to a point in the undisturbed medium (usually water) the detector is placed in (Nahum, 1996). This leads to

$$D_w = f \cdot D_c \quad (1.8)$$

where D_w is the dose to water. The *cavity theory* is used to evaluate and describe the factor f and will be explained in the next section.

1.4.3. Cavity Theory

As stated above, the relationship between dose to water and the dose in the air cavity of an ionization chamber can be expressed by a single factor. This theoretical relation was developed by Bragg and Gray in the 1950's. The idealized concept requires the cavity to be small enough not to perturb the fluence of (secondary) electrons crossing it, requiring small dimensions compared to the range of electrons. Further, no photon interactions may occur within the cavity, hence only charged particles entering the idealized cavity contribute to the dose absorbed in it, referred to as D_a . With equation 1.5 and a constant fluence Φ of electrons in the water and air, the ratio of doses is simply given by

$$\frac{D_w}{D_a} = \frac{\Phi \left(\frac{\bar{S}}{\rho}\right)_w}{\Phi \left(\frac{\bar{S}}{\rho}\right)_{air}} = \frac{\left(\frac{\bar{S}}{\rho}\right)_w}{\left(\frac{\bar{S}}{\rho}\right)_{air}} \quad (1.9)$$

with the mass collisional stopping powers averaged over the whole spectrum. The Bragg-Gray conditions demand an equilibrium of all electrons including δ -electrons created by hard collisions, which implies no creation or absorption of these electrons inside the cavity. Alternatively this condition might be fulfilled for real chambers by adding a thin air equivalent layer (e.g. graphite) to the inner wall of the ionization chamber (Reich, 1990), which creates the state of δ -electron equilibrium.

Another way was proposed by Spencer and Attix (1955b,a) who extended the Bragg-Gray theory to account for created δ -electrons and their potential energy deposition within the calculated average stopping-power ratios (sprs). For calculation of sprs they divided the electrons up into two groups discriminated by the cut-off energy Δ :

- *fast* electrons with kinetic energies larger Δ traversing the cavity and depositing energy in collisions limited to Δ ; for energy depositions larger Δ the created electrons are considered as part of the electron spectrum
- *slow* electrons with energies less than Δ that are unable to cross the cavity and thus depositing energy on the spot

Nahum (1978) extended the theory taking the 5-10 % of dose deposition into account, which is caused by electrons, which fall below Δ while passing the cavity. Including these "track-ends", the Spencer-Attix stopping-power ratios (corresponding to f in

equation 1.8) relate the ratio of doses in the cavity and the surrounding medium, caused by fluence of electrons differential in energy:

$$\frac{D_w}{D_a} = s_{w,a}^\Delta = \frac{\int_{\Delta}^{E_{max}} \Phi_{E,w} \left(\frac{L}{\rho}\right)_{\Delta,w} dE + (\Phi_E(\Delta))_w \cdot \left(\frac{S(\Delta)}{\rho}\right)_w \cdot \Delta}{\int_{\Delta}^{E_{max}} \Phi_{E,w} \left(\frac{L}{\rho}\right)_{\Delta,a} dE + (\Phi_E(\Delta))_w \cdot \left(\frac{S(\Delta)}{\rho}\right)_a \cdot \Delta} \quad (1.10)$$

The lowest energy of electrons considered in the spectrum is defined by Δ , electrons below are included in the restricted stopping powers L (see section 1.3.1), electrons falling below are considered by the track-end term in nominator and denominator, with initial kinetic energy between Δ and 2Δ ⁷.

The choice of Δ is more or less arbitrary. It must ensure that kinetic energy of electrons below Δ leaving the cavity, is compensated by electrons with energy larger Δ , but stopping inside the cavity, i.e. creating the δ -electron equilibrium. Usually Δ is set to 10 keV, the average energy needed by an electron to just cross a cavity of a typical ionization chamber. More precisely Δ depends on the exact shape and dimension of the cavity. Hence, the recently published German dosimetry protocol DIN 6800-2 includes a correction factor to take the deviation from the 10 keV value into account. The need for a correct choice was previously discussed by Sempau et al. (2004) and by Borg et al. (2000), but the introduction of the proposed factor is new and no quantitative data exist yet.

Stopping-power ratios between water and air for primary photons and electrons are included in the current international dosimetry protocol as calculated data based on Monte Carlo simulations. The values for photons are based on the calculations of Andreo (1993), the ones for electrons based on realistic, i.e. Monte Carlo calculated electron beams by Ding et al. (1995).

A comprehensible correction arises from the fact that the theory of Spencer-Attix assumes an idealized cavity within the surrounding medium. In reality a *perturbation* always occurs, caused by the finite volume of the detector and its construction with materials differing from water in atomic composition and density. In figure 1.6 the influence of the chamber wall on electron fluence is shown, which illustrates the complex problem of chamber dependent electron fluence perturbations.

The dose measured in the detector D_c can be corrected for the perturbation of the electron fluence by a factor p and allows the determination of dose to water D_w at the depth z

$$D_w(z) = D_c \cdot p \cdot s_{w,a}^\Delta \quad (1.11)$$

The introduction of a depth z for D_w is necessary since the position of the finite detector does not necessarily correspond to the point where dose is determined⁸.

In the case of a thimble ionization chamber the factor p can further be divided up into individual independent factors that each describe an effect on electron fluences. The following definitions follow the nomenclature of the IAEA and German DIN 6800-2

⁷The upper limit is caused by the fact that the electron cannot lose more than half of its kinetic energy in an inelastic collision.

⁸In fact p and $s_{w,a}^\Delta$ are depth-dependent as well, but this dependency will be introduced later.

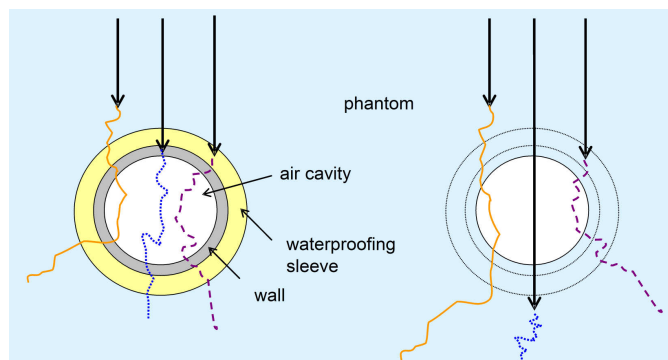


Figure 1.6.: Schematic illustration of perturbation effects for secondary electrons in the air cavity due to the presence of the chamber wall. The straight arrows represent primary photons which create secondary electrons (curved lines), passing the air cavity and depositing dose. The wall materials differing from water, lead to a change in the electron fluence (left) compared to the ideal case where no wall is present (i.e. all material is water) (right).

respectively.

- The central electrode perturbation correction p_{cel} accounts for the central electrode in a thimble ionization chamber. All current protocols use the Monte Carlo derived values of Ma and Nahum (1993b) which show good agreement with measurements of Palm and Mattsson (1999).
- The p_{wall} correction is applied, since the chamber wall material differs from the surrounding water. This factor might also include p_{sleeve} , which corrects in the same sense for a waterproofing sleeve. An approximate and simple analytic formulation exists (see below).
- The p_{stem} perturbation correction factor takes the existence of a chamber stem into account, but is usually ignored or included in some way in the wall correction.
- The displacement correction p_{dis} accounts for the fact that the air cavity of a cylindrical chamber causes less attenuation or build-up than the water displaced by it and causes the upstream shift of the effective point of measurement. The numerical values are usually based on measurements of Johansson et al. (1977).
- The p_{cav} factor corrects for scattering differences between the air cavity and the surrounding material, usually water. In high-energy photon beams the p_{cav} is generally assumed to equal unity at points where (transient) electronic equilibrium is achieved (see fig. 1.3).
- The p_{Δ} as a new factor in the current German dosimetry protocol DIN6800-2 accounts for the ionization chamber specific cutoff energy Δ in the calculation of the Spencer-Attix stopping-power ratios.

The product of the two factors p_{cav} and p_{dis} is referred to as the replacement correction P_{repl} ⁹ in the AAPM TG-51 protocol (Almond et al., 1999). Since the two factors are

⁹Note that in the TG-51 nomenclature capital letters are used for the individual perturbation factors.

strongly related to the same effects of the cavity inside the phantom, it is rather difficult to separate the individual factors. Therefore, the concept of one individual factor p_{repl} will be adopted in the following. Instead of applying a multiplicative correction factor the influence can be corrected, displacing the chamber by an amount that compensates for this effect, often referred to as the use of the effective point of measurement (EPOM). This approach is stipulated in the German dosimetry protocol, the data for the shift are based on measurements of Johansson et al. (1977). They estimated the needed shift from comparative measurements with a plane-parallel ionization chamber where no displacement is assumed (Andreo et al., 2001). A uniform shift of 0.5 times the inner radius r_{cav} towards the focus is used for cylindrical ionization chambers. Recent discussions about the validity of this value, Monte Carlo simulations, and measurements support the inadequateness of this approach. There is recent discussion on the validity of this value. Monte Carlo simulations and measurements support the inadequateness of this approach (Kawrakow, 2006b; McEwen et al., 2008). In the AAPM TG-51 a shift of 0.6 times the inner radius is required for relative photon dose measurements.

For the wall perturbation correction factor p_{wall} , Almond and Svensson (1977) developed a theoretical formulation which was later modified by Gillin et al. (1985) and Hanson and Tinoco (1985). According to their theory the wall perturbation can be calculated with ratios of mass-energy absorption coefficients and restricted stopping powers between the different materials:

$$p_{\text{wall}} = \frac{\alpha \left(\frac{\bar{L}}{\rho}\right)_{\text{air}}^{\text{wall}} \left(\frac{\bar{\mu}_{\text{en}}}{\rho}\right)_{\text{wall}}^w + \tau \left(\frac{\bar{L}}{\rho}\right)_{\text{air}}^{\text{sleeve}} \left(\frac{\bar{\mu}_{\text{en}}}{\rho}\right)_{\text{sleeve}}^w + (1 - \alpha - \tau) \left(\frac{\bar{L}}{\rho}\right)_{\text{air}}^w}{\left(\frac{\bar{L}}{\rho}\right)_{\text{air}}^w} \quad (1.12)$$

In the above equation α is the fraction of dose in the cavity due to electrons originating in the chamber wall, τ the corresponding fraction from a waterproofing sleeve (or second wall material). If no sleeve (or no second wall material) is present, i.e. $\tau = 0$ the above equation simplifies to the original formulation of Almond and Svensson (1977).

$$p_{\text{wall}} = \frac{\alpha \left(\frac{\bar{L}}{\rho}\right)_{\text{air}}^{\text{wall}} \left(\frac{\bar{\mu}_{\text{en}}}{\rho}\right)_{\text{wall}}^w + (1 - \alpha) \left(\frac{\bar{L}}{\rho}\right)_{\text{air}}^w}{\left(\frac{\bar{L}}{\rho}\right)_{\text{air}}^w} \quad (1.13)$$

It is more or less a simple approach to solve the complex problem of wall perturbation, which is a combination of different scattering and attenuation properties of the chamber wall compared to the surrounding water. One major drawback is that CPE is assumed for electrons generated in the wall and sleeve material that is usually not established for common wall thicknesses. Further, the electron spectra generated in the water are changed when electrons pass the wall and sleeve material, which is generally not accounted for in the calculation of stopping-power ratios. However, this theory is still included even in the latest dosimetry protocols as the DIN 6800-2 from 2008.

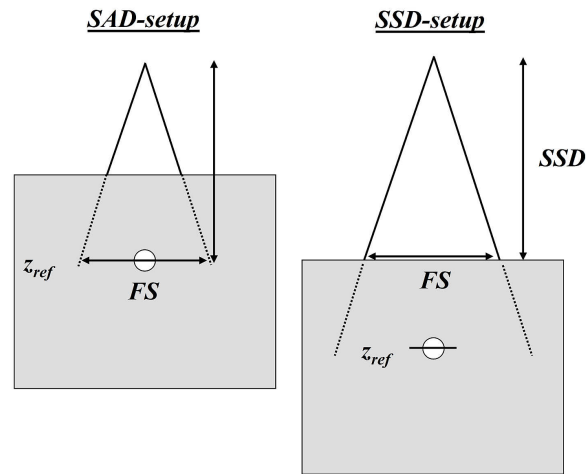


Figure 1.7.: Schematic illustration of geometrical reference conditions for a SAD-type (source-axis distance) setup applied in calibration and SSD-type (source-surface distance) setup usually used for photon dose measurement. The ionization chamber is located at the central axis of the beam in the depth z_{ref} and irradiated by a beam of field size FS . Numerical values can be found in table 1.1.

1.4.4. Dosimetry Protocols

Current dosimetry protocols define the procedures for the determination of absorbed dose to water in clinical dosimetry with calibrated ionization chambers for external radiation therapy. The ionization chambers are placed in a water-filled phantom and are irradiated by the user's beam. Instead of applying the cavity theory directly, calibrated ionization chambers are employed, since due to manufacturing variability the exact volume of the air cavity is usually not known exactly. Further, the chamber construction itself perturbs the radiation field as discussed in the previous section. Thus, a calibration coefficient is introduced:

$$D_{w,Q_0} = M_{Q_0} \cdot N_{D,w,Q_0} \quad (1.14)$$

The calibration coefficient N_{D,w,Q_0} must be traceable to a primary standard laboratory and relates the reading of the dosimeter M_{Q_0} , formed by ionization chamber and electrometer, to dose to water D_w in a reference field under reference conditions. These reference conditions are regarding air pressure, temperature, field sizes, measurement depth, phantom size and quality Q of the incident beam. The geometrical reference conditions for photon beams are illustrated in figure 1.7 schematically and summarized in table 1.1.

Usually only a few of the defined reference conditions can be maintained in the user's beam. The deviations due to *influence quantities* (Andreo et al., 2001) are corrected for by the application of a product of multiplicative factors of two classes. The first class corrects for changes in beam quality compared to the reference beam quality Q_0 , usually

Table 1.1.: Geometrical reference conditions for calibration and measurement in photon beams according to TRS-398 and DIN 6800-2, respectively.

Influence quantity	reference value	
	<i>calibration</i>	<i>measurement</i>
measurement depth (z_{ref})	5 cm	10 cm
source-chamber distance (SCD)	100 cm	110 cm
phantom size	30 x 30 x 30 cm ³	side length FS + min. 5 cm
field size (FS)	10 cm x 10 cm (at z_{ref})	10 cm x 10 cm (at SSD)

⁶⁰Co¹⁰. The rationale for the beam quality correction was given in the previous section, where the concept of sprs and perturbation correction factors was introduced. Extending these corrections to a function of beam quality leads to:

$$k_Q = \frac{N_{D,w,Q}}{N_{D,w,Co60}} = \frac{\left(s_{w,a}^{\Delta} \cdot p_{cel} \cdot p_{wall} \cdot p_{repl} \cdot p_{stem} \cdot p_{\Delta}\right)_Q}{\left(s_{w,a}^{\Delta} \cdot p_{cel} \cdot p_{wall} \cdot p_{repl} \cdot p_{stem} \cdot p_{\Delta}\right)_{Co60}} \quad (1.15)$$

The sprs vary with energy mainly due to the difference in the density effect correction of water and air (see eq. 1.10).

The second class of corrections is given by deviations other than energy or beam quality dependency, which can be summarized to charge measurement corrections. These include recombination correction for ions that recombine before they reach the electrodes, temperature-pressure correction for the varying density of air and humidity of the air, polarity correction for the effect of altering the measured charge with polarity. This second class of charged corrections is of minor interest in this thesis, because it is not directly open to Monte Carlo based investigations. Still, these factors and their possible non-constant nature should be kept in mind.

The dose to water in a user's beam, measured with an ionization chamber dosimeter, is given by

$$D_{w,Q} = M_c \cdot N_{D,w,Co60} \cdot k_Q \quad (1.16)$$

where M_c is the corrected charge reading of the dosimeter, $N_{D,w,Co60}$ the ⁶⁰Co calibration factor, and k_Q the beam quality correction factor. The latter one is separated within the scope of the German DIN protocol into chamber independent factor k'_Q , taking variations of stopping powers and the chamber dependent factor k''_Q for variations of the other perturbation correction factors (see eq. 1.15) with beam energy into account.

Dosimetry protocols provide the user with data of k_Q for various ionization chambers and beam qualities, requiring to maintain the geometrical reference conditions. The numerical values of individual perturbation correction factors needed for the evaluation of equation 1.15 are based on various approximations, comparative measurements with presumably perturbation free detectors, and theoretical considerations (e.g. Almond-

¹⁰The ⁶⁰Co beam is chosen due to the long half-life time and the simple spectrum leading to a precisely known quality and dose rate.

Svensson theory). The direct measurement is usually not possible, since an ideal cavity does not exist and further the individual perturbation correction factors usually occur together.

Following the international dosimetry protocol of the IAEA, as well as the German DIN 6800-2, the beam quality Q is defined as the ratio of dose readings in 10 cm and 20 cm depth within a water phantom. Differently, the TG-51 protocol defines beam quality as the percentage value of relative dose in depth $z=10$ cm normalized to the depth-dose maximum $\%dd(10)_x$ under absence of contaminant electrons (Almond et al., 1999).

1.4.5. Non-Reference Conditions

Non-reference conditions occur whenever the conditions defined in dosimetry protocols cannot be maintained. *Geometrical* non-reference conditions arise whenever the field size or measurement position inside the phantom changes (see tab. 1.1). This is the case for output-factor¹¹ measurements and measurement of relative distributions, as profiles or depth-dose curves, needed for quality assurance or commissioning procedures (see fig. 1.4). When measuring with ionization chambers the changed response is usually not taken into account. Thus, relative distributions in photon beams are not corrected for any change in perturbation correction factors, since a constant value is assumed.

Primary electron beams show strong variation in spectral distribution as a function of depth, so that a depth dependent correction for stopping-power ratios must be applied. The procedure is given in the current dosimetry protocols. Recent Monte Carlo driven studies revealed the change of wall perturbation that was usually assumed to be constant (Buckley and Rogers, 2006a,b; Sempau et al., 2004; Zink and Wulff, 2008). Still, an equivalent study on correction factors for photon beams is not known up to date. The conceptual foundation but without any numerical value has been included in the current DIN 6800-2 dosimetry protocol.

The factor k_{NR} corrects for any change of k_Q (see eq. 1.15) whenever the field size FS , off-axis distance R , depth z , or source-surface distance SSD is altered from geometrical reference (*ref*) conditions

$$k_{NR} = \frac{k_Q(z, FS, R, SSD)}{k_Q(10 \text{ cm}, 10 \text{ cm} \times 10 \text{ cm}, 0 \text{ cm}, 100 \text{ cm})} \quad (1.17)$$

which might be rewritten as

$$k_{NR} = \frac{(p \cdot s_{w,a}^{\Delta})_{non-ref}}{(p \cdot s_{w,a}^{\Delta})_{ref}} = \frac{(D_w/D_c)_{non-ref}}{(D_w/D_c)_{ref}} = \frac{f_{non-ref}}{f_{ref}} \quad (1.18)$$

with the correction factor p as the product of the individual perturbation correction factors p_{cel} , p_{wall} , etc. due to the presence of the ionization chamber in the beam. In the above equation dose to water is referred to as D_w and dose to the sensitive volume of the ionization chamber is D_c .

¹¹The outputfactor OF is defined as the ratio of dose in the phantom for a field size A to dose for a 10 cm x 10 cm.

Usually it is assumed that the chamber-dependent perturbation correction factor p does not change, thus the above equation would simplify and take only changes in Spencer-Attix restricted sprs $s_{w,a}$ between water and air into account. These have been demonstrated to change by less than 0.3% in photon beams (Sánchez-Doblado et al., 2003) and ionization chambers are generally used without k_{NR} -corrections in photon dosimetry. For procedures involving relative beam dosimetry generally no change of response is taken into account.

For relative dosimetry other types of detectors might be used. Still, as recommended by TG-106 (Das et al., 2008b) ... *one should compare it with ionization chamber measurements to confirm its correct operation and accuracy in data.* Sauer and Wilbert (2007) used the comparison of diodes with ionization chambers to correct their energy dependence. This requires the factor k_{NR} actually to be equal one which is difficult to verify. According to TG-106, the general goal in relative dosimetry for beam data acquisition is measurement errors below $\pm 1\%$. This can only be fulfilled if k_{NR} actually is below 1%, which is assumed to be true for ionization chambers used without any corrections.

With the introduction of advanced radiation treatment techniques such as stereotactic radiosurgery or intensity modulated radiotherapy small fields sizes result. Special treatment machines as the Gamma-knife, Cyber-knife or Tomotherapy accelerators (Mackie, 2006) do not even allow to use field sizes required by the dosimetry protocols. Concepts for standardized recommendations were currently published by an international working group (Alfonso et al., 2008). Accordingly, the beam quality correction factor k_Q of a reference field is connected to the situation in clinical fields with the use of special “field factors”.

Small fields and Charged Particle Disequilibrium

Small fields, defined as fields with sizes smaller than the lateral range of charged particles (Alfonso et al., 2008), might exhibit some degree of charged particle disequilibrium (CPD). Due to CPD a condition exists, where the application of the Spencer-Attix cavity theory as described above must be considered with restrictions. The perturbations are not known and vary as a function of space within these fields, especially at field boundaries or within the penumbra. The change of electron spectra within in the range of a field boundary is usually rigorous compared to the size of any realistic ionization chamber. This fact makes the determination of dose with ionization chambers and common approaches in regions of CPD difficult and leads to large uncertainties $\geq 5\%$ (Capote et al., 2004; Ding et al., 2008). The averaging effect due the finite detector volume leads to loss of spatial resolution in relative dose measurements. In principle this averaging can be expressed by the replacement perturbation correction factor p_{repl} , accounting for the fluence change due to the insertion of the finite volume compared to the desired dose to water at a point. Usually, ignoring the change of response of the detector, it is understood as a convolution of the underlying dose distribution (Das et al., 2008a).

Das et al. (2008a) have defined three categories of problems for small field dosimetry:

- Effects of radiation source size: Due to the collimation of a source with finite size, only a part of the source can be viewed from the detector’s field of view.

The setting of beam collimators, where the primary photon beam is scattered and thus blurred further, complicates the exact definition of a field size with traditional metrics for determination such as full width at half maximum.

- Electron ranges and loss of CPE: Electrons have a certain lateral range at the field boundary, which is further prolonged in the low density air of an ionization chamber with a finite volume.
- Measurement: The CPD might cause a breakdown of the (Spencer-Attix) cavity theory and the corrections for reference dosimetry cannot be applied.

Seuntjens and Verhaegen (2003) argued that the factorization scheme (see eq. 1.15) usually used in dosimetry protocols has limited meaning to small fields. Accordingly, they considered Spencer-Attix restricted sprs to inadequately approximate the dose conversion factors in small field dosimetry because they are based on unperturbed spectra. In fact, the chamber dependent factors might be much larger than the variation in sprs and these perturbations need to be known. However, if one would be able to calculate the sprs within the CPD *at one point*, and the factorization in individual perturbation correction factors is valid under these strong CPD, the application of the Spencer-Attix theory might still be correct.

There are some approaches to overcome the problems associated with CPD by the use of Monte Carlo simulations. Capote et al. (2004) calculated so called *c-factors* for ionization chambers in small IMRT fields. These relate the value f in equation 1.8 for the non-reference conditions to one under reference conditions, as a ratio between calculated dose to water and dose to the sensitive volume of the chamber, which is the same approach as given in equation 1.18. The approach has been used several times (Gonzales-Castano et al., 2007; Sánchez-Doblado et al., 2007) and is one of the approaches suggested in the mentioned recommendations of Alfonso et al. (2008). A different solution was proposed by Bouchard and Seuntjens (2004) and later by Tantot and Seuntjens (2008). They pre-calculated the response of ionization chambers to zero field-width pencil beams leading to kernels, which later could be summed up for individual field shapes.

1.4.6. Other Types of Detectors

For the determination of absolute dose ionization chambers are recommended in every dosimetry protocol. Depending on the measurement task, i.e. relative measurements, other types of detectors may be used.

Semiconductors have small sensitive volumes yielding high spatial resolution and show quick response time and high sensitivity. Still, they show an increased response to low energy photons, temperature and dose-rate dependencies. The response to low energy photons makes them mostly unsuitable for use in larger photon fields where a comparatively large amount of multiple scattered and thus low energy photons exist. Therefore, shielded or energy compensated designs exist, where the sensitive volume is shielded from low energy scattered photons. Diamond detectors as solid-state detectors with small sensitive volume are nearly tissue equivalent. Ionizing radiation causes a temporal change in electrical conductivity which can be measured. Diamond detectors are difficult to manufacture and thus comparatively expensive. Thermoluminescent (TLD)

detectors as indirect dosimeters are available in different sizes and shapes and are often used for *in-vivo* dosimetry because they do not require a connection to any electrical source. TLDs exhibit a dose and energy dependence. The accuracy of TLD dosimetry strongly depends on the cross calibration technique to an ionization chamber and their handling. For relative dose measurement films are often applied due to their high spatial resolution. Currently, ionization chambers filled with dielectric liquids (Wickman, 1974) are becoming commercially available. The liquid replacing the air as sensitive material offers a high signal with a comparable small volume.

1.5. Monte Carlo Simulations of Radiation Transport

1.5.1. General Introduction and Historical Background

The Monte Carlo method can generally be described as a statistical method for numerical integration with the use of random numbers. First descriptions of this method reach back to the year 1777 (de Buffon, 1777) and the first popular examples were computer based calculations for radiation transport at the end of World War II (Kalos and Whitlock, 2004; Eckhardt, 1987). The use of digital computers made the application of this method a valuable tool in science and technology.

Generally spoken, the Monte Carlo simulation of radiation transport uses the knowledge of individual, *microscopic* particle interactions in matter with the corresponding probability distributions. It applies random numbers to describe the random trajectories of these particles by sampling from the underlying probability distributions. Various sampling techniques applying uniformly distributed random numbers $[0, 1]$ exist (Kalos and Whitlock, 2004; Salvat et al., 2006). The probability distributions are based on the differential cross sections for the interaction mechanisms. Each primary particle may result in many particles of higher orders (e.g. electrons creating delta-electrons) forming a so called “history” or “shower”. Using a large set of N individual particles, the average *macroscopic* distribution of quantities such as dose can be calculated. Following the central limit theorem, the result of a Monte Carlo integration follows a Gaussian distribution and the estimated mean is within limits σ , that decrease with increased sampling size N , irrespective of shape of underlying probability distribution (Bielajew, 2001). The uncertainty of the mean σ (or its estimate s) follows

$$\sigma \propto 1/\sqrt{N} \quad (1.19)$$

and makes an appropriate finite sample size N necessary for a result within a certain confidence limit.

Besides enabling the description of particle transport, the Monte Carlo method allows to calculate quantities which are usually not accessible within a measurement. For example, particles can be marked in a certain region or after a certain interaction and their contribution to dose at a different point can be determined.

The application of the Monte Carlo techniques to problems in Medical Physics is

far-reaching. Probably the most popular example is the patient specific calculation of dose distributions, which has been proven to be the most accurate algorithm in treatment planning, being able to cope with situations of density heterogeneities where other algorithms based on analytical, simplified solutions tend to fail (Fogliata et al., 2007). As a consequence modern treatment planning systems employ the Monte Carlo method, implemented in optimized codes for faster calculation. Already, the widely used algorithms using superposition/convolution algorithms are based on Monte Carlo precalculated energy-deposition kernels, which describe the distribution of dose around a primary photon interaction site. Strongly connected to the patient dose calculations are simulations of clinical linear accelerators (Seuntjens and Verhaegen, 2003; Ma and Jiang, 1999). Besides the application in the dominant field of treatment planning, the Monte Carlo method can be found in calculations for diagnostic X-ray examinations, either for image processing and corrections, or for evaluation of patient dose.

Various so called general purpose Monte Carlo codes exist, which incorporate all necessary routines and algorithms needed for simulations in the field of Medical Physics. The most popular and wide spread code in the Medical Physics domain is the EGS series of codes. In the following section a brief introduction to this code used throughout the thesis will be given.

1.5.2. The EGSnrc Code System

The first versions of the EGS (Electron-Gamma-Shower) system were developed in the 1970s at the Stanford Linear Accelerator Center (Rogers, 2006). During the 1980s the EGS4 system was released, which was subsequently used in Medical Physics applications, e.g. it was used as basis for the BEAM system (Rogers et al., 1995). The EGSnrc Monte Carlo code system is the most recent version developed at the National Research Council of Canada (NRC) and incorporates many improvements considering the implemented transport physics (Kawrakow, 2000*b,a*).

The EGSnrc system provides subroutines and functions for sampling from various photon and electron interactions and for simulating of electron and photon transport. The quantities of interest (e.g. absorbed dose) are available to the user during runtime and must be processed (“scoring”) for calculating and reporting of the final result. For a complete application the user can combine the transport subroutines and must implement source, scoring and geometry related functions.

A set of readily implemented “user codes” is available (Rogers et al., 2005), which allows the definition of a geometry, set-up of various particle sources (e.g. parallel beam of photons with certain spectral distribution), and the scoring of quantities sufficient for most problems. For example, the SPRRZnrc code allows the calculation of sprs, the FLURZnrc calculates fluences and particle spectra and the DOSRZnrc code scores dose in an arbitrary geometry constituting of cylinders (RZ-geometry). The BEAM code can be employed to calculate the passage of particles through the head of a linear accelerator (see chapter 1.5.6). It incorporates its own geometry functions, organized in a set of modules as jaws or a flattening filter. The DOSXYZnrc code calculates dose to rectilinear voxels of a homogeneous or heterogeneous geometries (Rogers et al., 2006).

Prior to all simulations the cross section databases for photon and electron interactions

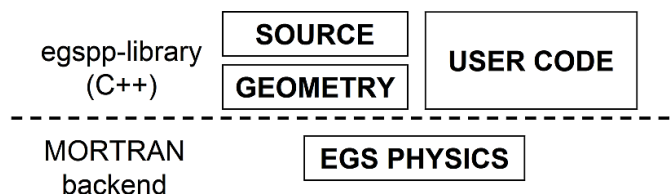


Figure 1.8.: Principle of the EGSnrc system. The original physics back-end written in MORTRAN is separated from the C++ classes for geometry and particle source related functions. Gathering of information, i.e. scoring and the manipulation during particle transport is implemented in a so called C++ “user code”.

are initialized. The data sets are provided in look-up tables for the materials found in the simulation geometries. These tables can be generated with the PEGS-program, the cross section data preprocessor for EGS.

The EGSnrc code is written in the MORTRAN programming language, which is a string preprocessor for the FORTRAN language (Kawrakow and Rogers, 2006). Since 2005 the C++ programming language class library “egspp” is included in the EGSnrc system (Kawrakow, 2006a). It provides the user with a powerful geometry and source module, allowing for the definition of complex geometries and particle sources. Furthermore, the user can write his own applications in C++ derived from available application classes. This application framework easily allows for custom-made, special purpose implementation of scoring and variance reduction techniques and is still connected to the MORTRAN back-end, taking care of all involved physics mechanisms.

All relevant photon and electron interactions are implemented in the EGSnrc code, as described in chapter 1.3. It should be specifically noted that the implemented electron transport algorithm circumvents the shortcomings of earlier Monte Carlo algorithms, especially for the case of ionization chamber calculations (Kawrakow, 2000b).

Random numbers which are needed in every Monte Carlo algorithm are generated with appropriate random number generators (RNG), providing sequences of highly uncorrelated and uniformly distributed numbers. The EGSnrc system usually applies the RANMAR type of RNG (Marsaglia et al., 1990).

1.5.3. Simulation of Photon and Electron Transport

The particles track in a coupled electron-photon field can be interpreted as a “Markov-process”, where “future values of a random variable (interaction event) are statistically determined by present events and depend only on the event immediately preceding”. Thus, the macroscopic solution of complete Boltzmann transport equation is broken down to single microscopic events even for complex geometries (Bielajew, 2001).

The simulation of transport generally consists of four steps: (1) selection of distance to next interaction, (2) transport to interaction site, taking geometry into account, (3) selection of interaction type, (4) simulation of interaction. These steps are repeated until particles have left the defined simulation geometry or if their energy falls below a speci-

fied energy, which is the energy where particles are assumed to be stopped and absorbed in the medium. In the EGSnrc code system these energies are referred to as E_{CUT} for electrons/positrons and P_{CUT} for photons.

For the energy range in external radiotherapy treatment, photons interact in the processes discussed in section 1.3.2 and their transport can be simulated in an “event-by-event” fashion. An electron and its descendants in the energy range of a few MeV undergoes 10^6 elastic and inelastic collisions until it comes to rest and is locally absorbed. It is not possible to calculate every single interaction in a reasonable calculation time and most of the collisions result in only minor changes of energy and direction. Berger (1963) introduced the condensed history technique (CHT), which concentrates a number of single interactions into single straight steps accumulating the minor deflections caused by elastic collisions and large number of small energy losses. The sampling of an artificial event at the end of such CH step requires an appropriate multiple scattering theory, taking the angular deflections and some path length corrections into account. In the so called class II models employing the CHT a certain threshold distinguishes between “catastrophic” events above which created knock-on electrons and Bremsstrahlung photons are explicitly modeled. Below these energy thresholds, effects due to the production of the secondary particles are grouped, i.e. the stopping powers in the calculation are restricted to energy losses smaller than this threshold (see chapter 1.3.1). In the EGSnrc system the threshold for generation of δ -electrons is called AE and AP for Bremsstrahlungs-photons.

1.5.4. Variance-Reduction Techniques - General Concepts

The main drawback of the Monte Carlo methods as a stochastic technique can be attributed to its random nature. Thus, an inherent statistical uncertainty in results must be addressed to results. Increasing the number of statistical independent samples or histories decreases the uncertainty but increases the computational effort. A general metric for the efficiency ϵ of a Monte Carlo simulation can be defined as

$$\epsilon = \frac{1}{\sigma^2 T} \quad (1.20)$$

where σ^2 is the variance of the simulation result (or rather its estimate s^2) and T the CPU simulation time needed for this variance. The time T is directly proportional to the number of simulated particles N . Ideas exist to increase the efficiency, often referred to as variance reduction techniques (VRT), although not necessarily reducing only the variance in the above equation. Rather, the time needed to achieve a specific uncertainty is shortened in these techniques. A more appropriate term might be “efficiency enhancement techniques”. Various advanced techniques are known, mostly specific to the problem investigated (Bielajew, 2001). In principle the mentioned condensed history technique in section 1.5.3 can be considered as a the most important VRT. Further two general classes can be defined that increase the efficiency.

The first class increases the efficiency by making approximation to the transport simulation. Certain energy thresholds can be defined, so that a particle is discarded and its energy is deposited locally, whenever it falls below the threshold. It is clear that increasing the threshold reduces the simulation time, but introduces a bias. A more advanced

method, which still approximates the charged particle transport physics, is the range rejection (rr). Although the CHT decreases the time for electron transport, usually most of the time in a Monte Carlo simulation is required for charged particle transport. The idea is to discard a charged particle whenever its kinetic energy is too low to leave a certain region. The corresponding implementation in a Monte Carlo code is generally straightforward, since energy (and thus range) and the closest distance to the most proximate boundary is usually known during particle transport. This technique is an approximation since it ignores the possible production of Bremsstrahlung or annihilation radiation. Hence, a threshold needs to be defined below which rr is applied to charge particles. The use of precalculated data for fast patient simulations is another example for a VRT that (most negligibly) approximates the transport physics for charged particle transport (Neuenschwander et al., 1995).

The second class of VRTs is considered as a “true” VRT, because it does not introduce any bias. Two commonly used and opposing ideas usually used in conjunction are “splitting” and “Russian Roulette”. Generally speaking, splitting leads to N particles with a statistical weight reduced to $1/N$. Thus, a splitted particle contributes to only $1/N$ in a scored quantity such as dose, but the probability for the dose deposition is increased due to the larger number of splitted particles. The splitting can be applied in many ways. One example is to split rare Bremsstrahlung events as in the case of linear accelerator simulations (Kawrakow et al., 2004). Another example is splitting a photon in a geometry into N split photons and distributing the interaction sites uniformly along the initial photons path (Kawrakow and Fippel, 2000).

The “game” of Russian Roulette (RR) can reversely reduce the number of particles simulated and thus the time needed to simulate their transport. If a particle survives the game, it carries a statistical weight, increased by the inverse probability to survive the game. Metaphorically speaking, it carries the physics for all others that did not survive. The surviving particle, often referred as “fat” particles contribute to scored quantities with their increased weight. Comparable to splitting, photons can be forced to interact and reduce the weight of secondaries accordingly without introduction of a bias (Rogers et al., 2005; Salvat et al., 2006).

The incorporation of these mentioned and the development of further specific methods for patient simulation were crucial steps for the implementation of Monte Carlo algorithms in context of therapy planning systems. For the investigation of ionization chambers and calculation of correction factors in the order of only a few percent or less, the use of variance reduction methods is indispensable, but must not introduce any bias and *true* VRTs are needed. Also, the simulation of radiation propagation through the treatment head of a linear accelerator is nearly impossible without the use of advanced VRTs. The corresponding algorithms and concepts used in this thesis will be explained in more detail in chapter 2.

Even with elaborate variance reduction techniques, the calculation times for ionization chamber investigations are usually too long on a single personal computer CPU. The Monte Carlo method itself, yielding a result from many individual and independent calculations, is predestined for parallel computing on a computer cluster. In practice the total number of histories can be split and calculated independently with a different sequence of random number on different CPUs (or nodes) of the cluster. When the simu-

lation is finished, the single results are combined as a mean of all independent runs. The heavy use of computer hardware might be understood as a “brute force” VRT, since a reduction in overall computation time is achieved. In principle, doubling the number of CPUs cuts the simulation time in half. Still, the network speed and initialization of each single simulation slightly increases the overall time.

1.5.5. Ionization Chamber Calculations

The simulation of ionization chambers offers the possibility to calculate quantities as perturbation correction factors. It turned out that the situation of a low density, air-filled cavity surrounded by some high density material is challenging for any Monte Carlo code (Rogers, 2006). This challenge is caused by the fact, that the condensed history approach (see chapter 1.5.3) fails close to media interfaces, if no special treatment is introduced. One single straight condensed history step might neglect some parts of a “real” track, taking place in the second medium beyond the interface. This problem is severe for two media which largely differ in properties, such as air and water. In the early applications special algorithm settings were needed, complicated to evaluate (Nahum, 1988; Rogers, 1993). Not before the development of new electron transport algorithms, which allow for a single scattering close to media interfaces, accurate ionization chamber was possible (Kawrakow, 2000b).

1.5.5.1. Calculations with EGSnrc

Various studies confirmed the accuracy of the EGSnrc code for ionization chamber investigations by directly comparing to measurements. These investigations focused on the overall uncertainties, including the accuracy of the algorithm and uncertainties in cross sections (Kawrakow, 2000a,b; Borg et al., 2000; Seuntjens et al., 2002; McCaffrey et al., 2004; Selvam et al., 2005; Russa et al., 2007). Ubrich et al. (2008) used ionization chambers with varying central electrode diameters in kilovoltage X-ray beams for determination of the ideal diameter. The variation in response due to the different aluminum electrodes and energies of the X-ray source could generally be reproduced at a 0.5 % level. In a recent publication Russa and Rogers (2008) investigated the ability of the EGSnrc code to reproduce experimental data for the change in ionization chamber response associated with changes in wall material and cavity dimensions in ^{60}Co beams. They concluded that the EGSnrc system can reliably be used to calculate the measured response within an accuracy of a few percent or less.

1.5.5.2. Fano Cavity Test

The most severe test for the accuracy of Monte Carlo codes considering the ability to calculate ionization chamber response correctly is the so called Fano cavity test. Under Fano conditions the dose to the ionization chamber model can be calculated and compared to the expected result.

The dose to the cavity of medium *cav* of an ionization chamber irradiated by primary photons of energy E , normalized to the incident fluence Φ_0 , can be written as

(Kawrakow, 2000b; Rogers, 2006)

$$\frac{D_{cav}}{\Phi_0} = A_{wall} A_{fl} \left(\frac{\bar{L}}{\rho} \right)_{wall}^{cav} \left(\frac{\bar{\mu}_{en}}{\rho} \right)_{wall} E \quad (1.21)$$

where A_{wall} is a correction for attenuation and scatter within the wall of medium $wall$ and A_{fl} corrects for the fluence perturbation due to the cavity. In a Monte Carlo simulation some simplifications to the above equation can be made. The Fano theorem states that a constant fluence spectrum exists throughout a medium when CPE is achieved, independent of local density variations (Fano, 1954). If the cavity is made of the same material as the wall

$$A_{fl} = 1, \left(\frac{\bar{L}}{\rho} \right)_{wall}^{cav} = 1 \quad (1.22)$$

results. Further, scatter and attenuation of the primary photons can be removed by regenerating the properties (energy and direction) of a photon after an interaction, which leads to

$$A_{wall} = 1 \quad (1.23)$$

In the Monte Carlo simulation radiation due to Bremsstrahlung and atomic relaxation can be discarded, finally yielding

$$\frac{D_{cav}}{\Phi_0} = \left(\frac{\bar{\mu}_{en}}{\rho} \right)_{wall} E \quad (1.24)$$

The fluence Φ_0 does not need to be known, since the result of a Monte Carlo calculation is usually already normalized to the primary fluence of the source. When μ_{en} is calculated with the same cross section database, the test can be considered as independent of underlying uncertainties in these cross sections. An algorithm that fails to cope with an interface between two media with varying density or is not able to correctly handle boundary crossings difference will show deviations in this test. Usually, the deviation from the expected result is used for benchmarking of Monte Carlo codes considering their condensed history implementations.

Recently only the EGSnrc and the PENELOPE pass this test at a 0.1% level. The latter code requiring some careful parameter settings considering the electron steps (Yi et al., 2006; Sempau and Andreo, 2006). Other codes such as the GEANT4 simulation toolkit fail the test, as was discovered by Poon et al. (2005).

1.5.5.3. Cross-section uncertainties

With the known cross sections differential in energy, energy-loss, deflection angles etc. for certain interaction mechanisms, the complete particle track can be calculated as a simulation of physical reality. In a Monte Carlo simulation the properties of compounds are usually modeled with the single-atom or additivity approximation, i.e. single atoms in mixtures are assumed to be independent of each other and neglecting chemical bindings. This approximation is considered to be accurate in the mega-voltage energy range, where

the energy of incident photons is much higher than binding energies.

The cross sections for photon interactions, i.e. the mass attenuation coefficient, are based on compilations, e.g. Hubbell's XCOM (Hubbell, 2006). There is no exact statement on the accuracy of these compilations for single materials. Generally, for lower energies where the photoelectric effect is dominating, the uncertainties are higher especially close to absorption edges. For light elements and energies where the predominant effect is incoherent scattering, the theoretical modeling with free-electron Compton-scattering is assumed to be accurate. Following Hubbell (2006) the uncertainty is estimated to be in the order of $\pm 5\%$ for energies below 5 keV and $\pm 2\%$ for energies up to 10 MeV. For light elements though it is estimated to be below $\pm 1\%$, since the Compton scattering, dominant in this energy range, can closely be described using the free electron scattering approach.

The uncertainty in electron collisional stopping power following the Bethe-Bloch formulation (see eq. 1.1), are governed by the uncertainty in the mean ionization potential I . Following the ICRU37 report (ICRU, 1984), the uncertainty of I is in the order of 1-10 % for materials and mixtures found in ionization chambers. The uncertainties of the radiative stopping powers are estimated to be about 2-5 % for energies between 2 and 50 MeV and about 5 % below 2 MeV. According to AAPM's TG-105 the databases are felt to be sufficiently accurate for Monte Carlo treatment-planning purposes (Chetty et al., 2007). For ionization chamber related investigations however, there is a lack of information. There have been some attempts to quantify the uncertainty in these types of calculations by estimating the effects of cross section uncertainties and the effects of using different transport algorithms (Mainegra-Hing et al., 2003; Rogers and Kawrakow, 2003), but according to Rogers (2006) this is an area deserving further investigation and careful analysis.

1.5.6. Simulation of Linear Accelerators

In the above section the general requirements and methods for ionization chamber calculation were briefly discussed. The investigation of ionization chambers in the field of linear accelerators requires a realistic model of the radiation source. The particles emerging from a therapeutic external radiation source such as a linear accelerator (linac), can be characterized by a multidimensional distribution often referred to as a phase space function $f(E, x, u, \dots)$. The measurement of this phase space is nearly impossible and not trivial even for just one of the dimensions.

A linac for radiation treatment with photons has a general modular construction, independent of a certain vendor. A schematic illustration is given in figure 1.9. Electrons accelerated to some mega-electronvolt exit a vacuum window, closing the vacuum-filled flight tube with the electric field for acceleration and a construction of bending magnets. These electrons possess a certain energy, angular and spatial distribution. When hitting the target, Bremsstrahlungs photons are produced mainly in forward direction. This photon beam is collimated by a primary collimator and the fluence is attenuated by a flattening filter to produce a flat dose profile within a certain depth in water. A monitor chamber in the beam's path is used for online verification. A mirror is also present in the beam path, which projects a light field on the patients surface. Finally a collimat-

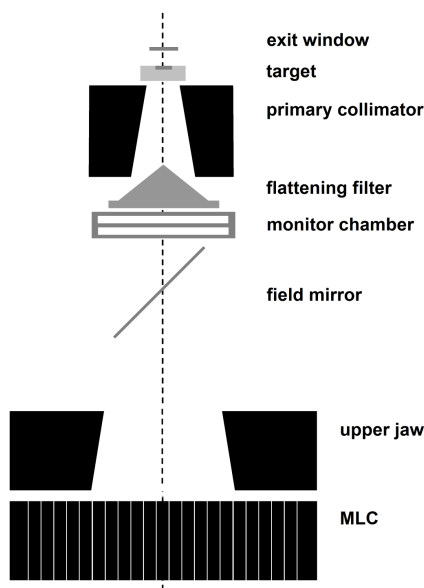


Figure 1.9.: Schematic illustration of a linear accelerator head. The multi-leaf collimator MLC is shown as a solid block, since its movement is perpendicular to the upper jaw.

ing system shapes the field in the x and y direction, consisting of massive blocks and/or multi-leaf collimators (MLC). MLCs exist in different shapes.

Monte Carlo simulations allow the generation of the phase space of such a model and have been used to calculate dose distributions from linear accelerators for decades (Verhaegen and Seuntjens, 2003). They were needed for the calculation of realistic sprs in dosimetry protocols. Especially for accurate radiotherapy treatment calculations *beam models* are needed, some of them directly based on the calculated phase space of linac Monte Carlo models (Seuntjens and Verhaegen, 2003). Further, Monte Carlo simulations have played an important role in the investigation and optimization of components of a linacs.

The calculation of photon transport through the head of a linac is time consuming due to the fact, that only a small fraction of the kinetic energy of incident electrons yields Bremsstrahlungs-photons. Special VRTs are implemented in modern Monte Carlo algorithms to enable the calculation of photon-related quantities such as dose or fluence at the bottom of a linac. For the BEAMnrc code (see chapter 1.5.2), the “Directional Bremsstrahlungs Splitting” (DBS) technique was introduced. In brief, whenever a radiative event (Bremsstrahlung, annihilation, characteristic x-ray emission) occurs, it is split NBR SPL times, with resultant photons carrying a weight $NBR SL^{-1}$. Careful selection of the splitting number ensures, that the increase of computing time for the transport of the splitted photons is much less than the gained increase of efficiency in dose or fluence at the bottom of the linac. Photons aiming to a user specified cone, defining the region of interest at the bottom of the linac, are kept, while all others are discarded via Russian Roulette (see chapter 1.5.4). If one of the surviving high-weight photons undergoes a Compton event subsequently, it is split as well. To reduce the number of transported

charged particles, RR is played with Compton-electrons of the aforementioned splitted Compton-interactions. Further, photons aiming inside the field of interest must survive a RR game, before they interact, effectively reducing the number of possible secondary charged particles. Although the actual implementation is far more complex (Kawrakow et al., 2004), the DBS algorithm ensures that many photons exist only in the user defined circular field of interest. The number of electrons can be increased afterwards by splitting them below the flattening filter rotationally symmetric, from where they have a certain probability to exit the linac. The DBS-algorithm allows to increase the efficiency of dose calculation in the order of a factor ~ 150 , compared to an analogue simulation without the technique and much higher efficiencies for photon fluence calculations. Independently of the DBS algorithm, usually a range rejection algorithm is applied (see chapter 1.5.4) to further reduce the transport of electrons without a chance to leave the accelerator at the bottom and being below an energy threshold.

Commissioning of a linear accelerator model

Although the nominal dimensions and materials of a certain linear accelerator are available from the manufacturer, the exact properties of the electron beam hitting the target is usually not known. Parameters such as kinetic energy and the size of the spot affect the dose distribution measured in a water phantom. Further, small changes in the exact position and material composition due to manufacturing variability of the accelerators components may have a certain impact. Usually the electrons' parameters of the linac model are varied until a match with measured data is obtained. Various approaches exist and due to the multidimensional characteristic of the problem the procedure of *commissioning* is complex.

Many papers can be found in literature dealing with the problem of Monte Carlo photon linac commissioning and source tuning, all with slightly different approaches. Verhaegen and Seuntjens (2003) proposed a procedure consisting of several steps based on their experience and publications available at this time: (1) In a first step percentage depth-dose curves of small fields are used to match the primary energy of the incident electron beam. As reported by Sheikh-Bagheri and Rogers (2002*b*), calculated percentage depth-dose (PDD) curves show only a weak dependence of the correct spot size. Recently these results were confirmed by Sham et al. (2008) for standard radiotherapy field-sizes down to 2 cm. For smaller field sizes in the order of a few millimeters the PDDs differed significantly. (2) Profiles measured in air or in shallow depths in a water phantom to avoid the influence of phantom scatter at larger depths can be employed to match the focal spot size. The spot is usually assumed to be a circle with a Gaussian width distribution. Sham et al. (2008) concluded from their measurements that the focal spot of their Varian Clinac can be modeled as a circle with a Gaussian distribution. According to Sheikh-Bagheri and Rogers (2002*b*) the beam horns of the relative cross profiles decrease quadratically with increased Gaussian width. A good match of energy must exist at this point, since the primary energy affects those to a large amount as well. (3) Another calculation of depth-dose curves must ensure, that the match still exists.

Pena et al. (2007) demonstrated the weak dependence of depth-dose curves on energy changes and therefore suggested to use wide-field profiles at shallow depth for the match of energy and spot size. Similarly, Tzedakis et al. (2004) started with PDDs for

initial energy determination, but later used profiles for adjustment of spot size and energy. Tonkopi et al. (2005) based their matching procedure solely on in-air profiles and were able to reproduce depth-dose curves. Likewise, Ding et al. (2006) tuned the parameters to match large fields even for small, stereotactic fields. Small fields have been demonstrated to be sensitive to the focal spot (Sham et al., 2008; Wang and Leszczynski, 2007). Their measurement requires appropriately chosen detectors with small volumes. Scott et al. (2008) on the other hand started with matching the penumbra for spot size, PDD curves for energy and later on large fields for the “fine tuning”. Pena et al. (2006) used this strong dependency of penumbra width on spot size for one of several weighted cost-functions in an automatic commissioning procedure. They used a large set of pre-calculated PDDs and cross profiles for various field-sizes to determine the best match. Still, one of their conclusion is that due to mis-matches in large fields the commissioning should use field sizes close to the one used for treatment planning. This renders their approach less useful.

Besides the parameters of the primary electron beam hitting the Bremsstrahlungstarget many other parameters must be considered to be free, although specified by the manufacturer. For electron beams Schreiber and Faddegon (2005) demonstrated the impact of exact positioning of the monitor chamber and scattering foils on calculated dose distribution for primary electron beams. For photon beams the density of the flattening filter is known to have a large influence on calculated profiles (Sheikh-Bagheri and Rogers, 2002a).

2. METHODS FOR MONTE CARLO BASED INVESTIGATION OF CLINICAL DOSIMETRY

In this chapter the methods for the investigation of clinical ionization chamber dosimetry are introduced. In the first section the developed variance reduction techniques and their investigation is described. In the second section the concepts for simulations of reference dosimetry are explained. Besides the determination of individual perturbation correction factors, the calculation of the overall beam quality correction factors for a widely used ionization chamber is described. Moreover, the method for quantification of systematic uncertainties, inherent to the calculated correction factors, is presented. In the last section the methods for investigation of dosimetry under non-reference conditions are introduced. These include the simulation of a linear accelerator model and its matching to corresponding measurements. Using the model, the calculation of corrections for ionization chambers under non-reference conditions is explained. The setup of a idealized photon field boundary for the study of charged particle dis-equilibrium and steep dose gradients is introduced. Besides testing a commonly used ionization chamber, the conditions of charged particle dis-equilibrium are used to compare various detectors considering their ability to measure a dose profile with low perturbations.

2.1. Increasing Efficiency

2.1.1. Ionization Chamber Calculations in Photon Beams

As discussed, clinical dosimetry follows the concept of dose to water as described in the current dosimetry protocols. Monte Carlo based dose calculations for photons are generally one order of magnitude less efficient than for electrons (Rogers and Bielajew, 1990). The Monte Carlo simulation of ionization chambers inside a water phantom is even more problematic. The typical measurement setup is an adverse one, considering calculation effort required. When comparing typical dimensions of ionization chambers (less than 0.6 cm^3) and of a water phantoms (up to 125000 cm^3) it becomes clear that the fraction, where particles actually can have a contribution to ionization chambers dose, is small. A simple Monte Carlo simulation of a $10 \text{ cm} \times 10 \text{ cm}$ photon field with primary photons of a 6 MeV spectrum reveals, that 99.9% of the photons do not have any contribution to the dose of a sphere with 1 cm diameter at 10 cm depth inside a waterphantom. Furthermore, 97% of simulation time is needed for electron transport only.

Figure 2.1(a) shows the mean free path (mfp) of monoenergetic photons in water as a function of energy. Considering the energy range of up to 25 MeV used in radiotherapy, the mfp can be larger than the water phantom's dimensions. Tracing photons through the phantom that do not interact is a waste of time, especially when time is needed to sample photons from an event generator, that creates particles as a result of a complete treatment head simulation. The CSDA range (see chapter 1.3.1) for an estimation of electrons ac-

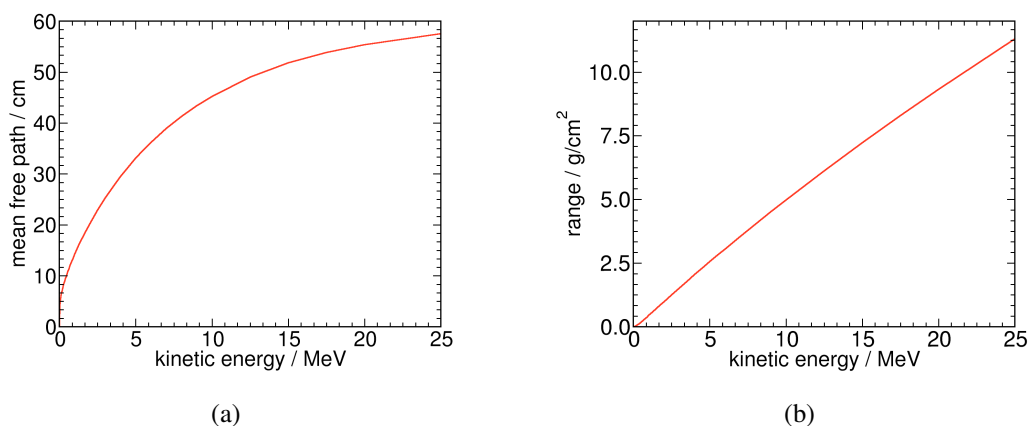


Figure 2.1.: (a): Mean free path in cm for monoenergetic photons in water. The data is taken from the XCOM database. (b): CSDA-range for monoenergetic electrons in water, calculated with the ESTAR program (Berger et al., 1998).

tual range as a function of energy is shown in figure 2.1(b). The range of low energy electrons is generally smaller than the distance between the point of electron production, e.g. at the field boundary, and the position of the ionization chamber. Simulating these electrons is unnecessary for the most part, since only created radiative photons (Bremsstrahlung, annihilation photons) can have a direct contribution to the ionization chambers dose.

The effects studied for ionization chamber dosimetry are usually in the order of a few tenth of a percent. Given the above observations, it is clear that simulations without any variance reduction techniques are nearly impossible, since they would require thousands of hours for a meaningful result.

2.1.1.1. *State of the art* ionization chamber calculation with the EGSnrc system

The `cavity` user code is part of the current EGSnrc distribution and permits the calculation of cavity dose for any small geometry typically describing an ionization chamber. The code is equipped with two powerful variance reduction techniques, namely photon splitting and an electron range-based Russian Roulette procedure. Photon splitting was introduced by Kawrakow and Fippel (2000) and found to increase the efficiency of external photon beam dose calculations for radiotherapy by a factor of up to 5. It is also suitable for ionization chamber calculations, and as a result it has been implemented in the EGSnrc user codes `CAVRZnrc` (Rogers et al., 2005) and `cavity`. The basic idea is to split a photon into N_s sub-photons with an uniform distribution of interaction sites along the initial direction. The weights of the split photons are adjusted to w_0/N_s , with w_0 denoting the original weight of the incident photon. The splitting number N_s is defined by the user and can be selected to yield the best efficiency.

The range-based Russian Roulette is an advanced technique for terminating electrons whose energy is too small to reach the cavity of the ionization chamber and thus cannot

contribute to the chamber dose directly. This technique can be understood as an extension to the simpler but approximate range rejection. Whenever an electron is about to take a step, its residual range in the medium with the lowest restricted stopping power present in the simulation geometry is evaluated. If this range is less than the smallest distance between the electron and an elementary, user-defined geometry surrounding the cavity, the electron is subjected to a Russian Roulette game with a user defined survival probability of $1/N_r$, $N_r > 1$. If the electron survives the game, it carries a statistical weight increased by a factor of N_r . These high weight electrons, often referred to as “fat” electrons, may generate high weight or “fat” photons in radiative events (Bremsstrahlung, electron impact ionization and, for positrons, annihilation). Such radiative interactions are therefore split N_r times to avoid fat photons reaching the cavity and causing large statistical fluctuations. Note that the range-based Russian Roulette is only applied to non-fat electrons. This technique achieves a similar effect to the commonly used range rejection (see chapter 1.5.4), but avoids the approximation of neglected photons set in motion by the rejected electrons and is thus a true VRT.

Although the above described techniques lead to an improved efficiency, the calculation of perturbation correction factors and the calculation of ionization chamber dose at more than one position inside a phantom is extremely time consuming. The goal of photon splitting is to increase the density of interactions throughout the whole simulation geometry. However, in typical setups, the ionization chamber and the water volume surrounding the chamber where electrons contributing directly to the cavity dose are generated, cover only a small fraction of the overall geometry. This implies that most electrons will be terminated immediately via Russian Roulette after being set in motion in a split photon interaction (*i.e.*, the time spent on simulating photon interactions that create electrons not contributing to the cavity dose is wasted). Hence, the `cavity` code was extended by various techniques for the special case of ionization chambers inside a phantom, as described in the following sections. The changes made in this work to the existing `cavity` code led to a new EGSnrc user code called `egs_chamber`¹.

2.1.1.2. The `egs_chamber` code for ionization chamber calculations

Photon Cross Section Enhancement - XCSE

The basic idea of XCSE is to increase the photon cross section Σ by a free parameter $b > 1$ thus decreasing the mfp to generate more secondary electrons along the path of a photon. This technique itself has been available in the EGSnrc user codes `DOSRZnrc` and `CAVRZnrc` for years, but is implemented here with some important extensions.

XCSE is comparable to the photon splitting mentioned. Generally, XCSE leads to an increased density of photon interaction sites by introducing a fictitious photon interaction, which leaves the direction and energy of the incident photon unchanged. The fictitious interaction cross section is taken to be $(b - 1)\Sigma$ so that the total photon cross section Σ_{tot} that includes the real interaction Σ and the fictitious interaction $(b - 1)\Sigma$ is

¹Since July 2009 the code is made a public domain software available at <http://www.irs.inms.nrc.ca/EGSnrc/EGSnrc.html>, distributed via the National Research Council of Canada.

$$\Sigma_{tot} = \Sigma + \Sigma (b - 1) = b \cdot \Sigma \quad (2.1)$$

When a photon arrives at an interaction site, it is split into a portion that undergoes a real interaction and a portion that performs a fictitious interaction (*i.e.*, a non-interacting portion). The interacting portion is simply the ratio of the real cross section Σ to the total cross section Σ_{tot} , *i.e.*, given by $1/b$. The non-interacting portion is $(b - 1)\Sigma/\Sigma_{tot} = 1 - 1/b$. The interacting photon will set electrons and/or scattered photons in motion all carrying a statistical weight of w_0/b , with w_0 being the statistical weight of the incident photon. One can then play a Russian Roulette game with a survival probability of $1/b$ for scattered photons and $1 - 1/b$ for the non-interacting portion of the incident photon so that all surviving photons carry again the initial weight w_0 . In practice, it is sufficient to generate a single random number r between zero and unity and keep scattered photons if $r \leq 1/b$ or the initial photon if $r > 1/b$. The result of all this is that the number of electrons set in motion by the incident photons is increased by a factor of b while the number of transported photons remains the same. The advantage of XCSE compared to photon splitting is that a position dependent enhancement factor b can be used, with b being set by the user on a region-by-region basis in the `egs_chamber` implementation.

Since individual regions of a phantom can be equipped with different XCSE factors b_i in the `egs_chamber` implementation, electrons of different statistical weight will be set in motion in the different regions of the geometry. To avoid fluctuations in weight, which may compromise the statistics of the cavity dose, electrons are handled in a special way. When an electron leaves a region, the XCSE factor b_2 of the new region is compared to the XCSE factor b_1 of the current region. If $b_2 > b_1$, the electron is split into b_2/b_1 copies, each carrying a fraction of b_1/b_2 of the initial weight, and each copy is transported separately. If $b_2 < b_1$, then the electron is subjected to a Russian Roulette game with a survival probability of b_2/b_1 , and the weight of surviving electrons is increased by b_1/b_2 . In this way all electrons moving in a region with a XCSE factor of b have a statistical weight of w_0/b , regardless of whether they were set in motion in this region or entered from another region with a different XCSE.

XCSE can be combined with range-based Russian Roulette. The `egs_chamber` implementation of this technique works in exactly the same way as described in the previous section. The only `egs_chamber` specific detail is that fat electrons are excluded from the splitting or Russian Roulette when moving between regions with different XCSE factors. This has no impact on the ionization chamber dose because fat electrons per definition can never enter the cavity.

In practical applications the XCSE technique is employed by using large XCSE factors in and around the chamber geometry. This is accomplished by surrounding the chamber geometry with one or more extra regions, called “shells” in what follows, which can easily be defined with the `egspp` geometry library (Kawrakow, 2006a). The parameter that can be adjusted for optimum efficiency are the XCSE factors and the size and shape of shells.

Correlated Sampling (CS) and Intermediate Phase Space Scoring (IPSS)

When calculating a depth-dose curve or a profile inside a water phantom using a real

ionization chamber model, each position of the chamber must be simulated separately. On the other hand, only a small fraction of the overall geometry changes from one position to another. To avoid a full, “brute force” re-calculation in all parts of the phantom, one can introduce an artificial volume, which surrounds all possible chamber positions needed for the depth-dose curve or profile as tightly as possible. The phase space (*i.e.*, particle type, energy, position, direction, statistical weight, and possibly additional user defined particle properties) of all particles that enter the artificial volume can be stored and the particle transport terminated immediately. The stored phase space can then be used as a source for all single chamber calculations at the different locations inside the phantom. In the `egs_chamber` implementation the user defines a “base geometry”, which consists of the phantom and the artificial volume for IPSS. All ionization chamber positions are described by separate simulation geometries that include the phantom but not the artificial IPSS volume. The transport is started from the common simulation source in the base geometry and stops at the artificial IPSS boundary. Subsequently, the particle transport is performed in all simulation geometries describing different chamber locations and dose to the cavity is calculated in a normal fashion. A comparable technique was introduced by Chibani and Ma (2007) for the GEPTS code. In `egs_chamber` an “on-the-fly” method is used, *i.e.*, phase space information is stored in memory to omit the use of phase space files as known from *e.g.* BEAM simulations (Rogers et al., 1995, 2006) thus avoiding the relatively slow speed of hard disk access and all other disadvantages associated with the use of phase space files (Kawrakow and Walters, 2006). It is worth noting that due to the flexibility of the `egspp` library, arbitrary IPSS volumes can be defined, including horizontal or vertical rectilinear tubes needed for profile or depth-dose curve calculations.

Figure 2.2 illustrates the use of IPSS and XCSE. Also shown is a necessary, special handling of electrons to combine IPSS with the XCSE technique efficiently. The surrounding geometry and the ionization chamber itself are equipped with a shell of phantom material of enhanced cross section and both shells overlap. If an electron from the phase space does not start inside the XCSE region of an ionization chamber geometry, a Russian Roulette game is applied with a survival probability of the inverse XCSE-factor. In this way, large numbers of electrons are only transported around the cavity for each chamber location.

The idea to simulate only the changing fraction of a geometry, can also be applied to the calculation of perturbation correction factors. For example, the calculation of the central electrode correction factor p_{cel} requires two simulations, one with the central electrode present and one without it. A correlated sampling scheme for the calculation of perturbation correction factors is therefore implemented in `egs_chamber`. It stores the random number generator state besides the phase space mentioned above, whenever a particle enters a set of user-defined geometry regions. These regions define the part that differs from one geometry to another. The statistical uncertainty of the dose ratio is evaluated taking into account the correlation of the two dose values brought about by using the same particles in both geometries and enhanced by employing the same random number sequence.

The combined uncertainty of a dose ratio $r = \frac{\bar{X}}{\bar{Y}}$ can be computed taking the correla-

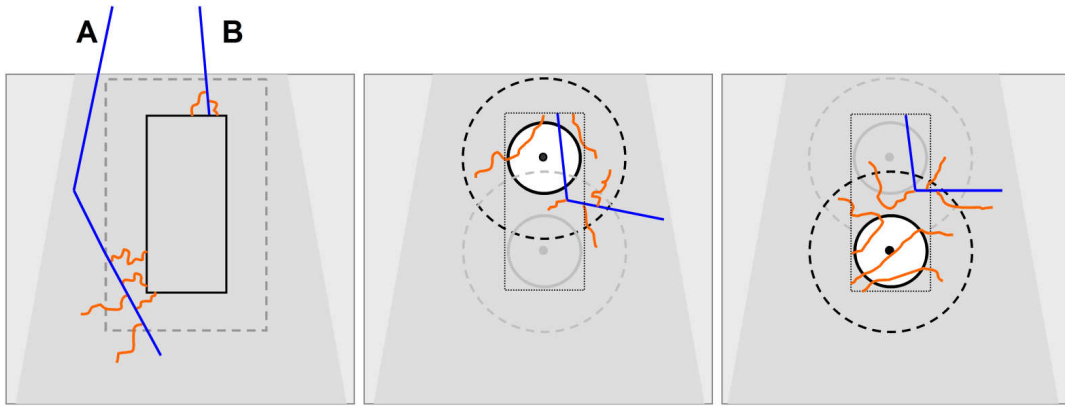


Figure 2.2.: Illustration of the combination of the IPSS and XCSE techniques for the simulation of two ionization chamber positions inside a phantom. In the left “base geometry” photon tracks A and B are started from the simulation source. The IPSS volume (left) surrounds both ionization chamber positions (middle, right). The IPSS volume (solid line box) in the “base geometry” is surrounded by a XCSE region (dashed line box). Each of the two chamber geometries has its own XCSE region that only partially overlaps with the XCSE region of the “base geometry”. The phase space of photons and electrons is stored and the transport is terminated as soon as the particles enter the IPSS region (left). The phase space is used for both ionization chamber positions as a particle source. Electrons must survive a Russian Roulette game, if they do not start inside the XCSE region of the respective ionization chamber geometry. In this illustration no IPSS electrons originating from photon A survive the game for the first chamber position (middle) and no IPSS electrons from photon B survive for the second (right).

tion into account with

$$\frac{s_{\bar{r}}}{\bar{r}} = \sqrt{\left(\frac{s_{\bar{X}}}{\bar{X}}\right)^2 + \left(\frac{s_{\bar{Y}}}{\bar{Y}}\right)^2 - \frac{2cov(X, Y)}{(N-1)(\bar{X}\bar{Y})}} \quad (2.2)$$

where $s_{\bar{X}}$ and $s_{\bar{Y}}$ are the statistical uncertainty for N particle histories on the calculated mean dose \bar{X} and \bar{Y} respectively. The term $cov(X, Y)$ is the covariance of X and Y , defined by

$$cov(X, Y) = \frac{\sum_{i=1}^N X_i Y_i}{N} - \frac{\sum_{i=1}^N X_i}{N} \frac{\sum_{i=1}^N Y_i}{N} \quad (2.3)$$

Hence, increasing the covariance reduces the combined statistical uncertainty of the dose ratio. The quantities in the above expression are scored during runtime. The scoring is already implemented in the `cavity` and thus in the derived `egs_chamber` code.

The correlated sampling technique was introduced for ionization chamber calculations by Ma and Nahum (1993a) and more details can be found in their paper, as well as in a more recent study by Buckley et al. (2004). In the `egs_chamber` implementation the

correlated sampling can be applied to calculate more than one perturbation correction factor and/or one or more perturbation correction factors at different chamber locations in a single run. The subsequent simulations of all geometries representing different ionization chamber constructions (*e.g.*, full chamber geometry, chamber without electrode, chamber without central electrode and without wall, etc.) start at the boundary of the user-defined regions. For example, if one wants to compute the wall and central electrode perturbation correction factors of a cylindrical chamber in a single run, the transport will start at the boundary of regions defining the chamber wall, even for the calculation of p_{cel} . The ability to recreate the exact random number sequence from the stored data ensures that the particle transport to the region of the central electrode is exactly the same for both simulations necessary for determining p_{cel} . Thus, the correlation between both doses is maximized, although some time is wasted by simulating particle tracks in some parts of the geometry twice.

2.1.1.3. Validation of implemented methods for variance reduction

To test the `egs_chamber` user code, both in terms of the correctness of the implementation and in terms of efficiency gain, several test calculations were run. The results were compared to simulations without any variance reduction techniques as well as to the results of simulations using photon splitting and range-based Russian Roulette with the original `cavity` code, which has been extensively benchmarked. In addition, these test calculations were used to determine optimum settings of the various variance reduction parameters in typical cases relevant for ionization chamber simulations.

In a first simple simulation geometry, small spheres of different radii and material at 10 cm depth inside a 30 cm x 30 cm x 30 cm water phantom were used to evaluate the XCSE technique. These spheres were surrounded by a spherical shell of varying thickness made of water. The photon cross section was increased by the same amount in the sphere and in the surrounding shell. The water phantom was irradiated by a divergent 10 cm x 10 cm photon beam with a source-surface-distance (SSD) of 100 cm and a published 6 MeV medical linear accelerator Bremsstrahlungs spectrum by Mohan et al. (1985).

In a second simulation, dose and the p_{cel} perturbation correction factor were calculated for a simplified cylindrical NE2571 Farmer type ionization chamber model inside a 50 cm x 50 cm x 50 cm water phantom at 10 cm depth for various beam qualities using Mohan et al. (1985) MV spectra and a ^{60}Co spectrum by Mora et al. (1999). All simulations were performed for a 10 cm x 10 cm field size and SSD= 100 cm. In these simulations CS, IPSS and XCSE are employed by defining an additional cylindrical shell of water around the chamber. The chamber were comparable to the one in figure 1.5, but neither included the stem, nor the waterproofing sleeve. Further, it was modeled as a simple cylinder without the conical tip.

To find the optimal parameters for the XCSE-technique the following procedure was used:

- The ionization chamber model was equipped with an extra region, leading to a shell of different size in all dimensions, filled with phantom material. The maximum

shell thickness that one needs to consider is given by the range of maximum energy electrons set in motion by the incident photon beam.

- For various shell thicknesses, the XCSE factor is changed and applied to all regions of the ionization chamber geometry and the extra region. Efficiency of the dose calculation is determined using equation (1.20) and short simulation runs.

In a final simulation setup the chamber dose and perturbation correction factors were calculated for the simplified Farmer chamber model as a function of depth along the central beam axis and as a function of distance from the central axis at 10 cm depth. A full BEAMnrc (Rogers et al., 1995, 2006) treatment-head simulation employing the DBS technique (see chapter 1.5.6). The BEAMnrc accelerator was compiled as a shared library and served as a particle source. The simulated beam was the 6 MV beam from the NRC Elekta Precise linac. Geometry specifications and parameters of the electrons incident on the Bremsstrahlung target are the same as those used by Kawrakow (2006b) and Tonkopi et al. (2005). The depth-dose curve was calculated for a 10 cm x 10 cm field at SSD = 100 cm, the profile for a 10 cm x 10 cm and a 40 cm x 40 cm field, also at a SSD of 100 cm. For these calculations, XCSE, CS, and IPSS at a surface enclosing all chamber positions described by a box were used. The simulations for the ionization chamber included the calculation of dose to the cavity and the calculation of the perturbation correction factors p_{cel} and p_{wall} in one run. The variance reduction parameters were adjusted for best dose efficiency.

2.1.2. Fast kerma-Based Calculations

As an alternative for the complete simulation of ionization chambers within the phantom, the use of kerma-based calculations was investigated. As will be discussed below, the commissioning of a linear accelerator model requires several iterative steps. Whenever the response of an ionization chamber has an impact on the calculated profiles, it needs to be included employing VRTs in the simulation as described above. This is certainly true, for regions, where CPD exists. On the other hand, when the change of ionization chamber response is of minor magnitude and when CPE exists, efficiently calculated kerma can be related to measured dose (see chapter 1.3.3.2).

The calculation of kerma is advantageous for two reasons. First of all the simulation of charged particle transport can be neglected, which requires a great fraction of overall simulation time. Secondly, collision kerma can directly be related to the photon fluence (see eq. 2.3). The calculation of fluence in a Monte Carlo simulation is straightforward since the fluence $\Phi = t/V$ can be related to the track length t of a photon inside a region of volume V .

Williamson (1987) proposed two methods of collisional (collisional) kerma calculation based on the track length of photons. In figure 2.3 the benefit of calculating kerma based on fluence is illustrated. The *linear* track length estimator uses the relation in equation 1.4 directly leading to

$$K_{\text{col}} = \Phi \cdot E \cdot \frac{\mu_{\text{en}}}{\rho} = \frac{1}{m} (t \cdot E \cdot \mu_{\text{en}}) \quad (2.4)$$

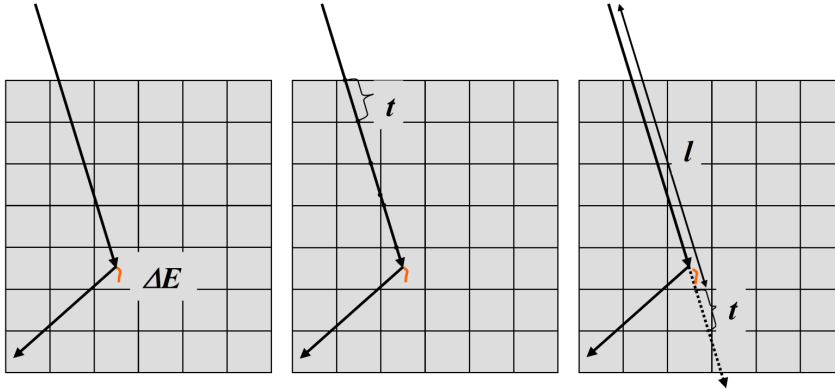


Figure 2.3.: Schematic illustration of different methods for the calculation of (collisional) kerma in a grid of regions. The straight line represents a photon interacting in one region, creating a secondary particle and being scattered out of initial direction. Left: In the analogue calculation the energy transferred to secondary particles ΔE is scored whenever a photon interacts inside the region. Middle: The *linear* track length estimator scores the fluence of photons in each region it passes with a track t , irrespective where the interaction actually occurs. Kerma is calculated based on equation 2.4. Right: The *exponential* track length estimator further uses photons to calculate the fluence even after being scattered. Their contribution is corrected for the attenuation along the path l . The kerma is calculated according to eq. 2.5.

The energy E as well as the mass m of the volume is known during particle transport and the step length t can be assessed as well. A second approach, the *exponential* track length estimator, further uses the contribution by photons to the fluence in one region even if the photon is scattered (see fig. 2.3). In this case, the collisional part of kerma is given by

$$K_{col} = \frac{1}{m} \left(E \frac{\mu_{en}}{\mu} e^{-l\mu} (1 - e^{-t\mu}) \right) \quad (2.5)$$

where μ denotes the attenuation coefficient at energy E . In the case of heterogeneous media along the path l , the attenuation needs to be considered for each region separately.

In both implementations of the track length estimator one needs precalculated data of the mass-energy absorption coefficient μ_{en}/ρ . The user code \mathfrak{g} (Rogers et al., 2005), was used to consistently calculate μ_{en}/ρ on a logarithmical grid for monoenergetic photons in water. During the simulation the single values for photons of energy E are interpolated with build-in interpolators as part of the `egspp` class library (Kawrakow, 2006a).

Track-length estimators for kerma are mainly known from low energy photon calculations as in brachytherapy or diagnostic x-ray simulations, where the range of charged particles can be neglected (Schmidt et al., 2009; Chibani and Williamson, 2005; Taylor and Rogers, 2008). Kawrakow and Fippel (2000) investigated the use for low energy

photons in high energy radiation therapy calculations. Since a fraction of dose is caused by Bremsstrahlungs-photons created at larger depth within the phantom, electrons must not be discarded although they are not directly needed for the kerma estimation. Therefore, a Russian Roulette option was implemented with subsequent splitting of RR-survivors, i.e. fat photons whenever a radiative event takes place.

The results of the track length estimator were compared to the calculations with the DOSXYZnrc code, employing the “howfarless” option (Walters et al., 2007). This option increases the efficiency of simulations by avoiding calculations of geometry-specific distances to voxel boundaries inside a homogeneous phantom. Presently, this is the most efficient way of calculating dose distributions inside a water phantom within the EGSnrc code system. A cubic 50 cm x 50 cm x 50 cm phantom with 0.5 cm³ voxels was irradiated with a 20 cm x 20 cm photon beam of 6 MV and 24 MV spectrum (see tab. 3.2).

2.1.3. Parallel Computing with the EGSnrc Monte Carlo Code

Despite the fact that the developed methods for variance reduction allow efficient calculation of ionization chamber dose and perturbation correction factors, the simulations still might require hundreds of hours on a single computer. The Monte Carlo method can ideally be used in conjunction with parallel computing, i.e. distributing the complete simulation task to different computer processors, since each simulated single event is independent of the others (see chapter 1.5.3).

For parallel computing used during the course of this work, a dedicated computer cluster was configured. It consists of 14 Intel[®] D 2.4 GHz, 12 AMD Athlon[™] 64 X2 Dual Core 4200+ and 4 Intel[®] Core[™]2 Quad 2.4 GHz PCs. The single PCs are connected via a 1 GBit/s Ethernet network and are accessible through a 100 MBit/s connection to the intranet. The system is based on Perceus² and the SUN Grid Engine³ and runs under Linux.

The slightly heterogeneous structure of the cluster is efficiently used with the EGSnrc built-in parallel functionality (Rogers et al., 2005). In brief, each node a job is submitted to, starts with a small fraction of particles, a so called “chunk”. During simulation each node takes chunks of particles and reports the number of particles left to a control file, until no particles are remaining. In this way slower CPUs take fewer chunks, while faster CPUs are able to take more chunks within the same amount of time. The node processing the last remaining histories combines the single results of all nodes.

2.2. Ionization Chamber Calculations for Reference Dosimetry

2.2.1. Photon Spectra

Collimated point sources were employed for the simulations of reference dosimetry. These sources were used in conjunction with published photon spectra found in liter-

²<http://www.perceus.org>

³<http://gridengine.sunsource.net/>

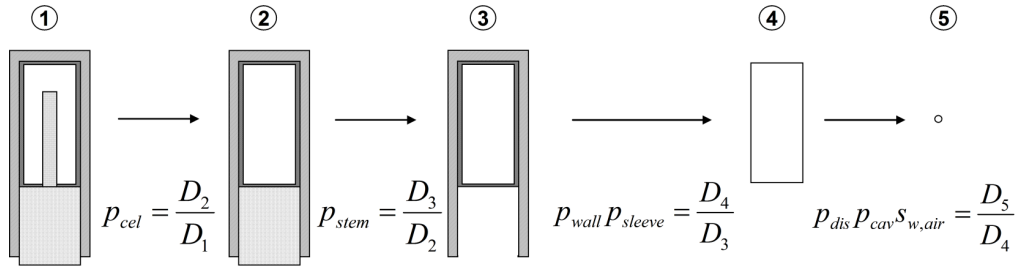


Figure 2.4.: Principle chain for the determination of perturbation correction factors used in this study. The various perturbation correction factors are given by the dose ratios from one step to another in the ionization chambers cavity (1-4) and the dose to a small portion of water (5). The step from model 3 to 4 can be further subdivided into separate calculation of p_{wall} and p_{sleeve} .

ature for ^{60}Co and various linear accelerator beams (Mora et al., 1999; Rogers et al., 1988; Sheikh-Bagheri and Rogers, 2002a; Mohan et al., 1985). They are all based on simulations of complete treatment heads as used in this study⁴ as well.

For consistency, beam quality specifiers $\%dd(10)_x$ (TG51) and $\text{TPR}_{20,10}$ (TRS-398) of those spectra were calculated. The $\%dd(10)_x$ for the spectra was estimated from a depth-dose curve which was calculated with DOSXYZnrc user code in a homogeneous $50 \times 50 \times 50 \text{ cm}^3$ water phantom in a SSD-setup and use of the “howfarless” option. A point source was placed at 100 cm source-surface-distance and collimated to 10 cm x 10 cm at the phantom surface. For the $\text{TPR}_{20,10}$ estimation, the dose in the reference volume in 10 cm and 20 cm depth in the water phantom ($50 \times 50 \times 50 \text{ cm}^3$) were calculated for each spectrum with the use of the `egs_chamber` user code in a SAD-type setup (see fig. 1.7).

2.2.2. Calculation of Perturbation and Beam-Quality Correction Factors

The calculation of the beam quality correction factor k_Q (see eq. 1.15) can be achieved by simulating the ionization chambers cavity dose D_c and relating it to the dose in water D_w at the point of measurement. One determines the factor f (see also eq. 1.8) in a beam of quality Q and relates it to f in a ^{60}Co beam

$$k_Q = \frac{f_{\text{Co60}}}{f_Q} = \frac{(D_w/D_c)_{\text{Co60}}}{(D_w/D_c)_Q} \quad (2.6)$$

The factor f can be interpreted as the inverse *response* of an ionization chamber compared to the ideal detector measuring D_w . The separate correction factors can be evaluated by calculating the ratio of chambers cavity doses with or without constructive details. In figure 2.4 a schematic procedure for determination of the above defined perturbation correction factors as used in this study is shown.

⁴Calculated beam qualities are summarized as part of the results in table 3.2

The efficient calculation of all single dose ratios is possible with the methods described, i.e. by applying the developed `egs_chamber` code. Ionization chamber geometries were modeled with the C++ class library `egspp` for the EGSnrc code system (Kawrakow, 2006a). The NE2571 Farmer-type chamber with a volume of 0.6 cm^3 was used for calculation of perturbation correction factors and the beam quality correction factors (see fig. 1.5). The NE2571 is a widely used cylindrical ionization chamber for absolute clinical dosimetry purposes. The dimensions of the chamber were partly taken from the original paper by Aird and Farmer (1972) and the data given in the IAEA TRS-398 dosimetry protocol. The chamber cavity has a diameter of 0.64 cm and a length of 2.4 cm and includes a 2.06 cm aluminum central electrode with 0.1 cm diameter. The wall is made of graphite with 0.061 g/cm^2 thickness. The model also includes a waterproofing sleeve made of 1 mm PMMA since the NE2571 itself is not waterproof. The chamber stem was modeled with portions of aluminum and graphite and includes a PTFE (TEFLON) insulator. Although the central dimensions and materials of the NE2571 are given in the dosimetry protocols, the construction of the chamber stem might be different for different Farmer-like chambers. For example Ma and Nahum (1995) modeled the chamber stem of a NE2571 as made purely of PMMA, whereas in the original Farmer paper and other publications it is made of PTFE (Russa et al., 2007). Hence, a second NE2571 geometry, with the material of the PTFE stem-parts (see fig. 1.5) changed to PMMA was investigated.

In order to calculate the dose to water D_w (see eq. 1.15) at the point of measurement, a reference volume was modeled as a simple disc of water placed in a phantom. The thickness of the disc was chosen with 0.025 cm and the radius with 1 cm. Various sizes were tested and no difference in calculated dose below the thickness of 0.05 cm was observed within a statistical uncertainty $\leq 0.05 \%$. Kawrakow (2006b) showed theoretically in a recent study, that those dimensions are adequate for 6 MV and 25 MV photon beams.

The chamber model and the reference volume were placed in a $30 \times 30 \times 30 \text{ cm}^3$ cubic water phantom. The centers of the chambers cavity volume and of the reference volume were located at reference depth. According to current dosimetry protocols TRS-398 and TG-51 the reference depth of 10 cm in a SSD-type setup (see fig. 1.7) and for some selected beams in a SAD-setup was applied. For the ^{60}Co beams a calibration depth of 5 cm was used in the SAD-type setup.

Besides the several published spectra used, a realistic model of a Siemens KD linear accelerator model, simulated with the BEAMnrc package (Rogers et al., 1995, 2006), was employed (see chapter 2.3.1 for further details). All dimensions, materials and parameters were set as specified by the manufacturer. Taking this beam model, the corresponding photon spectra were also calculated from a phase space file at the bottom of the accelerator and averaging over a $10 \text{ cm} \times 10 \text{ cm}$ field for a 6 MV and 15 MV beam.

For the simulations the transport cut-offs and secondary particle production thresholds were set to `ECUT= AE= 521 keV` and `PCUT= AP= 10 keV`. Other transport parameters were set to their defaults (see Ref. (Kawrakow and Rogers, 2006)). A detailed discussion on transport parameter selection for these calculations is given in chapter 2.2.3.

Prior to a systematic investigation of cross section uncertainties in chapter 2.2.3, the general influence of cross section variations was investigated for one parameter under current discussion, namely the mean ionization energy for graphite (Rogers and

Kawrakow, 2003). The standard data used in EGSnrc is $I = 78$ eV based on the ICRU Report 37 value (ICRU, 1984), while other authors refer to larger values up to 86.8 eV (Bichsel and Hiraoka, 1992). To analyze the influence of such an extreme change of cross sections, the calculated chamber beam quality correction factor k_Q with the changed value of the mean ionization energy was determined.

2.2.2.1. Calculation of p_{wall}

Besides the straightforward calculation of p_{wall} (see fig. 2.4) the wall correction can be calculated based on the theory of Almond and Svensson or its modifications (see eq. 1.12 in chapter 1.4.3). To allow a proper comparison between both methods which is independent of cross section databases, the needed quantities can directly be calculated with the EGSnrc Monte Carlo system. A similar approach was used by Buckley and Rogers (2006b), but here a more adequate estimation of α and τ (see eq. 1.12) corresponding better to the ideas of Almond and Svensson (1977) was used.

The FLURZnrc code was used to calculate the spectra inside the wall and sleeve of the cylindrical ionization chamber model placed in 10 cm depth inside a cylindrical water-filled phantom, irradiated by the different spectra. Subsequently the σ user code as part of the EGSnrc distribution was used to calculate the $\bar{\mu}_{en}$ values needed for the ratios of mass-energy absorption coefficients in equation 1.12. The SPRRZnrc code was applied to calculate the sprs between the different materials, also inside the cylindrical water phantom and also including the cylindrical model of the ionization chamber. Due to the fact that the RZ user codes are limited to cylindrical geometries, the chambers axis was placed parallel to the beam axis for these calculations. Still, this approach allows to include the effect of attenuation and scatter of primary photons inside the water, chamber wall, and sleeve. Further, the calculation of stopping-power ratios includes the change of electron spectra and the fact that no CPE exists, since the chamber model itself is included in the simulation.

The fraction of dose by electrons originating in the chamber wall and sleeve α and τ , was calculated with a slightly modified version of the `cavity` code. Usually α is calculated or measured as the ratio of dose to air in a chamber with a given wall thickness to dose to air in a chamber with full build-up thickness (Buckley and Rogers, 2006a). Using following approach corresponds better to the actual definition: electrons originating in the chamber wall and sleeve are “tagged” and their contribution to the cavity dose as a ratio is calculated at the end of the simulation. The chamber model was again placed inside the water phantom at 10 cm depth. Tagging of particles is made possible with the inherent `latch` variable of each particle, which can be modified during transport (Kawrakow and Rogers, 2006).

2.2.2.2. Replacement Correction and the Effective Point of Measurement

Following the schema in figure 2.4, the p_{repl} factor can be estimated with the ratio of a small reference volume of water and dose to a bare air cavity times the stopping-power ratios between water and air. Recently Wang and Rogers (2008) investigated various approaches to calculate the replacement correction p_{repl} . Besides the first approach men-

tioned here (SPR-approach called in their paper), they further used a calculation where the air in the cavity is replaced by water with density of air (LDW-approach). Therefore, the cavity in the geometry 4 in figure 2.4 contains water with density of 0.0012047 g/cm^3 . Appropriate material can easily defined with the PEGS-program. The ratio of dose in the water filled cavity with density of air and the reference dose yields directly the p_{repl} factor. This method has the advantage of avoiding the calculation of stopping-power ratios and being more efficient.

As mentioned in chapter 1.4.3, the alternative to use a individual perturbation correction factor is a constant shift of the ionization chamber. This shift ensures a match of the effective point of measurement (EPOM) of the air-filled cavity with the depth of measurement. This approach is favored by the German DIN 6800-2. To calculate the corresponding shift two different methods were investigated. Using the local gradient at the point of measurement, i.e. in 10 cm for reference dosimetry, the shift can be estimated from the p_{repl} factor. For this investigation the value of the LDW method was applied. As a second approach, the χ^2 minimizing method introduced by Kawrakow (2006b) was utilized. Generally spoken, this proposed method minimizes the position dependence of the ratio of dose to water to dose to cavity of an ionization chamber by applying a small shift Δz of the two depth-dose curves. The implementation was realized with a MATLAB⁵ script.

2.2.2.3. Calculation of the Energy Cut-Off Correction Factor p_{Δ}

The perturbation correction factor p_{Δ} accounts for the ionization chamber specific cut-off energy in the calculation of Spencer-Attix sprs. For the calculation of p_{Δ} various quantities are needed. Usually the energy Δ is estimated from the mean chord length of electrons inside the cavity and the energy of the corresponding CSDA range (see eq. 1.2) (Borg et al., 2000). A simple approximation for the mean chord length l of convex shaped volumes V with surface area A and irradiated isotropically is given by Attix (2004):

$$l = \frac{4V}{A} \quad (2.7)$$

For a more exact calculation of the electrons' chord length inside the cavity, the `cavity` user code was extended. During particle transport the single step lengths inside the defined air cavity are summed up. This particle property is accessible during transport via the parameter `VSTEP` (Kawrakow and Rogers, 2006). Generated secondary particles inside the cavity are also included in the calculation by transferring the so far covered chord length to the new particle. This was realized by introducing a new parameter to the particle properties in the source code. The total chord length of all actually crossing particles (neglecting the contribution of stoppers inside the cavity) is divided by their number and thus yields the mean chord length. The mean chord length was calculated in this way for the bare cylindrical cavity of the NE2571 and PTW31010 thimble chambers (see fig. 1.5) inside a water phantom.

For the estimation of the corresponding cut-off energy Δ , the range of monoenergetic electrons in air was calculated as a function of energy. Two different data sets for the

⁵<http://www.mathworks.de/>

stopping powers of air were used. This behavior can be controlled by setting the appropriate flag in the PEGS routines (`IUNRST`). The first data set ignores the discrete creation of secondary particles and thus enabling a CSDA type calculation (see eq. 1.2). The other data set includes the creation and yields a more realistic estimation of range, called “true” range subsequently. The simulations were carried out with a simple developed EGSnrc user code which calculates the mean total step-length inside a semi-infinite air volume. Simulations were carried out with cut-off energies of 1 keV, i.e. the lowest threshold possible in EGSnrc.

With the appropriate cut-off energy Δ the stopping-power ratios between water and air were calculated with the `SPRRZnrc` user code. The perturbation correction factor p_Δ is given as

$$p_\Delta = \frac{s_{w,a}^\Delta}{s_{w,a}^{10\text{ keV}}} \quad (2.8)$$

Since the perturbation correction factor itself will be used for the evaluation of k_Q (see chapter 1.4.4), it is straightforward to define a beam quality dependent correction factor k_Δ

$$k_\Delta = \frac{(p_\Delta)_Q}{(p_\Delta)_{Co60}} \quad (2.9)$$

This factor gives the actual necessary correction needed due to the introduction of a chamber specific cut-off energy Δ .

2.2.3. Uncertainty Estimation for Calculated Correction Factors

2.2.3.1. Fano Cavity Test

As described in chapter 1.5.5.2, the Fano cavity test can be used for benchmarking the condensed history implementation in a Monte Carlo code. Since the underlying electron transport algorithm in EGSnrc has been validated many times in literature, the test can be employed to validate the correct implementation of the geometry model. Such a test is necessary, because the `egspp` geometry module allows complex definitions of a simulation geometry, possibly not free of errors.

A model of the NE2571 ionization chamber completely made of water and filled low-density water ($\rho = \rho_{air} = 0.0012047 \text{ g/cm}^3$) was modeled. The original implementation of the `cavity` code (and the `CAVRZnrc` code as well), allows a calculation in the Fano mode. The ionization chamber model was irradiated with a ^{60}Co -spectrum of photons. The corresponding value of $\bar{\mu}_{en}$ was calculated with the `g` user code.

2.2.3.2. Expression of Uncertainties

The “Guide to the expression of uncertainty in measurement” (GUM) (ISO, 1995) divides two components of standard uncertainties: type A (*statistical*) and type B (*systematic*) uncertainties. While the type A uncertainty is easily described in a Monte Carlo

simulation by the standard uncertainty to the mean, usually given with a $1\sigma \approx 68.3\%$ confidence, the type B uncertainty estimation is not as straightforward. The statistical (type A) uncertainty of those MC calculated data can be minimized with the use of elaborate variance reduction techniques described, but the type B uncertainties remain. Therefore, the result of the calculated k_Q will be affected to some unknown amount by the uncertainties in underlying cross sections.

A general procedure for reporting the final uncertainty can be found in the GUM. Assuming N uncorrelated⁶ parameters (or input quantities) influencing in the result f , the combined u uncertainty follows

$$u^2(f) = \sum_{i=1}^N \left(\frac{\partial f}{\partial x_i} \right)^2 u^2(x_i) \quad (2.10)$$

with $\partial f/\partial x_i$ as the sensitivity coefficient for the change of the result due to a parameter x_i with a standard uncertainty u . The standard uncertainties u to the single parameters x_i are influenced by their underlying probability distributions, i.e. how likely a variation is. For example it can follow a Gaussian distribution with $u = \sigma$ or a rectangular distribution with $u = \sqrt{a/3}$, where a is the variation in the parameter. A so-called coverage factor defines the confidence interval for the distribution, where $k = 1$ covers 68% of the values for a normally distributed quantity.

The type B uncertainty can be investigated by directly changing one parameter to a known amount. This yields the product $(\partial f/\partial x_i)u^2(x_i)$ in eq. 2.10. Summing up all possible influences in quadrature quantifies the final uncertainty. This approach was used for example by Rogers and Kawrakow (2003), who calculated correction factors for air kerma primary standards. For a large amount N of possible parameters, each result of a changed input (e.g. the cross sections for graphite in the chamber wall) carries a statistical uncertainty. Thus, if the influence of a changed parameter is small, long calculation times are required to reduce the statistical uncertainty below the *systematic* change in f . Otherwise the final result will be governed by the single *statistical* uncertainties only.

2.2.3.3. Different Transport Options, Setup and Cross Sections Variations

The beam quality correction factors k_Q can be calculated with a small statistical uncertainty within a reasonable amount of time employing the methods described. For an investigation of the systematic uncertainties in the calculated values of k_Q due to cross section uncertainties and transport options selection, some tests were performed. Considering transport options, EGSnrc allows many adjustments. Therefore, the default settings were changed gradually to inspect changes to the calculated values of k_Q at the largest energy, i.e. the 25 MV spectrum (see tab. 3.2). The highest energy for k_Q was chosen, so that any energy-dependent influence on k_Q can be estimated in a conservative manner. A simulation with all EGSnrc transport defaults and cut-off energies of $ECUT = 521$ keV and $PCUT = 1$ keV was used. Different ⁶⁰Co spectra and small geometry variations were investigated as well. One might ask why not to use the most “exact” settings, i.e. using all possible interaction models for simulation, but the term “exact” is rather ambiguous.

⁶In fact it is not necessarily true, that the single quantities are uncorrelated.

Not all physical processes such as the electron impact ionization or triplet production are well documented in the EGSnrc manuals and are not benchmarked in detail yet. Further, turning on all options increases the calculation times.

The influence of uncertainties in cross sections on the calculated correction factors is not well known. In a first step databases for cross sections were changed. For a more general investigation of systematic uncertainties, the cross sections itself were varied in a second step, one at a time and for each material used in the geometry separately. In order to determine the final uncertainty without too long calculation times, a method proposed by de Carlan et al. (2008) was followed. Assuming a linear relationship, i.e. replacing $\partial f/\partial x_i$ by $\Delta f/\Delta x_i$, each single parameter, i.e. the cross sections for a material was changed to a large amount. If the resulting variation in f is ten times higher than its statistical uncertainty, one can use simply the slope in the linear variation to determine the sensitivity coefficient. For some parameters the change in f might still be below the statistical uncertainty. Instead of further increasing the variation by an unrealistic amount, the slope can be estimated in a conservative manner by adding the statistical uncertainty to the calculated change. This approach of calculating the sensitivity has the advantage, that coefficients in eq. 2.10 can be calculated separately for each parameter and a standard uncertainty u can later be assigned to it.

In order to determine the sensitivity, the photon mass attenuation coefficient of the different materials in the simulation geometry was scaled by a factor $\pm 5\%$. Since the uncertainty in the attenuation coefficient is different for the interaction contributions, the photoelectric effect, Compton effect, and pair production probability were changed individually by this factor. The general uncertainty of photo cross sections is assumed to be in the order of 1-2%. With the calculated sensitivity the contribution to k_Q was estimated based on a standard uncertainty u (see eq. 2.10) that was taken to be 2% for photoelectric effect and pair production and 1% for the Compton scattering.

It is known, that the largest amount of uncertainty in electron stopping powers arises from uncertainties in the mean excitation or ionization energy I . For electrons, a data set of different collisional stopping powers was generated with the PEGS program with a reduced mean ionization energy (see 1.1). Since the stopping powers are proportional to $\ln(1/I^2)$ the influence on the calculated k_Q is not likely to be linear. Hence, as a conservative estimate, the reduced/decreased mean ionization energy I was used with the linear approximation, overestimating the slope of a linear fit. The mean ionization energy was reduced by 50%. The resulting contribution of uncertainty to k_Q -values was based on the uncertainty given for I -values of the used materials given in the ICRU37 report (ICRU, 1984).

2.3. Ionization Chambers under Non-Reference Conditions

The investigations in the previous section pointed at the investigation of ionization chamber dosimetry at reference conditions. As will be shown in the results, a realistic photon spectrum source collimated to the reference field size is generally sufficient for the calculation of the correction factors. For the investigation of ionization chambers and cor-

responding correction factors under non-reference conditions (varying depth, field size, of-axis position) a photon spectrum collimated to a rectangle does not characterize a realistic radiation source sufficiently. Hence, a linear accelerator model was created and radiation transport through it was simulated, representing a real measurement as close as possible. The MC model of the linac was matched to measurements inside a water phantom. Individual perturbation correction factors of a commonly ionization chamber were calculated and the k_{NR} (see eq.1.17) factor was determined as a function of depth for three field sizes and as a function of central-axis distance. The condition of charged particle *dis*-equilibrium in the penumbra of a photon field was created with a simulation of an idealized, hypothetical photon field boundary, testing the ability of various detectors to deliver the relative dose profile with the lowest perturbation.

2.3.1. Modeling a Linear Accelerator Head

2.3.1.1. Strategies for Commissioning

A linear accelerator head was completely simulated, delivering a phase space used for ionization chamber calculations. The model was commissioned, i.e. the primary electron parameters were adjusted as described below, to match a corresponding measurement. For the simulations, the ionization chamber model of the measurement was included to avoid any influence of a possibly changed response, not known a priori. As mentioned in TG-106 (Das et al., 2008b) the improper choice of the detector may lower the quality of the collected beam data due to the variability of their response. Including the ionization chamber model in the Monte Carlo simulation will minimize this variability, since any possible perturbation is taken into account correctly. Hence, this circumvents the necessity to use different types of detectors for different tasks, e.g. high resolution diodes for small fields or penumbras but not for larger fields due to their non-constant energy response.

A model of a Siemens KD 6 MV linac was created for the BEAMnrc code. Technical drawings with dimensions and material specifications were provided by the manufacturer. The linac consists of several components as shown in the schematic figure 1.9. The components were simulated as follows:

- a gold target layer embedded into a steel container
- a tungsten primary-collimator with conical shape including the flattening filter made of steel
- a dose chamber with layers of aluminum-oxide defining two air cavities
- a 45° mirror made of glass with a thin aluminum layer
- target-focused tungsten jaws in y-direction
- an ideal 29 leaf tungsten MLC (without tongue and groove structures)

The mentioned studies in chapter 1.5.6 point out, that no definitive way of commissioning exists. Hence, the sensitivity of the initial electron parameters was investigated and used to find to an energy/size combination, which reproduced measured data at best.

Large open beam profiles, normalized to the central axis dose yielding an off-axis factor (OAF) were examined. The kinetic energy, size of Gaussian-shaped spot and mean angular spread was varied. Further, the influence of changing the width of the energy distribution also assumed to be Gaussian-shaped was investigated. Since some KD-type linacs were equipped with a tungsten-replacement kit (Faddegon et al., 2004), the impact of changing the target was tested. Most investigators neglect the exit window for simulations, but still some report the necessity to include it in order to get a good agreement to measured data (Francescon et al., 2000; Faddegon et al., 1999). Faddegon et al. (1999) demonstrated that the position of the primary collimator leads to a change in calculated profiles. This influence was not expected since the primary collimator spans a circular field of 50 cm diameter while the maximum field size investigated and shaped by jaws and collimator was 40 cm x 40 cm.

A set of wide open field profiles was calculated covering the energy range of 5.7-6.6 MeV in steps of 0.3 MeV and spot sizes with a Gaussian distribution and a full width at half maximum (FWHM) of 1-4 mm in steps of 1 mm. The resulting 16 simulated cross-profiles with each 36 independent ionization chamber positions inside the open field had a statistical uncertainty below 0.5%. This span in primary electron parameters was chosen, since the statements on matched energy and spot size given in literature for Siemens type of linacs vary at least in this range (Sheikh-Bagheri and Rogers, 2002b; Faddegon et al., 1999; Francescon et al., 2000). The energy and spot combination which yielded the best agreement in terms of a root mean squared deviation (RMSD) to spline-interpolated measured values. In order to validate the findings of the large fields profiles and to further improve the match to measurements, the penumbra a 3 cm x 3 cm fields and PDD curves were investigated. This seemed necessary, especially in the light of the above mentioned uncertainty in the exact density of the flattening filter.

For the BEAM simulations cut-off energies for transport and production thresholds of $ECUT=AE=700$ keV and $PCUT=AP=10$ keV respectively were used. Further, the full Bremsstrahlung angular-distribution (option "KM") was used. Using only the leading term increases the efficiency of BEAM simulations (Rogers et al., 2006), but was shown to be inaccurate considering the calculated large profiles (Smedt et al., 2005).

The `egs_chamber` code was connected to the BEAM-model as a shared library (see chapter 2.1.1.3). Dose was calculated in a model of the PTW31010 ionization chamber (see fig. 1.5) placed inside a 70 cm x 60 cm x 50 cm water phantom as used in the comparative measurements (see section below). The XCSE-parameters for the ionization chamber model were optimized for a 6 MV spectrum. Optimal splitting numbers in the DBS algorithm for the BEAM-model were chosen following Kawrakow's approach (Kawrakow, 2005). Accordingly, the efficiency was maximized for each field size simulated. The dose to the ionization chamber model inside the water phantom was calculated at 6 points within the field in different depths and thus efficiency was optimized based on mean statistical uncertainty for all positions. Within the DBS algorithm, electron splitting was turned on at a splitting plane at the bottom of the flattening filter, which is necessary for good contaminant electron statistics at the surface of the water phantom (Rogers et al., 2006). Range rejection was employed in the BEAM simulation for electrons below 2 MeV. Furthermore, splitting particles at the bottom of the accelerator lead to an increased efficiency for simulations including the ionization chamber, since most

of simulation time is needed for the BEAMnrc part of the simulation. Splitting and thus reusing one particle several times increases the probability for a contribution to dose in the ionization chamber.

2.3.1.2. Comparison to Measurements

Comparative measurements were performed in the field of the Siemens KD 6 MV beam at the University of Mainz. The PTW Tandem electrometer was used in conjunction with a MP3 water tank. Depth-dose curves, and profiles were measured and analyzed with the PTW-mc² software. A PTW 31010 ionization chamber was used for all measurements. A reference detector was placed in the periphery of the radiation field and used for monitoring the fluence for each set of measurement. Each reading of the field detector current was normalized to the current of the reference detector. In order to compare the measurements and simulations with each other, dose values were normalized, i.e. relative dose distributions were compared.

Whenever regions with a large dose gradient exist, small misplacements of a detector will lead to large deviations of dose distributions. In high gradient regions a distance to agreement is usually given for quantifying the deviation. For homogeneous phantoms an agreement of 1.5% within the beam and within 2 mm in the penumbra can be considered as a realistic requirement for acceptability (IAEA, 2004; Papanikolaou et al., 2004).

2.3.1.3. Calculation of Monitor Chamber Backscatter

For the varying field sizes the dose to the monitor chamber in a linac (see fig. 1.9) may be affected, since for narrow jaw settings particles are scattered back. If no special backscatter plate is included in the linac the monitor chamber will quicker measure the preset number of monitor unit and terminate the beam. The magnitude of this effect is generally a few percents (Verhaegen and Seuntjens, 2003). The decreased output is automatically included in corresponding measurements, but for a direct comparison with a Monte Carlo simulation the effect needs to be taken into account. Although Verhaegen and Das (1999) could not find any evidence for monitor chamber backscatter in a Siemens MD2 linac, which is comparable to the KD type used here, some simulations were performed to rule out any backscatter effect.

The upper portion of the KD up to some portion of the flattening filter was simulated in BEAMnrc. Starting from the lower portion of the flattening filter the monitor chamber, mirror and the jaws were modeled with the egsp library and the dose to the monitor chamber (with an increased XCSE-factor) was efficiently calculated with the `egs_chamber` code. The approach of splitting the simulation has the advantage, that the correlated sampling technique efficiently calculates the dose ratios for different jaw settings in one simulation run. The small contribution of backscattered particles makes the calculation with small statistical uncertainties necessary. Due to the strong correlation of single dose values, which differ only by the backscattered contribution, the dose ratios uncertainty decreases drastically when taking correlations into account (see eq. 2.2).

2.3.2. Ionization Chamber in the 6 MV Field of a Linear Accelerator

Perturbation factors were calculated for the PTW31010 model (see fig. 1.5) with the methods described in the sections above. For the calculation of the f -factor (eq. 2.6) a small cubic voxel of 1 mm side length was simulated. The size of the voxel was surrounded by a shell for XCSE with optimized factor considering efficiency. The factors were calculated within the field inside a water phantom at different depths and off-axis positions.

The perturbation correction factors were normalized to the value of the reference field (10 cm depth and 10 cm x 10 cm field size), giving insight to the change of perturbation correction factors and yielding the overall correction k_{NR} (see eq. 1.18).

Further, the mean energy was calculated with the FLURZnrc code. Since the code can handle only cylindrical symmetric geometries and corresponding regions as cylindrical shells, the jaws/MLC were replaced by a single focused collimator with a circle diameter whenever profiles were investigated. Otherwise artifacts would have been resulted when using rectangular fields with circular regions. The same applied for the calculations of sprs employing the SPRRZnrc code.

2.3.3. Ionization Chambers and Other Detectors Under Charged Particle Dis-Equilibrium in the Penumbra of a Photon Beam

The most severe perturbation of electron fluences and thus radiation detector response can be expected under conditions of charged particle disequilibrium. An idealized field boundary was created with a sharp beam penumbra, which allows the investigation of behavior of various detectors regarding their averaging properties and behavior under CPD. As a source a simple photon spectrum of a Siemens KD linac (see tab. 3.2) was used irradiating a small water phantom (radius = 5 cm and thickness = 10 cm) with a parallel, circular beam of 5 cm diameter. Various detectors were placed at 2.5 cm depth, allowing for CPE at the field center, and were moved along the field penumbra. Using this idealized setup allows comparison of detectors with each other and avoids long calculation times for the complete treatment head as used in the previous chapter. In fact, the results somehow depend on the focal spot size and the exact construction of beam limiting collimators as discussed in chapter 1.4.5. Still, for a general investigation of the behavior of various detectors and possible order of magnitude for corrections however, the setup is advantageous. Further, it will allow future simulation based comparisons under exact same conditions not influenced by any accelerator specifics. Figure 2.5 shows the setup used for this investigation.

The circular beam allows for the definition of rings for efficient determination of dose and fluences to water along the field, since the rotationally symmetric volume in the RZ-geometry can be made comparatively large while spatial resolution remains high. The water volume had a thickness of 0.5 mm and a width of 0.5 mm as well and its geometrical center of mass was assumed to represent the dose to a point. Due to the finite dimensions this assumption is only valid to a certain amount, but is a compromise between

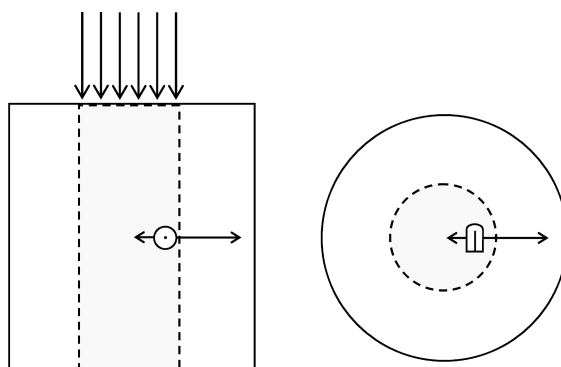


Figure 2.5.: Setup for the investigation of detectors in the idealized beam penumbra. Left: a section through the cylindrical water phantom, which is irradiated from top with a parallel beam of photons. The detectors are moved perpendicular to the central axis. Right: top view on the cylindrical phantom with the circular area covered by the beam.

simulation time and accuracy. As mentioned, Kawrakow (2000b) proposed a method to estimate the error introduced due to the finite voxel size. Using his approach, the error can be expected to be $\sim 1\%$ at the largest gradient within the penumbra. Electrons and photon fluences were calculated in the small volume as well as the Spencer-Attix stopping power-ratios. The perturbation correction factors for the PTW31010 chamber were determined.

Table 2.1 summarizes the investigated types of detectors and their properties. Besides the PTW31010 chamber three other air-filled ionization chambers of the “pinpoint” type were investigated. They all have a semi-spherical ending and a aluminum electrode, except the PTW31006 which is equipped with an electrode made of steel. The detector axis of all ionization chambers was placed perpendicular to the beam axis.

The TLD detectors were simulated as rods with their rotation axis in in depth of measurement and perpendicular to the beam axis. The radiochromic film of type MD-55 was modeled according to Paelinck et al. (2003). It consists of seven thin layers, with the active microcrystalline monomeric dispersion of $15\mu\text{m}$ coated on flexible polyester. A complete sheet of film was inserted into the phantom and dose was scored in concentric rings of the sensitive layer with 0.5 mm width, which has a density of 1.3 g/cm^3 . The modeled diode represents the IBA stereotactic field diode (SFD). The detector consists of a silicium chip within an epoxy resin housing. Within the chip a sensitive volume of 0.06 mm thickness and 0.6 mm diameter results. As stated by McKerracher and Thwaites (2006) it is similarly constructed as the unshielded electron field diode of IBA, which was used in a simulation based study of Wang and Rogers (2007) on behavior in electron beams. Therefore, the material composition and basic dimensions were taken from Wang and Rogers (2007) and adapted to the dimensions given in (McKerracher and Thwaites, 2006) and the IBA brochures for the SFD. Its axis was oriented parallel to the beam axis. The liquid filled ionization chamber was modeled according to the information given by the manufacturer PTW. It consists of a small disc of sensitive liquid and a housing made of polystyrol. Its construction is comparable to a plane-parallel chamber with a

Table 2.1.: Characteristics of detectors used for investigation in the field boundary. The radius r and the length l (or thickness t) are given for the sensitive volume, which corresponds to the specified value given by the manufacturer.

detector type	volume cm^3	sensitive material	remarks
PTW31010 (<i>semiflex</i>) ¹	0.125	air	see fig.1.5
PTW31014 (<i>pinpoint</i>) ¹	0.015	air	$r = 1 \text{ mm } l = 5 \text{ mm}$
PTW31006 (<i>pinpoint</i>) ¹	0.016	air	$r = 1 \text{ mm } l = 5 \text{ mm}$
PTW31016 (<i>pinpoint</i>) ¹	0.016	air	$r = 1.45 \text{ mm } l = 2.9 \text{ mm}$
TLD rods	0.00235	LiF	$r = 0.5 \text{ mm } l = 3 \text{ mm}$
MD-55 film ²	—	polydiacetylene	$t = 0.015 \text{ mm}$
IBA SFD ³	1.69×10^{-5}	Si	$r = 0.3 \text{ mm } t = 0.06 \text{ mm}$
LIC ¹	1.72×10^{-4}	iso-octane ⁴	$r = 1.25 \text{ mm } l = 0.35 \text{ mm}$

(1) Dimensions and material properties provided by the manufacturer.

(2) Dimensions and material properties taken from Paelinck et al. (2003).

(3) Dimensions and material properties taken from manufacturers brochure, Wang and Rogers (2007) and McKerracher and Thwaites (2006).

(4) iso-octane: 2,2,4-Trimethylpentane.

collecting electrode made of graphite.

The f -factor was calculated for each detector at each position within the field and normalized to the value at the field center, where CPE exists. Although the center of the 5 cm diameter field can not be considered as a reference field, the resulting ratio can still be understood as a measure of deviation from reference conditions. As long as CPD exists, the changed field size from a reference field with 10 cm x 10 cm to smaller field sizes causes no severe change in k_Q (see chapter 3.3).

In order to quantify the influence of the different detectors on relative dose distributions the penumbra broadening was determined. The width between 80% and 20% of the relative dose distribution was calculated for the piece of water as the ideal detector and compared to the width of the various detectors, yielding the positive or negative deviation due to broader or narrower penumbra.

3. RESULTS AND DISCUSSION

In the section 3.1.1 of this chapter the performance of the developed variance reduction techniques is presented for some general test cases. Section 3.2 presents results for simulations of dosimetry under reference conditions. These results include calculations of individual perturbation correction factors and comparison to existing data. The underlying systematic uncertainties of the calculations are investigated. In section 3.3 the matching of the linear accelerator model is described and its application to the calculation under non-reference conditions is discussed. The properties of various detectors under conditions of idealized charged particle dis-equilibrium are demonstrated.

3.1. Increasing Efficiency

3.1.1. Ionization Chamber Related Calculations in Photon Beams

3.1.1.1. Investigation of Gain by XCSE

As described in chapter 2.1.1.3, small spherical geometries were used for the general validation of the implemented techniques. Figure 3.1(a) shows the relative efficiency, i.e. the efficiency compared to the case with no VRT, as a function of the XCSE factor for the computation of dose in a 0.5 cm radius spherical water-filled cavity placed at 10 cm depth in a water phantom. Each curve represents a simulation geometry with a different spherical shell thickness with increased cross sections surrounding the cavity.

Two observations can be made from the figure. First, the efficiency increases with increasing XCSE-factor and reaches a peak due to the larger probability, that source photons contribute to the chamber dose. Further increasing the XCSE factor results in a decrease of efficiency due to the longer simulation time required while no extra information, i.e. decreased statistical uncertainty, is gathered from the additional electrons generated by the same set of photons. As mentioned, efficiency is affected by simulation time and statistical uncertainty. Secondly, the efficiency increases with the thickness of the surrounding region reaching a maximum at 1 cm, beyond which it drops with increasing thickness. The thicker the shell, the more secondary electrons are set in motion in the regions of increased cross section. As figure 3.1(a) indicates, optimum values for the XCSE factor and for the size of the shell exist, which lead to a gain in efficiency of about a factor 130 for this type of simulation. This is about a factor of 7 more efficient than using the `cavity` photon splitting technique with a splitting number, optimized in terms of efficiency.

The optimum XCSE factor depends on the size and material of the cavity. In figure 3.1(b) efficiency results are shown for simulations with different sizes of the sphere. Furthermore, the material inside the sphere is changed from water to air for the smallest diameter. The figure indicates that the gain in efficiency increases with decreasing cavity volume. This is expected because the probability of a dose deposition per initial source

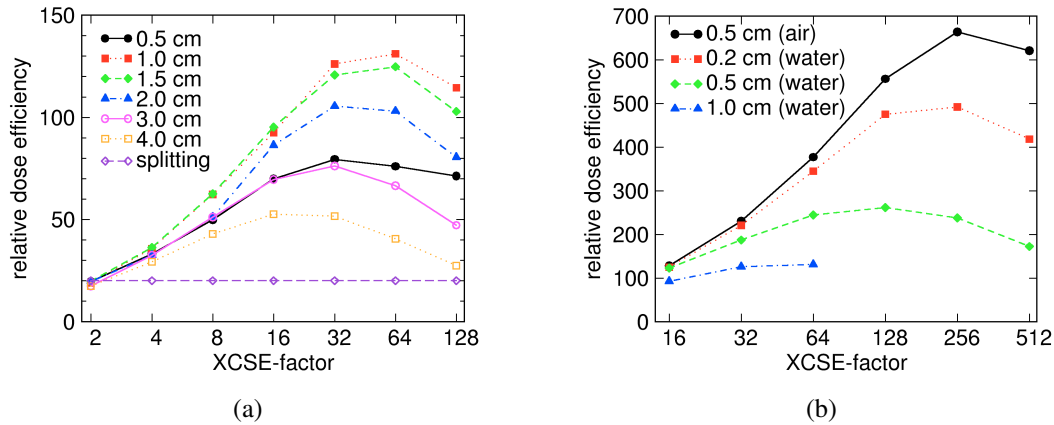


Figure 3.1.: Efficiency gain by the use of the XCSE-technique. (a): Relative efficiency as a function of XCSE-factor for various thicknesses of the shell surrounding a small *water-filled* sphere within a water phantom. In comparison the efficiency gain when using the generally known photon-splitting technique is shown. (b): Relative efficiency as a function of XCSE-factor for spheres of various diameter filled with water or air.

photon decreases with decreasing sphere size. Hence, a local increase in photon interaction density leads to more secondary electrons that deliver dose. The same applies for the small air-filled spherical cavity of 0.5 cm diameter, where the probability for dose deposition is even smaller. In this case the (relative) peak efficiency is about a factor of 650 better compared to simulations without variance reduction techniques. For comparison, the efficiency for the `cavity` photon splitting technique with optimum splitting number lies at roughly a factor of 16 in this case.

In principle, one could define several shells around the cavity with a XCSE factor gradually increasing from unity towards the maximum XCSE factor used in the cavity and in the first surrounding shell. The efficiency of calculations with more than one shells were tested for varying shell numbers and strategies of increasing the XCSE factors. Although slightly better efficiency ($\sim 10\%$) could be obtained in some of the simulations, it was deemed that this small increase of efficiency is not worth pursuing given the increased complexity of geometry definition and the much more difficult process of obtaining optimum XCSE factors and shell thicknesses. Thus, in all subsequent simulations reported here a single enhancement region around the chamber was used.

3.1.1.2. Application to Ionization Chamber Dose and Perturbation Correction Factors

For the simulations of the NE2571 ionization chamber in a water phantom, the surrounding cylindrical shell and XCSE-factor were adjusted to deliver the best efficiency. In figure 3.2(a) the relative efficiency for the calculation of dose to the cavity is shown as a function of the beam quality specified as $\%dd(10)^1$. The efficiency gain drops with

¹See also table 3.2

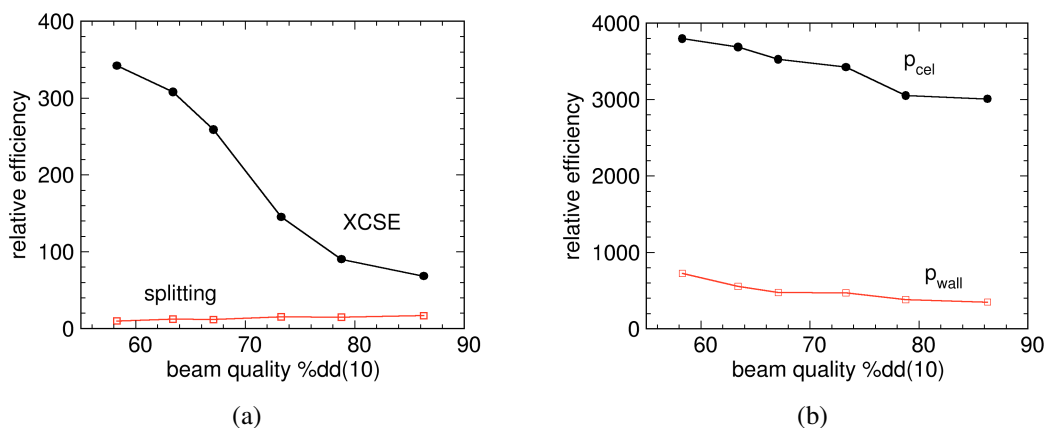


Figure 3.2.: Efficiency gain for dose (a) and perturbation correction factor calculations (b) as a function of beam quality. A cylindrical NE2571 ionization chamber was placed in 10 cm depth within a water phantom and irradiated by photons of different spectra.

increasing energy, but is significantly higher than using the `cavity` photon splitting technique even at the highest investigated energy of 25 MeV by roughly a factor of 3.5. Table 3.1 summarizes the parameters delivering best efficiency in this situation. In general, the XCSE-factors are larger for lower energies.

When calculating perturbation correction factors and using the correlated sampling technique the optimum parameters differ from those when just calculating cavity dose. Best efficiency for perturbation correction factors is achieved with thinner shells and higher XCSE factors as seen in table 3.1. The relative efficiency for the p_{cel} calculations varies with a slight energy dependence between 3800 for ^{60}Co and 3000 for the 25 MeV photon beam. In figure 3.2(b) the efficiency is shown for the calculation of perturbation correction factors as a function of beam quality. The extreme gain in efficiency when calculating p_{cel} according to equation 2.2 can be explained by the high correlation of single dose depositions, which is increased drastically by the XCSE technique.

The most realistic but challenging situation is the calculation of ionization chamber doses and perturbation correction factors when a realistic beam source is included in the simulation. For the simulation of the complete profiles and depth-dose curves including the treatment head of the 6 MV NRC ELEKTA linac, efficiency gain for dose calculations was in the order of a factor 500 and up to 10^4 for the calculation of the p_{cel} perturbation factor.

3.1.1.3. Summary

The above results demonstrate the ability of the implemented methods to dramatically improve the efficiency of ionization chamber dose and perturbation factor calculations. The developed methods for variance reduction implemented are not new and in fact they have been employed in one way or another in previous publications. The novelty of the approach presented here consists of the unique combination of these techniques that

Table 3.1.: Optimum cylindrical shell thickness and XCSE factor for dose and p_{cel} or p_{wall} calculations for a Farmer ionization chamber in a water phantom at 10 cm depth in order to achieve the relative peak efficiency. The corresponding values for the relative efficiency in a dose calculation are shown in Figure 3.2(a).

beam quality %dd(10)	<i>dose</i>		<i>perturbation correction factors</i>	
	shell thickness cm	XCSE-factor	shell thickness cm	XCSE-factor
58.3	0.5	256	0.25	512
63.4	1	256	0.25	256
67.1	1	128	0.25	256
73.3	1	64	0.25	256
78.8	1	32	0.25	256
86.3	1	16	0.25	128

results in a dramatic improvement of simulation efficiency when calculating perturbation correction factors and ionization chamber doses (or dose to any volume that is small compared to the irradiated volume).

3.1.2. Fast kerma-Based Calculations

The application of the implemented track length estimator was tested for a homogeneous phantom made of water and simple photon spectrum sources. Figure 3.3 compares the results of the track length estimator with those of the DOSXYZnrc code with the best VRT settings available up to date. In regions of CPE both results agree within the statistical uncertainty of $\leq 0.25\%$. The track length estimator for the 6 MV beam was up to 130 times more efficient in the exponential mode and 34 times in the linear mode, respectively. The efficiency gain for the largest depth was up to a factor 84 and 38 in the 24 MV beam.

The large increase in efficiency for kerma calculations compared to full dose calculations encourages for the use of the kerma scoring technique, whenever kerma approximation is acceptable. This is the case for points within a homogeneous phantom under transient CPE, which might be used for the commissioning of a linear accelerator. Further it must be ensured, that the ionization chamber used during measurement has a constant response, i.e. the perturbation correction factors as described in equation 1.18 need to be constant. Since it was not known in advance, if this requirement was fulfilled, the use of the track length estimators was not exploited and further. However, for future investigations this technique might be a valuable alternative to full dose calculations, at least in the first steps of the commissioning procedure.

3.2. Calculations for Reference Dosimetry

In the following sections the calculated individual perturbation correction factors of a NE2571 Farmer-type ionization chamber will be presented. Special attention is paid

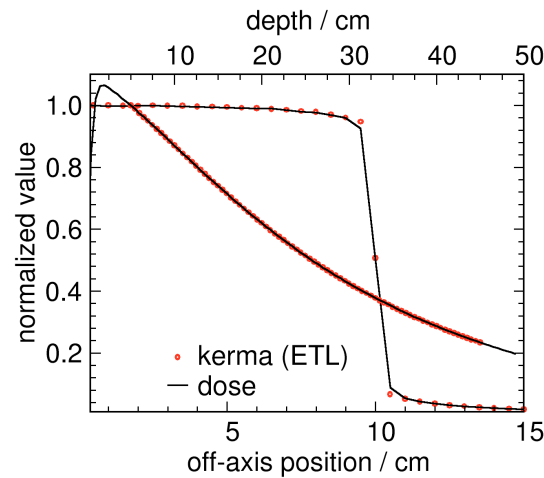


Figure 3.3.: Calculated distributions of kerma employing the exponential track length (ETL) estimator and full dose distributions as result of DOSXYZnrc calculations.

to the calculation of wall correction factors and the replacement correction, where the largest deviations to existing data can be found. The currently introduced correction factor p_{Δ} of the DIN 6800-2 protocol is investigated for two typical ionization chamber dimensions. Further, an analysis of systematic uncertainties in calculated beam quality correction factors k_Q is presented.

3.2.1. Perturbation Factors

The individual perturbation correction factors were calculated according to figure 2.4. Note that the chain defined there is more or less arbitrary, since no clear definition exists for the order in which the factors have to be applied. The common assumption is, that all factors are small and independent of each other, hence the order in the chain is of no importance.

Calculated beam quality specifiers for the used photon spectra are given in table 3.2. Most of the following data will be presented in terms $TPR_{20,10}$ as used in the international IAEA TRS-398 protocol or the German dosimetry protocol DIN 6800-2. Though with the data in the table and a fit through one specifier as function of the other allows a consistent conversion between both (Kalach and Rogers, 2003).

3.2.1.1. Central Electrode Correction Factor p_{cel}

The factor p_{cel} describes the influence of the central electrode on the electron fluence in the cavity of an ionization chamber. The factor itself is generally less than unity, indicating an increased dose due to the presence of the aluminum within the air-filled cavity. The beam quality dependency is caused by the larger probability of photon interactions at lower energies (see fig. 1.2). The calculated values in figure 3.4 are comparable to those of Buckley et al. (2004) and Ma and Nahum (1993b), showing an almost linear

Table 3.2.: Calculated beam quality specifiers for the various spectra found in published works, based on Monte Carlo simulations. The statistical uncertainties in the depth-dose curves used for determination of $\%dd(10)_x$ were not exceeding 0.3% in voxels of 1 mm thickness and 1 cm width. The statistical uncertainty in the $TPR_{20,10}$ values was generally below 0.2%.

Beam description	$E_{nominal}(MV)$	$\%dd(10)_x$	$TPR_{20,10}$
^{60}Co Eldorado 6 ¹	-	58.4	0.572
^{60}Co Eldorado 6 ²	-	58.6	0.572
Varian Clinac ³	4	62.9	0.621
	6	66.2	0.662
	10	74.2	0.736
	15	77.8	0.755
	18	81.3	0.780
Siemens KD ³	6	67.6	0.676
	18	78.7	0.768
Elekta SL25 ³	25	83.7	0.797
Varian Clinac ⁴	24	86.3	0.806

(1) (Mora et al., 1999)

(2) (Rogers et al., 1988)

(3) (Sheikh-Bagheri and Rogers, 2002a)

(4) (Mohan et al., 1985)

trend of changed chamber response between 0.8 % and 0.5 %.

Remaining minor discrepancies between the published values of p_{cel} might be attributed to the different photon cross sections, transport options, more detailed chamber model used in this study and the fact that a waterproofing sleeve was present in the calculation (see fig. 1.5). Further, a point source was used collimated to a rectangle, while the other authors used parallel beams.

Besides the published spectra, results are shown for the Siemens KD linear accelerator model, either as a full BEAM-model or the photon spectra only. Although the calculated spectra do not contain any spatial information of the full phase space, the energy is averaged over the full field size and no contaminant electrons are included, the results follow the same linear trend. Merely the calculated beam quality specifier between the full BEAM-source and the collimated point-source with the corresponding spectrum differ. This observation was made for all other perturbation correction factors. Thus, the results for the Siemens KD model and corresponding photon spectra are not included in the following figures. Likewise, no difference in the perturbation correction factors were observed for the two different ^{60}Co spectra, differing mainly in the resolution of energy bins, and thus in the following only the results for the more recent spectrum of Mora et al. (1999) are shown.

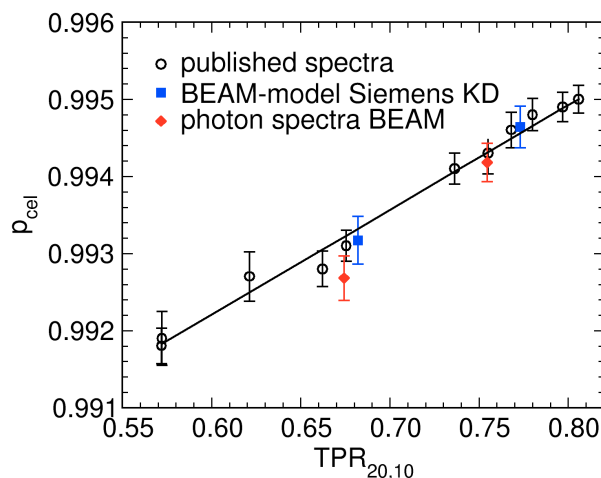


Figure 3.4.: Calculated perturbation correction factor p_{cel} for the central electrode of a NE2571 chamber as a function of beam quality $\text{TPR}_{20,10}$. The published spectra are characterized in table 3.2. The BEAM-model (yielding a complete phase space) of the Siemens KD includes the full phase space as a source for 6 MV and 15 MV. The 'photon spectra BEAM model' were calculated with photon spectra from the phase space of the Siemens KD BEAM model. A linear fit of form $p_{\text{cel}} = 0.0136 \cdot \text{TPR}_{20,10} + 0.984$ is shown for all points of the published spectra.

3.2.1.2. Stem Perturbation Correction p_{stem}

The influence for a chamber stem is generally ignored in the calculation of beam quality correction factors in all current dosimetry protocols. This seems to be justified taking a look at the small magnitude of the perturbation correction factors shown in figure 3.5. The p_{stem} factor varies in the range of tenth of a percent in the beam quality range. Although the absolute value of the p_{stem} perturbation correction factor is different for the two stem implementations (PTFE vs. PMMA portions), the shape is almost identical. Hence, due to the normalization of beam quality correction factors k_Q relative to ^{60}Co (see eq. 1.15), the influence of the actual stem construction for the two investigated materials is negligible.

3.2.1.3. Chamber Wall Correction p_{wall}

The combined effect of the chamber wall and the waterproofing sleeve is shown in figure 3.6, which bares an almost linear decrease of chamber response and a resulting increased perturbation correction factor with energy. The influence changes the chamber response by $\sim 0.6\%$ over the full energy range. The separation of the wall and sleeve perturbation correction factors reveals the large influence of the sleeve solely. The individual perturbation correction factor p_{wall} shows a more constant distribution than the combined effect of wall and sleeve.

According to IAEA TRS-398 the p_{wall} value including a 0.5 mm waterproofing sleeve is 0.992 in ^{60}Co and therefore smaller than the presented value here of 0.9980 \pm 0.0005

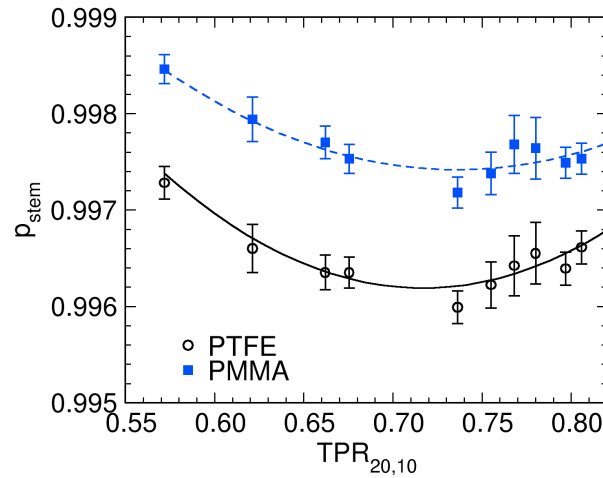


Figure 3.5.: Perturbation factor p_{stem} for the presence of a chamber stem in the NE2571 model. The circles correspond to the model shown in figure 2.4. The solid squares represent the results, when all portions of PTFE in the model are replaced by PMMA. Quadratic polynomials of type $p_{\text{stem}} = a \cdot (\text{TPR}_{20,10})^2 + b \cdot \text{TPR}_{20,10} + c$ with parameters $a = 0.0385$, $b = 0.0567$, $c = 1.0183$ for PMMA and $a = 0.0564$, $b = 0.0809$, $c = 1.0252$ for PTFE are given.

for a 1 mm sleeve. Still, one could argue that the stated uncertainty of the IAEA TRS-398 with 0.5% leads almost to an agreement with the calculated value here, but obviously a general problem exists for describing the wall perturbation.

As discussed by Buckley and Rogers (2006b) Monte Carlo calculated values of p_{wall} do not agree with the ones based on the formalism by Almond and Svensson (1977) as used in current dosimetry protocols, especially at lower energies. Figure 3.6 further includes the calculated values for the wall perturbation according to the theory by Almond and Svensson (1977) (see eq. 1.12). The underlying values α varied from 47% (^{60}Co) to 8% (25 MV) and τ from 35% to 10% respectively (see chapter 2.2.2.1). These calculations include the more appropriate estimation of α and τ and the absorption coefficients and sprs as well. However, these calculations do not allow for an agreement to the direct calculation. The value at ^{60}Co based on the AS-theory calculations is in excellent agreement to the one given in the TRS-398 protocol, but deviates significantly from the one resulting of the direct calculation. This result once more demonstrates the problem with the commonly but inadequate description of the complex wall perturbation by an analytical description.

3.2.1.4. Replacement Correction and the Effective Point of Measurement

Calculated values for the product of p_{dis} and p_{cav} yielding p_{repl} are given in figure 3.7. Usually, the p_{cav} perturbation correction is assumed to be unity in high-energy photons and the p_{dis} correction only dependent on the gradient. The calculated values presented here should therefore only reflect the factor p_{dis} . The data available on p_{dis} which is incorporated in current dosimetry protocols, is based on the studies of Cunningham and

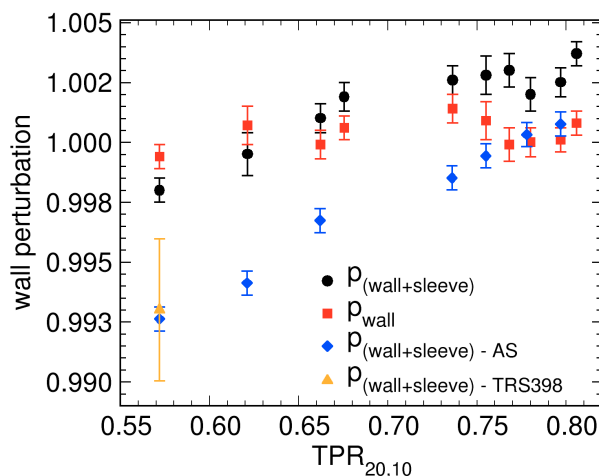


Figure 3.6.: Wall perturbation correction factor p_{wall} as a function of beam quality for the NE2571 model. The circles are results, when a waterproofing sleeve of 1 mm PMMA is included. The solid squares are the perturbation correction factors for the graphite wall only. Further, the result of the Almond and Svensson (1977) equation (AS) and the values of the TRS-398 protocol (TRS398) are given.

Sontag (1980) and Johansson et al. (1977). Their values differ from the calculated ones here significantly. For instance at ^{60}Co TRS-398 uses the 0.987 ± 0.003 of Johansson et al. (1977), whereas the value calculated here is at 0.996 ± 0.001 . Hence, there is a nearly 1% deviation between currently used values and the ones calculated here. The replacement correction was also calculated for monoenergetic photon beams to exclude issues concerning the quality of the photon spectra. It is obvious, that the spectra are not the reason for the discrepancies.

The results given here follow a theoretical definition of the perturbation correction factor (see fig. 2.4). One can imagine that a measurement of this factor uncoupled from other effects is challenging. As discussed by Huq et al. (2001) the different approaches for the determination of the replacement correction factor yield a large spread in range of half a percent. Still, there is obviously a systematic deviation between the simulations here and the measurement based data currently accepted.

Since the calculated values for p_{repl} as presented above are close to unity, the alternative results for applying a constant shift in order to take the EPOM into account (see chapter 1.4.3) can be expected to be smaller as well. In figure 3.8(a) the calculated shifts for the cavity of a Farmer-type chamber are shown, based on different methods for determination. Obviously there is a discrepancy of $\sim 1-1.5$ mm between the applied shift recommended in the dosimetry protocols and the one calculated here. The result might be surprising, since Kawrakow (2006b) recently calculated the EPOM for Farmer-type chambers in the field of a 6 MV photon beam and, despite some influence of field-size and chamber construction, presented values at least close to $0.5 r_{cav}$. On the other hand, Kawrakow (2006b) included the whole depth-dose curve, while in the method used here only the local gradient at 10 cm depth (where chambers are placed in absolute dosimetry)

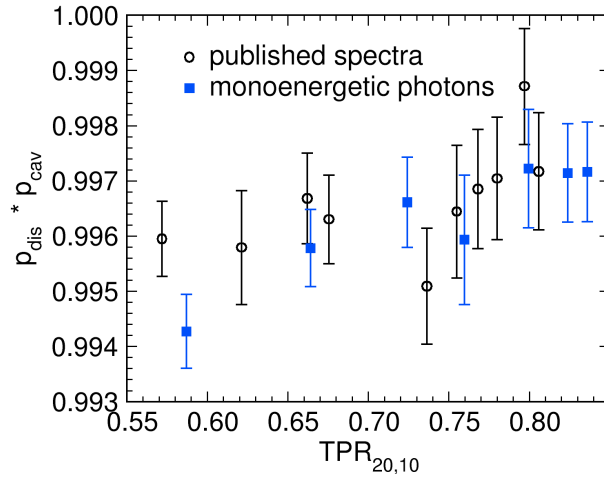


Figure 3.7.: The product of the p_{dis} and p_{cav} factors for the NE2571. The manner of calculating the value is shown in figure 2.4. Monoenergetic photons are used in a point source incident on the water phantom.

was taken into account.

Figure 3.8(b) shows two calculated depths dose curves. One is calculated for a small water volume yielding dose to a point, while the other one is calculated for the cavity of the Farmer chamber, water-filled with the density of air and without any shift. The difference and thus the shift of both is solely caused by the displacement of water due to the cavity's volume. Obviously, the deviation of both curves in terms of a shift is different in the build-up and depths beyond it (i.e. 10 cm). Normalizing the curves in figure 3.8(b) to their maximum would translate the needed shift in the build-up to the larger depths. The same applies for comparative measurements, which gave reason for the application of a $0.5 r_{\text{cav}}$ shift, recommended by e.g. DIN 6800-2. Usually *relative* depth-dose (or rather ionization) curves of thimble chambers are compared with those of plane-parallel chambers. If there is a depth dependent shift, as the results here allow an assumption for, it is covered when depth-dose curves are normalized. The EPOM is connected to the local gradient and the degree of CPD, maximal at regions prior to the build-up. Accordingly the χ^2 -minimizing will also depend on it. Hence, taking the whole curve into account for the minimization will still lead to minimizing mainly in the build-up region, where the ratio is strongly affected by the degree of CPD.

Recently Wang and Rogers (2009) investigated the reason for the difference in a similar manner confirming the assumption made above. They concluded that the normalization procedure is based on the wrong assumption, namely the same ionization within different detectors at the depth of maximum, which is wrong by the amount the results in TRS-398 and here differ.

In conclusion, both currently used methods for describing the replacement correction, i.e. applying a factor or applying a shift do not agree with the results presented here for *absolute* dosimetry purposes. On the other hand, in order to minimize the deviation of *relative* dose distributions normalized to their maximum, the recommended shift of $0.5 r_{\text{cav}}$ is appropriate, although as mentioned by Kawrakow (2006b) depends details of the

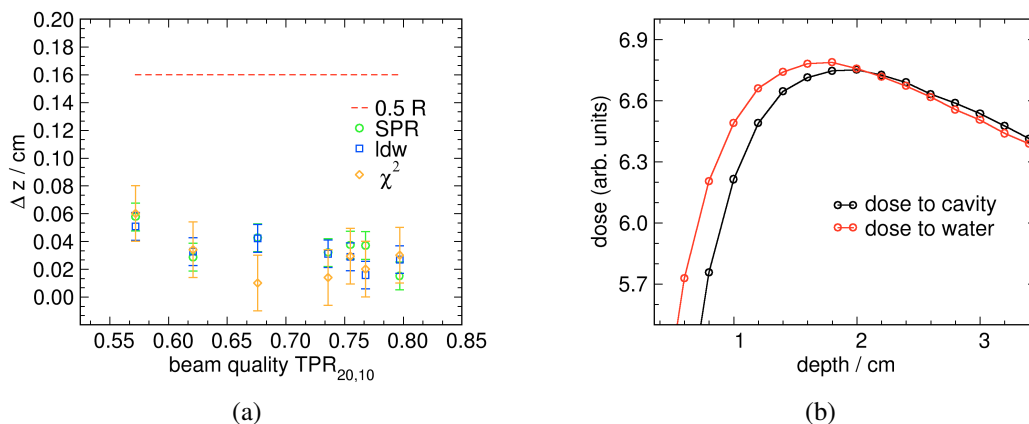


Figure 3.8.: Calculation of the effective point of measurement for the cavity of the NE2571. The broken line corresponds to the recommended shift of $0.5 r_{cav}$. The symbols are the results of the different methods, either based on the ratio between dose to water and to cavity applying stopping-power ratios and the local gradient (SPR), the low density water within the cavity (ldw) or the χ^2 minimization of the dose ratios (χ^2). For further description see chapter 2.2.2.2. (b) Build-up region for dose to water and dose to cavity of the cylindrical water-filled NE2571 ionization chamber with density of air.

chamber, field-size etc.

3.2.1.5. Calculation of the Energy Cut-Off Correction Factor p_{Δ}

In order to calculate the p_{Δ} factor one needs the relationship between the range of an electron and the kinetic energy, needed to travel the corresponding distance. The calculated relationship between the range and energy of mono-energetic electrons is shown in figure 3.9. The data for “CSDA” are based on the range calculations in the infinite medium without the creation of secondary particles. A perfect agreement between the CSDA ranges from the NIST database and the calculated ones can be found. The “true” range is calculated taking the discrete interactions (Bremsstrahlung, creation of δ -electrons) into account. The electrons energy needed to travel the true range is slightly higher and increases with range. This is due to the loss of energy in discrete interactions, which shortens the range.

The calculated mean chord length within the cavity of the Farmer chamber was 0.53-0.54 cm for all energies, close to the result of the simple approximation in eq. 2.7, which yields 0.56 cm. This corresponding cut-off energy Δ was calculated to be 16 keV, irrespective of beam quality. For the PTW31010 chamber, the calculated mean chord length was 0.37-0.38 cm, which results in $\Delta = 13$ keV. Table 3.3 summarizes the calculated perturbation p_{Δ} and beam quality dependent correction factors k_{Δ} for various beam qualities, based on the sprs with the appropriate cut-off energy Δ .

The calculated data demonstrate, that the proper choice of a cut-off energy shows only a weak influence for calculated correction factors. Although the cut-off energy is actually

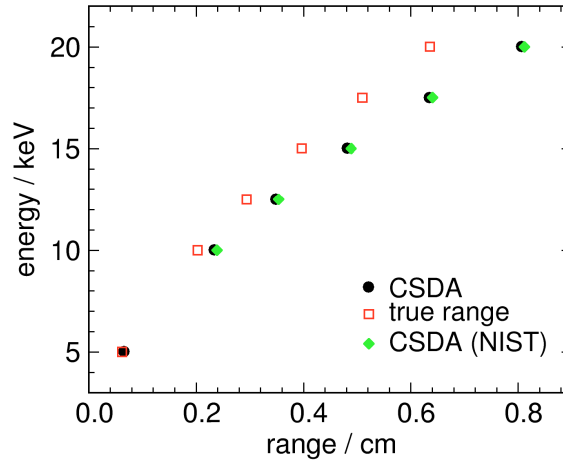


Figure 3.9.: Calculated relationship between range and energy of monoenergetic electrons in air. For the calculation of the “true range”, discrete interactions were included.

different from 10 keV, the resulting correction factors are small and the k_{Δ} normalized to the ^{60}Co -quality, does not exceed 0.05%. For any practical application, the factor seems to be of no importance. Taking the adherent uncertainty given in TRS-398 of 0.5% for current data of sprs between water and air into account, the influence is anyway included in the uncertainty budget for dosimetry based on standards of dose to water (Andreo et al., 2001). Hence, at least for air-filled ionization chambers of dimensions comparable to the ones used here, the inclusion of a p_{Δ} -factor should be negligible.

3.2.1.6. Overall Perturbation and Beam Quality Correction Factors

An overall perturbation correction factor p was calculated according to equation 1.11 with the use of calculated stopping-power ratios. This factor combines the influence of all constructive elements of an ionization chamber and thus all perturbation factors, e.g. p_{wall} , p_{cel} etc.. It is obvious from figure 3.10(a), that the overall perturbation of the ionization chamber decreases with increasing energy, which results in an increasing factor.

The values were calculated for the two different setups described in figure 1.7. Within the statistical uncertainties of about $\sim 0.1\%$ there is no difference between the SAD- and SSD-type setup.

The simulated cavity dose in the detailed model of the ionization chamber and the reference volume yields the beam quality correction factor k_Q as defined in equation 2.6 and circumvents any approximation when using single, possibly not independent factors. In figure 3.10(b) the resulting values for the NE2571 chamber and the used spectra are given as a function of beam quality for two mean ionization energies of graphite. A large set of measured data for the beam quality correction factor k_Q for the NE2571 chamber is available, compiled by Andreo (2000) with some necessary corrections. An polynomial fit through measured data is given in figure 3.10(b) as the solid line. These data can

Table 3.3.: Estimated factors p_{Δ} and k_{Δ} based on the calculated mean chord length given in *cm* within the cavity and the corresponding cut-off energy Δ given in keV. Calculations were performed for air cavities of typical ionization chambers placed in a water phantom according to required geometrical reference conditions (see tab. 1.1). The statistical uncertainty of all values does not exceed 0.03%.

beam descriptor	NE2571				PTW31010			
	length	Δ	p_{Δ}	k_{Δ}	length	Δ	p_{Δ}	k_{Δ}
^{60}Co Eldorado 6 ¹	0.54	16	0.9989	1.0000	0.37	13	0.9994	1.000
Varian Clinac 6 MV ²	0.53	16	0.9990	1.0001	0.37	13	0.9993	0.9999
Varian Clinac 10 MV ²	0.53	16	0.9990	1.0001	0.38	13	0.9992	0.9998
Varian Clinac 18 MV ²	0.53	16	0.9991	1.0002	0.38	13	0.9993	1.0000
Elekta SL25 25 MV ²	0.53	16	0.9993	1.0005	0.38	13	0.9995	1.0001

(1) (Rogers et al., 1988)

(2) (Sheikh-Bagheri and Rogers, 2002a)

Table 3.4.: Parameters of fits to calculated data of k_Q as a function of beam quality $\text{TPR}_{20,10}$ for a cubic polynomial of type $k_Q = a \cdot (\text{TPR}_{20,10})^3 + b \cdot (\text{TPR}_{20,10})^2 + c \cdot \text{TPR}_{20,10} + d$.

	parameter			
	a	b	c	d
experimental data	-0.8340	0.9780	-0.3134	1.0152
NE2571 ($I = 78 \text{ eV}$)	-1.3627	2.1014	-1.1135	1.2044
NE2571 ($I = 86.8 \text{ eV}$)	-0.6830	0.6311	-0.0422	0.9455

be understood as a mean value including chamber to chamber variations and allow a comparison with Monte Carlo calculated data. The Monte Carlo based data calculated here are shown for the two used mean ionization energies for graphite. Both sets differ by $\sim 0.5\%$ indicating the large influence of the electron cross sections on the calculated values. The best agreement with the fit to measured data would probably be achieved with some value in between. Rogers and Kawrakow (2003) considered the change of the I -value by only 3.5 eV instead of the 8.8 eV increase from 78 eV to 86.8 eV used here, which would yield obviously a good match.

Furthermore the data from the current dosimetry protocols TG-51 and TRS-389 are shown in the figure. Obviously, the data of the AAPM protocol give a slightly better agreement to the measurements, although no sleeve was included in the compilation of TG-51. The TRS-398 values with a 0.5 mm PMMA sleeve differ more from the measured values, but agree within their stated uncertainty.

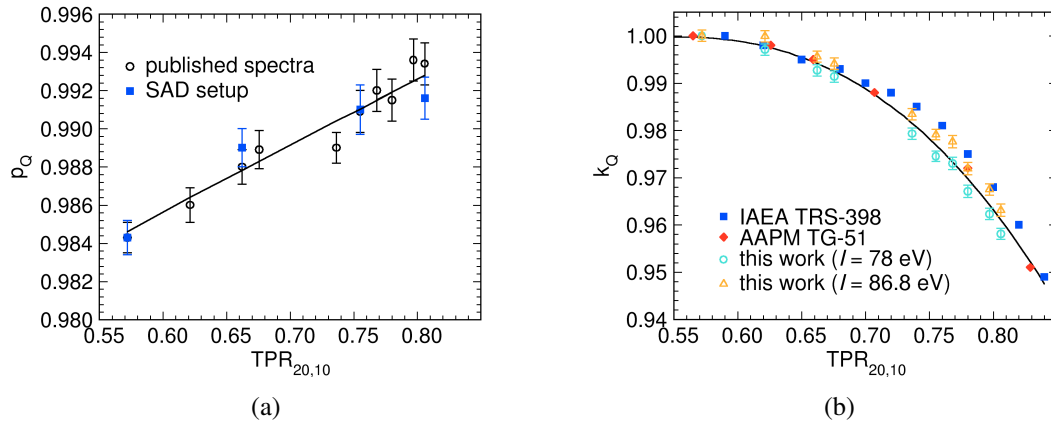


Figure 3.10.: (a): The overall perturbation correction factor p as a function of beam quality for the NE2571. Values were calculated for the published spectra in a SSD-setup and for some in a SAD-setup (see fig. 1.7). A linear fit of form $p_Q = 0.0349 \cdot \text{TPR}_{20,10} + 0.9647$ is shown. (b): Beam quality correction factor for the NE2571. The solid line represents a cubic polynomial fit through the compiled measurements given by Andreo (2000). The Monte Carlo calculated values of this study are calculated with two different mean ionization energies I of graphite. Parameters of the fits are given in table 3.4. The calculated values of the current dosimetry protocols TG-51 and TRS-398 are taken from these protocols. Fits to the Monte Carlo calculated data are omitted for better visibility, but are given in table 3.4.

3.2.2. Uncertainty-Estimation for Calculated Correction Factors

The above results for the beam quality correction factor k_Q point out, that the largest influence on the calculations is caused by uncertainties in the underlying cross sections. In the following the results for the calculation of the systematic uncertainties inherent to the calculated values will be given.

3.2.2.1. Fano Cavity Test

The Fano cavity test was applied to the chamber model of the NE2571 and the ratio between calculated cavity dose under Fano-conditions (see chapter 1.5.5.2) and the expected value, i.e. $E(\mu_{en}/\rho)_{wall}$, was 1.0002 ± 0.0007 . Hence, the transport algorithms as well as the geometry related functions for the modeling of the NE2571 chamber can be considered as accurate.

3.2.2.2. Different Transport Options, Setup and Cross Sections Variations

In figure 3.11(a) the deviation of k_Q for different transport parameter settings is shown. Within the statistical uncertainties of $\sim 0.1\%$ (coverage factor $k = 1$) no influence due to the lowered electron transport cut-off energy (ECUT512), i.e. 512 keV can be observed.

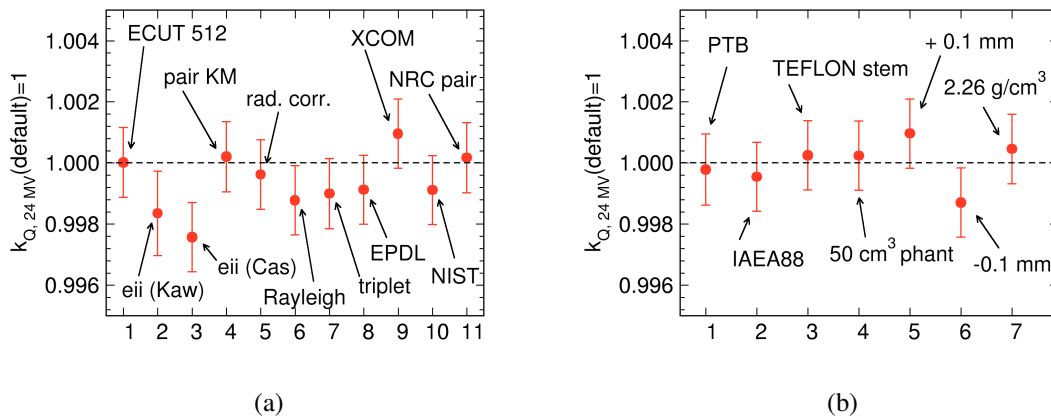


Figure 3.11.: Influence of transport parameter settings (a) and the simulation setup (b) on the calculated beam quality correction factors k_Q . The default settings correspond to unity. For explanation see text.

The same applied for increase of cut-off energy up to 526 keV, and 15 keV for photons as well (results not shown), except for the decreased simulation times with higher cut-offs.

EGSnrc allows the explicit simulation of electron impact ionization (eii) using different cross section datasets (Kawrakow or Casnati). Eii results of electron interactions with the inner atom shells, with following emission of characteristic X-rays and Auger-electrons. Although the process of electron impact ionization is considered to be of higher importance for low energy applications, such as exact calculations of X-ray spectra, the inclusion of eii leads to a small, but significant decrease of $\sim 0.2\%$ in calculated k_Q , irrespective of the database used.

In the simulation of pair production processes, the sampling of the angle for created positron/electron pairs can be changed to the more exact distribution (pair KM). Within the statistical uncertainties, no change can be observed. Likewise, the inclusion of radiative corrections to the simulation of Compton scattering (rad.corr) such as double-Compton scattering has no significant influence on calculated k_Q values. Rayleigh scattering is usually not included in high-energy simulations due to its low contribution to the total photon cross sections, i.e. the attenuation coefficient. A small, nearly insignificant influence of explicit simulation of Rayleigh scattering processes is observable in figure 3.11(a) (Rayleigh). Triplet production (triplet) processes are included in the total photon cross sections, but usually not modeled explicitly. In the recent EGSnrc version, the triplet interactions can be modeled, but have no influence on the k_Q value.

EGSnrc uses the total photon cross sections from Storm& Israel by default (Kawrakow and Rogers, 2006). The current XCOM and EPDL-97 tabulations are more considered to be more accurate, but the influence on the calculated k_Q values is insignificant. Similarly, the changed cross sections for sampling of photons energy in Bremsstrahlungs events from NIST-databases (NIST) do not change the result. Neither do the more exact NRC pair cross sections (NRC pair) for the sampling of the pair energies, instead of the default cross sections by Bethe-Heitler.

The beam quality correction factor k_Q was calculated with ^{60}Co spectra of Mora (see

tab. 3.2) as default. The discrete spectrum of the Co-decay is altered by different housings of the source and collimator of a Cobalt-machine. Two other Co-spectra were used for the calculation of k_Q (see fig. 3.11(b)). They both result in an indistinguishable result. In the same manner, did the increased size of the water phantom 50 cm^3 not lead to significant changes. Changing the material of the stem does not alter the result, which is not surprising keeping the magnitude of the stem-correction itself in mind (see fig. 3.5). The changed wall thickness of $\pm 0.1\text{ mm}$, which corresponds to a $\sim 26\%$ change in thickness, leads to a small but systematic change. Even changing the density from 1.7 g/cm^3 to 2.25 g/cm^3 with the correspondingly changed density effect parameters does not have an influence.

In conclusion, the above investigations point out, that the calculation of k_Q factors with the EGSnrc system are mostly stable within the statistical uncertainties of $\sim 0.1\%$ (at $1\sigma = 68\%$ confidence), when changing from default transport-parameter selection to more “exact” settings. Only the electron impact ionization significantly changes the result by $\sim 0.2\%$. Even severe changes in the dimensions of the wall lead to comparatively small changes. One must keep in mind, that the manufacturing accuracy is generally better than the 0.1 mm used here as a variation. On the other hand it was shown in figure 3.11(b) that the influence of the graphite part of the ionization chamber wall is small. A variation in k_Q is therefore not likely to occur, when changing the dimensions of it.

In the DIN 6800-2 it is stated that the inclusion of small uncertainties below 0.1% generally has no significant influence on the uncertainty in measuring dose to water (DIN6800-2, 2008). Following this statement, the influence of the transport parameter settings is almost negligible. The investigations presented here are limited to simplified, collimated point sources with realistic spectra. On the other hand, the used spectra are as realistic as one can characterize a source by a simple quality index (such as $\text{TPR}_{20,10}$) as done in the dosimetry protocols.

3.2.2.3. Varying Cross Sections

Although the changed databases for photon cross sections did not lead to a significant change in k_Q (see fig. 3.11(b)) they are mostly based on similar theories. Table 3.5 summarizes the results for the estimation of uncertainties in k_Q due to uncertainties in the cross sections of the different materials and the corresponding sensitivity. The largest fraction of the total uncertainty ($\sim 0.87\%$) is caused by uncertainties in photon cross sections, dominated by the contribution due to Compton-scattering. Due to the small magnitude of the influence, no single sensitivities for the materials are shown for photo-effect and pair production, rather the combined sensitivity summed in quadrature is shown. The largest influence is caused by water, forming the largest parts of the simulation geometry. It is stated that cross sections in current tabulations are accurate within 1-2% but no clear value is given for single materials (Hubbell, 2006). Further, the main influence has been demonstrated to be caused by the Compton-effect, where a modeling used for tabulations (such as XCOM) might be better than 1%. Furthermore, one needs to keep in mind that the uncertainties for the single materials might be correlated, i.e. cross sections differ from the true value by the same amount for all materials and energies. Equation 2.10 considers single uncorrelated contributions and the values used here can be considered

Table 3.5.: Calculated sensitivity and final uncertainty in calculated k_Q factors at $\text{TPR}_{20,10}=0.806$ (24 MV) due to variations in the photon and electron cross sections.

Parameter variation		medium	Sensitivity	Related standard uncertainty	
x_i			$\frac{\partial(\Delta k_Q/k_Q)}{\partial x_i}$	$u(x_i)/x_i$ /%	$ \Delta k_Q/k_Q $ /%
Percentage variation Photon cross sections ^a	Photo effect	all	0.045	± 2	0.09
		H2O	0.711	± 1	0.71
	Compton scattering	C	0.413	± 1	0.41
		PMMA	0.260	± 1	0.26
		Al	0.003	± 1	≤ 0.001
Variation in mean excitation energy ^b	Pair production	all	0.056	± 2	0.11
		H2O	0.089	± 2.7	0.24
		C	0.067	± 6.1	0.41
		PMMA	0.032	± 1.4	0.04
		Al	0.003	± 0.8	0.003
	Air	0.024	± 1.3	0.03	
				Total	1.00

(a) assumed Gaussian distribution

(b) 68% confidence of ICRU37 values

as a conservative estimation. Due to the fact that the numerical methods for determining the cross sections are identical for the single materials (e.g. free electron approximation based on Klein-Nishina), it is likely that a correlation between all materials exists. So when the Compton cross sections for water are increased the ones for PMMA must be increased as well. Changing the photon cross sections for photoelectric effect, Compton effect and pair production for all materials simultaneously and summing them in quadrature, reduces the contribution to the overall uncertainty from ($\sim 0.87\%$) to ($\sim 0.03\%$). Hence, the values in tab. 3.5 can be understood as a conservative estimation.

The uncertainties of mean ionization energies in stopping powers ($\sim 0.48\%$ of total uncertainties in tab. 3.5) are dominated by the I -value of graphite which possesses the largest uncertainty. The large influence was already discussed in chapter 3.2.1.6. In the context of heavy ion radiotherapy the exact knowledge of the I -value for water is essential for an exact calculation of ranges in a patient. Thus, there has been recently discussions and higher values (Paul, 2007) based on experimental data were recommended, exceeding the given uncertainty of ICRU37. Accordingly I -value for water varying between 67.2 eV up to 80.8 eV point out, that these might still be too optimistic (Henkner and Jäkel, 2007). Electron cross section uncertainties in this study are limited to the major contribution of uncertainty in mean excitation energy I . Hence, the overall uncertainty might be higher and influenced by the uncertainty of Bremsstrahlung cross sections. Recently, Faddegon et al. (2008) compared Bremsstrahlungs-production at thick targets and observed agreement to simulations with the EGSnrc system within 10%. Though, due to comparatively low atomic numbers the importance of Bremsstrahlung is less severe for the investigated simulations in the present study. The changed cross

section databases for Bremsstrahlungs-production at least did not have an influence (see fig. 3.11(a)).

3.2.3. Summary

The above results demonstrate that the calculation of beam quality correction factors k_Q is feasible with the use of Monte Carlo simulations. The application of the developed variance reduction techniques allows for the simulation of the single, underlying perturbation correction factors. Those show deviations from the currently used ones by up to 1%. The theoretically justified factor p_{Δ} turned out to be rather small. Calculated beam quality correction factors show agreement with the ones used in current dosimetry protocols and available data based on measurements, but due to variations in the available data and stated uncertainties in the dosimetry protocols of 1% no definite “ground truth” is known. More importantly the Monte Carlo simulated values suffer from the uncertainties of the underlying cross sections, leading to a systematic uncertainty. As a conservative estimation these uncertainties can be expected to be up to 1% for calculated k_Q -values.

3.3. Non-Reference Conditions

For the investigation of ionization chambers under non-reference conditions, the linear accelerator head model of the Siemens KD 6 MV beam was matched to corresponding measurements. In the following the results of this commissioning procedure will be presented. Using the model, ionization chamber perturbation correction factors and the k_{NR} factor were calculated. The largest perturbations are expected to occur at points with charged particle dis-equilibrium. For the investigation of these conditions ionization chambers and other detectors were compared in the boundary of an idealized photon field, considering their ability to measure a relative dose profile with high gradients with small perturbations.

3.3.1. Modeling the Siemens KD Linear Accelerator

Figure 3.12 shows the relative calculated and measured profiles in the depth of the dose maximum (1.7 cm) inside the water phantom in the 40 cm x 40 cm field normalized to the central axis. These calculations included the ionization chamber and were performed for changed parameters of the primary electron beam hitting the target of the linear accelerator and for changed densities of the flattening filter respectively. The off-axis factor, i.e. the relative dose normalized to the central axis, decreases linearly with increased energy of the primary electrons, the horns in the cross-profile are lowered. Likewise, there is a decrease of the off-axis factor for increased spot sizes as well, although following rather a quadratic trend. Contrary, an angular spread of primary electrons leads to an increased off-axis factor, increasing the horns of the profiles. In most studies an angular spread is not included for modeling of linear accelerators. Recently Sawkey and Faddegon (2009) stated an upper limit in beam divergence of 0.2° for a Siemens linac at 6 MV. In the following commissioning no change of the angular spread was therefore considered, but the

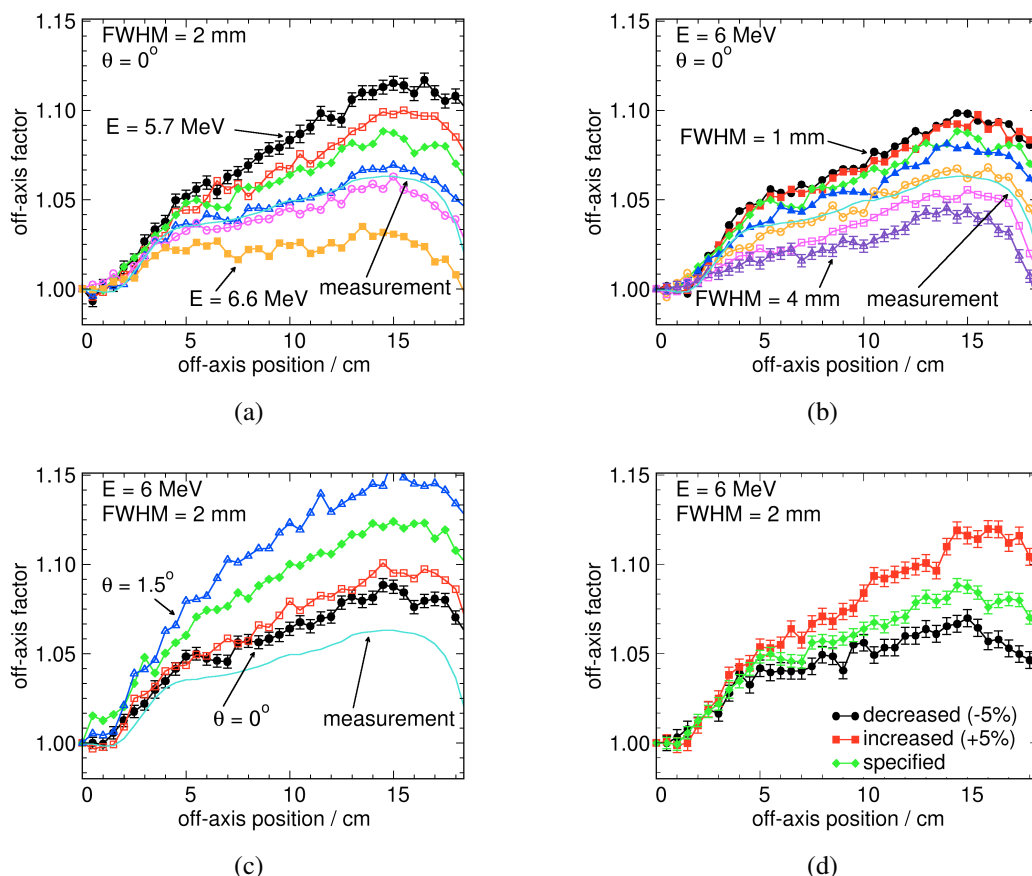


Figure 3.12.: Variation in the 40 cm x 40 cm cross-profile in 1.7 cm depth due to variations in mean energy of the primary electron spot (a), its size (b) or mean angular spread (c). The change of the profile due to variations in the flattening filters density is shown in (d).

principle influence is illustrated in figure 3.12(c).

The variation in the flattening filters density leads to changed off-axis profiles (see fig. 3.12(d)), indistinguishable from a change in the primary electron parameters. The density of the flattening filter must therefore be known as precisely as possible. The manufacturer provided detailed information about the composition of the used materials within the Siemens KD accelerator including the flattening filter. It turned out however, that the specified density of the steel used in the flattening filter did not allow a match of PDDs and cross profiles with the methods described in the following. A comparison to DIN-EN standards of steel (DIN-EN-10088-1, 2005) revealed a discrepancy of $\sim 3.7\%$ in the density for this specific type (SST303), which corresponds to a decrease of $\sim 0.3 \text{ g/cm}^3$ from the specified “approximately” $\rho = 8.2 \text{ g/cm}^3$. As stated by Sheikh-Bagheri and Rogers (2002b) in order to match off-axis factors accurately, the density needs to be known better than 0.1 g/cm^3 , which can be confirmed taking a look at the strong influence in figure 3.12(d). On the other hand, the density of the used steel type was given by Faddegon et al. (1999) to have a density of $\rho = 8.06 \text{ g/cm}^3$, stated to be

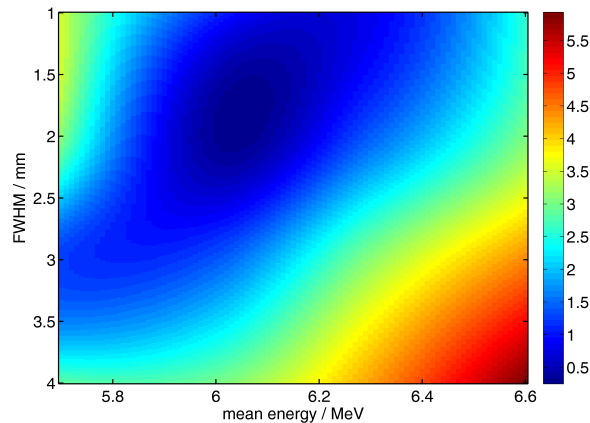


Figure 3.13.: Difference between calculated and measured off-axis profiles for different energy and spot size combinations in the simulations. In between the 16 discrete positions a cubic spline interpolation was applied.

based on Siemens specifications as well. Given the variations in manufacturer specifications, it was decided to use the value of $\rho = 7.9 \text{ g/cm}^3$ according to DIN-EN standard.

Some Siemens KD linacs are equipped with a target replacement kit (Faddegon et al., 2004), where the target material is changed from Gold to Tungsten. However, the changed target did not lead to an observable change in the profiles, at least not for this energy and the depth of 1.7 cm. Actually, as discussed by Faddegon et al. (2004) one goal during the development of the target replacement kit was to allow the use of the new target without the need for a re-commissioning of the linac. Using different spreads of the primary electron spectrum lead to indistinguishable off-axis profiles, comparable to the results of Sheikh-Bagheri and Rogers (2002b), Tzedakis et al. (2004) or Smedt et al. (2005). Sheikh-Bagheri and Rogers (2002b) reported on the large influence of the primary collimator opening even by changes of $\pm 0.1 \text{ mm}$. Within 0.5% statistical uncertainty such an influence could not be observed. Changing the position of the flattening-filter by $\pm 2 \text{ mm}$ neither lead to a significant influence. The exit window was not included in the simulations. Neglecting the exit window as an extra source of Bremsstrahlung and the resulting angular spread of electrons, the influence of the exit window can be compensated by an adjusted energy of the electrons, since its main influence is a decrease of the primary electrons energy. This might explain the difference of the lower energy needed for agreement here ($\sim 6 \text{ MeV}$) compared to higher energies as suggested by e.g. Sheikh-Bagheri and Rogers (2002b).

In figure 3.13 the calculated relative root mean squared deviation (RMSD) between the measured and the 16 calculated profiles, each with 36 simulated chamber positions (0-18 cm distance from central axis), is depicted. In between the 16 points, a cubic spline interpolation is applied. The chamber positions included in the calculation of the RMSD were limited to 18 cm maximum distance from the central axis to avoid any influence of possibly misplaced jaws or inaccurate modeling within the simulation. A good match is obviously achieved at roughly 6 MeV and 2 mm spot size. Using the interpolated values in figure 3.13 the minimum difference in terms of RMSD is found at an energy of

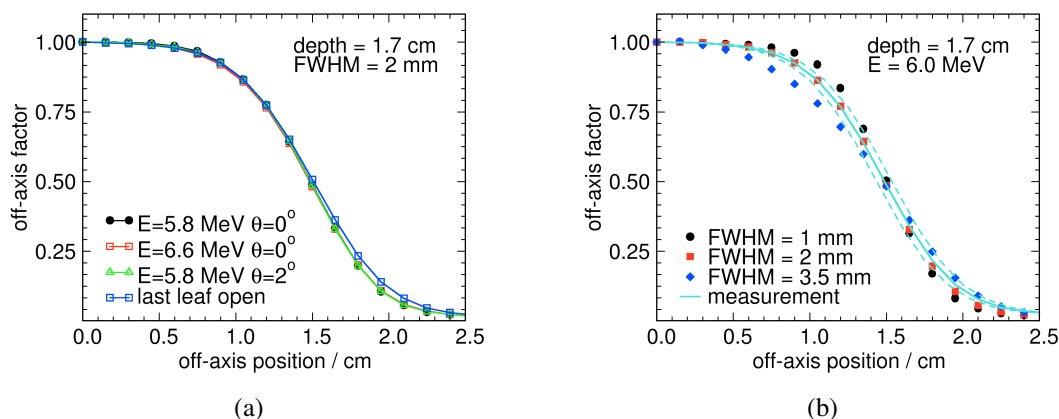


Figure 3.14.: Relative dose distribution within the 3 cm x 3 cm field. (a): For variations in angular spread and mean energy, indistinguishable results are achieved. Although the field is blocked by jaws and MLC, leaving one leaf open leads to an observable influence. (b): Variations in the spot size lead to different penumbra width. The comparison to the measurement can be used to obtain the best match. A hypothetical uncertainty of ± 1 mm in the position of the detector during measurements is indicated by the broken lines.

6.05 MeV and 1.85 mm spot size.

The spot size of the primary electron beam was further adjusted taking small fields into account. The simulated 3 cm x 3 cm field in 1.7 cm depth turned out to be independent of energy of primary electrons as well as of the mean angular spread even for large values (see fig. 3.14). The profiles were simulated in the inplane direction with the field boundary completely covered by the jaws and the MLC. Figure 3.14(a) shows the non-distinguishable influence of the changed primary energy on calculated profiles. However, leaving the last leaf pair open and thus defining the field boundary by the jaws only, changes the slope of the dose distribution in the penumbra in the portions most distant.

The profile only depends on the primary electron spot diameter as illustrated in figure 3.14(b). As can be concluded from this figure, a diameter of 2 mm leads to a good agreement to the measurements. Taking profiles of varying spot diameter and calculating the penumbra-width between 80% and 20% of the dose-distribution leads to a linear relationship. For the 2 mm spot size a penumbra width of 0.64 mm resulted while the measured profile shows a penumbra width between 80% and 20% of 0.66 mm. Taking a positioning uncertainty during measurement of 1 mm into account (see broken lines in figure 3.14), the estimated spot size of 2 mm seems to be reasonable and in agreement to the calculated minimal difference in large profiles (see fig. 3.13).

Simulated fields of 3 cm x 3 cm were used to calculate depth-dose curves for varying mean energy. The best agreement in terms of mean difference and a χ -square test passed at a $p=0.95$ level could be achieved with an energy of 6.0 MV as summarized in table 3.6. For field sizes of 10 cm x 10 cm and 40 cm x 40 cm a good agreement was achieved likewise.

Table 3.6.: Differences of calculated and measured depth-dose curves in terms of root mean square deviation in % and χ^2 test with $N = 19$ degrees of freedom, i.e. based on the 20 calculated dose values along the depth.

mean energy	3 cm x 3 cm		10 cm x 10 cm		40 cm x 40 cm	
	χ^2	RMSD	χ^2	RMSD	χ^2	RMSD
5.95	1.413	0.476	-	-	-	-
6.00	0.088	0.436	0.453	0.224	1.512	0.407
6.05	3.341	0.590	-	-	-	-
6.10	4.353	0.730	-	-	-	-

3.3.1.1. Efficient Use of the Accelerator Model

For the optimization of the DBS algorithm in terms of efficiency the splitting numbers were varied from 7750 for a 3 cm x 3 cm field to 1450 for a 40 cm x 40 cm field. Usually one achieves a good efficiency with a general splitting number of 1000 as suggested by Kawrakow et al. (2004), but due to the many calculations necessary it seemed worthwhile to optimize the splitting number. Still, the gained improvement was moderate and only in the order of $\sim 20\%$ for the smallest field.

As mentioned in chapter 2.3.1, particles leaving the accelerator model and entering the simulation geometry of the ionization chamber in the water phantom, were splitted. This allowed for a slight increase in efficiency since most of the simulation time is spent on the linac part and thus splitting (i.e. reusing) particles increases the probability of a ionization chamber dose contribution. For the 3 cm x 3 cm field particles were split 16 times, 8 times for the 10 cm x 10 cm field and 4 times in the 40 cm x 40 cm field at the bottom of the accelerator head.

3.3.1.2. Validation and Limitations of the Model

Figure 3.15 shows simulated dose profiles for the three field sizes in depth of 1.7, 5, 10 and 20 cm in comparison to the measured profiles. Further a comparison in the build-up region is shown. There is a good agreement for most of the calculated doses within 1 mm/1%. Larger deviations occur for some points of the 40 cm x 40 cm field at points within the penumbra, presumably due to problems in modeling the jaws/MLC for these large field sizes. Deviations are also observable for dose out of the field (see fig. 3.15(c)). In the simulations a dose of almost a factor two lower compared to the measurements is calculated. Due to the idealized modeling of the MLC, no tongue and groove structures are simulated and one might expect the lower dose in the simulations caused by the missing transmission through the leaves. Opening the last leafs in the profiles (see fig. 3.14(a)) leads to a slightly higher out of field dose, but still does not allow for an agreement. On the other hand, Huq et al. (2002) compared various types of MLCs and measured a leakage of only $\sim 1\%$, which is in better agreement to the calculations here than the measurements.

The comparison of Monte Carlo calculated and measured dose distributions in the build-up region of photon beams and the discrepancies have been discussed in litera-

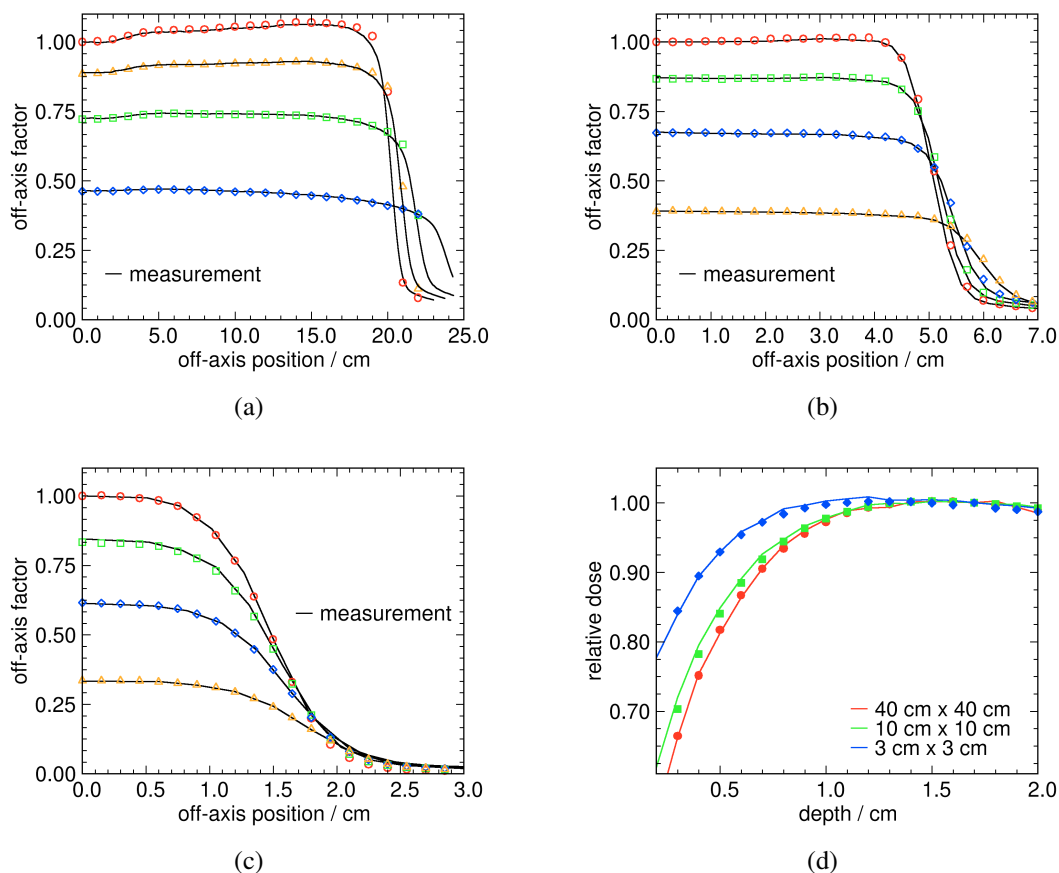


Figure 3.15.: Calculated and measured dose distribution of the 6 MV photon beam of the Siemens KD at depths of 1.7, 5, 10 and 20 cm. A comparison of the half-profiles is shown for field sizes of 40 cm x 40 cm (c), 10 cm x 10 cm (b) and 3 cm x 3 cm (c). The figure (d) shows the comparison of the build-up region for various field sizes.

ture. Kawrakow (2000b) attributed these discrepancies to the incorrect handling of a replacement correction due to the presence of the ionization chamber air cavity. In the calculations shown in figure 3.15(d) the ionization chamber was included and thus agree better than 1%/1 mm. Generally, an agreement of measured and simulated dose within 0.2 mm could be achieved for all field sizes.

Table 3.7 gives the results of calculated output-factors as the ratio of the ionization chamber reading for various field sizes normalized to the reading at the 10 cm x 10 cm field. There is a good agreement $\leq 0.6\%$. As described in chapter 2.3.1.3 the monitor chamber backscatter was calculated for the various field sizes. No influence due to monitor chamber backscatter for field sizes ranging from 1 cm² up to 40 cm² within 0.05% statistical uncertainty could be found. Hence, the measured values in table 3.7 do not need to be corrected and can directly compared to the simulated. Obviously the monitor chamber construction avoids a response to backscattered particles.

The agreement of the measured and simulated dose can be considered as accurate,

Table 3.7.: Comparison of calculated and measured output-factors. The statistical uncertainty on last digit for the simulation is shown in the parenthesis.

square field size <i>cm</i>	measurement	simulation	deviation %
3	0.828	0.833(2)	0.6
40	1.176	1.170(3)	0.5

taking the generally requested accuracy in radiotherapy into account (IAEA, 2004). Scott et al. (2008) even considered a 30% deviation outside the field as reasonable.

The mentioned uncertainties in cross sections (see chapter 3.2.2) apply for the simulation of linear accelerator as well. In a recent study, Faddegon et al. (2008) compared various Monte Carlo codes to simulate measurements of Bremsstrahlung from thick targets for 10-30 MV beams. They concluded that the fluence distributions within typical angles for radiation treatment (out to 10°) can be calculated within their measurement uncertainty of 3%. As stated in their conclusion some error in the angular distribution might be compensated by the selection of primary electron parameters. Using the EGSnrc Monte Carlo code, photon spectra below 2-3 MeV were overestimated by 15%. These results were similar or even larger for the PENELOPE and GEANT4 codes. It is difficult to translate these systematic deviations into a deviation in absorbed dose within the ionization chamber, but any matching of simulations to measurement as done here will suffer to some degree from these problems. Still, the match achieved here can be considered as good enough for the investigations of ionization chambers inside the field of the linear accelerator as described in the following.

3.3.2. Ionization Chambers in the 6 MV Field of a Linear Accelerator

3.3.2.1. Depth-Dose Curves and Profiles

In figure 3.16(a) the mean energy of photons of the linac model and created secondary charged particles within the water phantom is shown, excluding regions of charged particle disequilibrium such as build-up and penumbra regions. The mean energy of photons varies as a function of depth, differentially for the single field sizes. While a beam-hardening occurs in small fields, which is caused by the larger attenuation of low energy portions in the linear accelerator spectrum, a decrease can be observed for the large field size due to the increased contribution of low energy scattered photons. However, the change by $\sim +25\%$ for the 3 cm x 3 cm field and by $\sim -35\%$ in the 40 cm x 40 cm causes only a comparatively small change in the mean energy of the secondary electrons.

Figure 3.16(b) shows the change of mean energy as a function of off-axis distance in the 40 cm x 40 cm field. For the shallow depth of 1.7 cm a decrease of mean photon energy by $\sim -10\%$ is observable, which is caused by the differential hardening of primary photon within the flattening filter. Similarly the mean energy of electrons drops. With increasing depth, this trend is reversed and towards the larger off-axis distances an increase of mean energy by $\sim +16\%$ is caused by the lack of lateral low energy scatter.

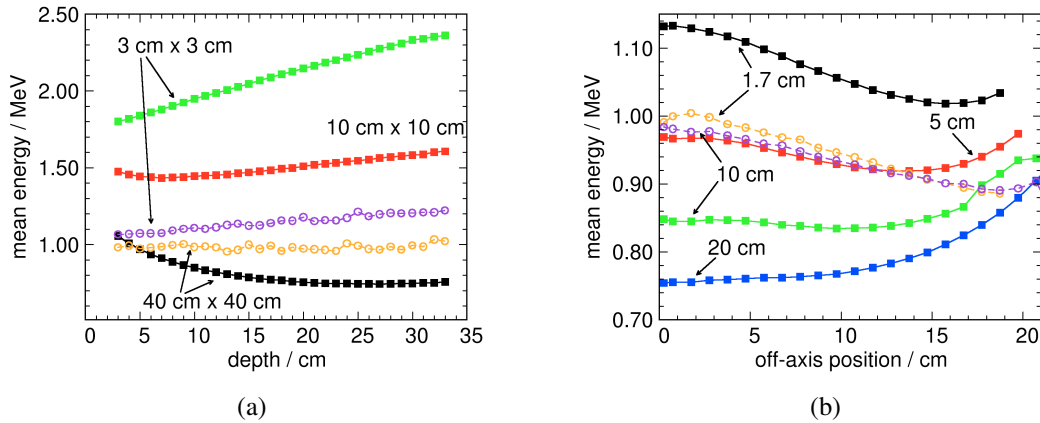


Figure 3.16.: Changed mean energy of photons (filled symbols) and charged particles (open symbols) within the 6 MV field of the Siemens KD. In (a) the function of depth for three field sizes is given, in (b) the function of distance to the central axis at various depth within the 40 cm x 40 cm field. Note the different scaling of the energy axis.

The above observations allow for the expectation of a changed response of ionization chambers within the field of the linear accelerator and justifies the introduction of the k_{NR} factor.

In figure 3.17(a) the calculated k_{NR} factors for the PTW31010 are shown as a function of depth for three field-sizes and as a function of off-axis distance in the 40 cm x 40 cm field in two depths. The resulting total correction factor k_{NR} for the 3 cm x 3 cm field in figure 3.17(a) changes by $\sim -0.5\%$ and does not exceed unity by more than 0.005 ± 0.0025 . For the other two field sizes no significant change is observable. Still, k_{NR} in total is slightly smaller than unity for the 40 cm x 40 cm field. Likewise, for the function of off-axis distance, the factor k_{NR} is close to but less than unity and changes nearly insignificantly.

In figure 3.18(a) and 3.18(b) the individual perturbation correction factors and the stopping-power ratios are shown as a function of depth for two field sizes. The single values are normalized to the value at reference condition, i.e. 10 cm depth in the 10 cm x 10 cm field. The decreasing stopping-power ratio between water and air in the 3 cm x 3 cm field is the result of the increased mean energy of the particles due to the beam hardening pronounced in the smaller field size. Irrespective of this spectral change, the wall and central electrode correction factors stay nearly constant as a function of depth, both differing from their values in the reference field by only $\sim 0.1\text{-}0.2\%$. The relative p_{repl} factor is slightly larger than unity for shallow depths and decreases with increasing depth, but almost insignificantly within the statistical uncertainties of $\sim 0.2\text{-}0.3\%$.

The sprs are minimally increased in the 40 cm x 40 cm field compared to the value in the reference field, the resulting relative value in figure 3.18(b) is slightly increased but stays almost constant. The p_{wall} perturbation is larger than in the reference field, the p_{cel} perturbation is smaller respectively. Both factors change by $\sim 1\%$ with depth. While the

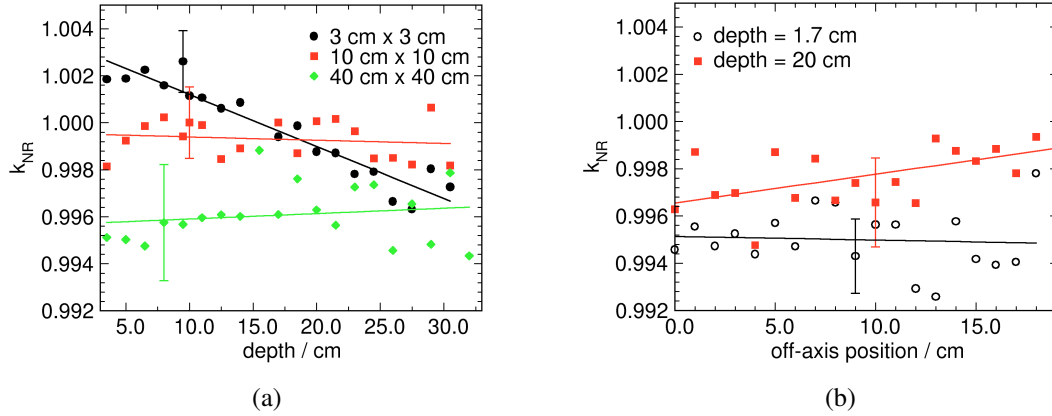


Figure 3.17.: Total correction k_{NR} in the field of the Siemens KD2 6 MV-X photon beam as a function of depth (a) for three field sizes and as a function of the off-axis distance for two depths (b). The error-bars indicate the statistical uncertainty of $\sim 0.15\text{-}0.3\%$ and are shown at single values only for better visibility. The straight lines represent linear-regression fits to the values.

relative p_{wall} factor increases since the low energy particles are absorbed partially in the chamber wall, the low energy, scattered photons interact in the central electrode made of aluminum and create secondary electrons, causing a decrease of the p_{cel} factor in turn. Hence, due to the opposite variation of both factors k_{NR} as a function of depth does not change within $\pm 0.2\text{-}0.3\%$ statistics.

Figure 3.18(c) shows the relative perturbation correction factors and the sprs as a function of distance from the central axis. In the depth of maximum (1.7 cm) the wall perturbation correctionization changes marginally by $\sim -0.1\%$. This is in contrast to the findings of Dohm et al. (2005), who measured and calculated a $\sim 2.5\%$ change in response of the same chamber type in a Elekta 6 MV beam at the depth of dose-maximum. This discrepancy might be attributed to the type of accelerator used in the study of Dohm et al. (2005), or more likely caused by a change of response of TLD detectors which they used for comparison. Further, their calculated values for the p_{wall} perturbation correction factor, which they addressed the changed response to, were based on the Almond-Svensson formulation, which has been shown to be inaccurate (see chapter 3.2.1.3).

The above results point out, that the concept for a correction factor k_{NR} is theoretically justified, but the resulting corrections are small for primary photon beams. Due to the subtle construction of commonly used ionization chambers, the influence due to chamber dependent perturbation correction factors p_{wall} and p_{cel} compensates each other to a large degree at large fields, where a large fraction of low energy scattered photons is present. The flat response of the ionization chambers to low energy kilovoltage photon beams due to the construction and proper selection of central electrodes dimensions has been discussed by Ubrich et al. (2008). The change of sprs turn out to be the main reason for changes in k_{NR} from unity of $\sim 0.5\%$ as a function of depth in small fields. For the large fields the combination of all other perturbation factors affect the slope of k_{NR} .

The remaining statistical uncertainties e.g. in figure 3.17 are high compared to the

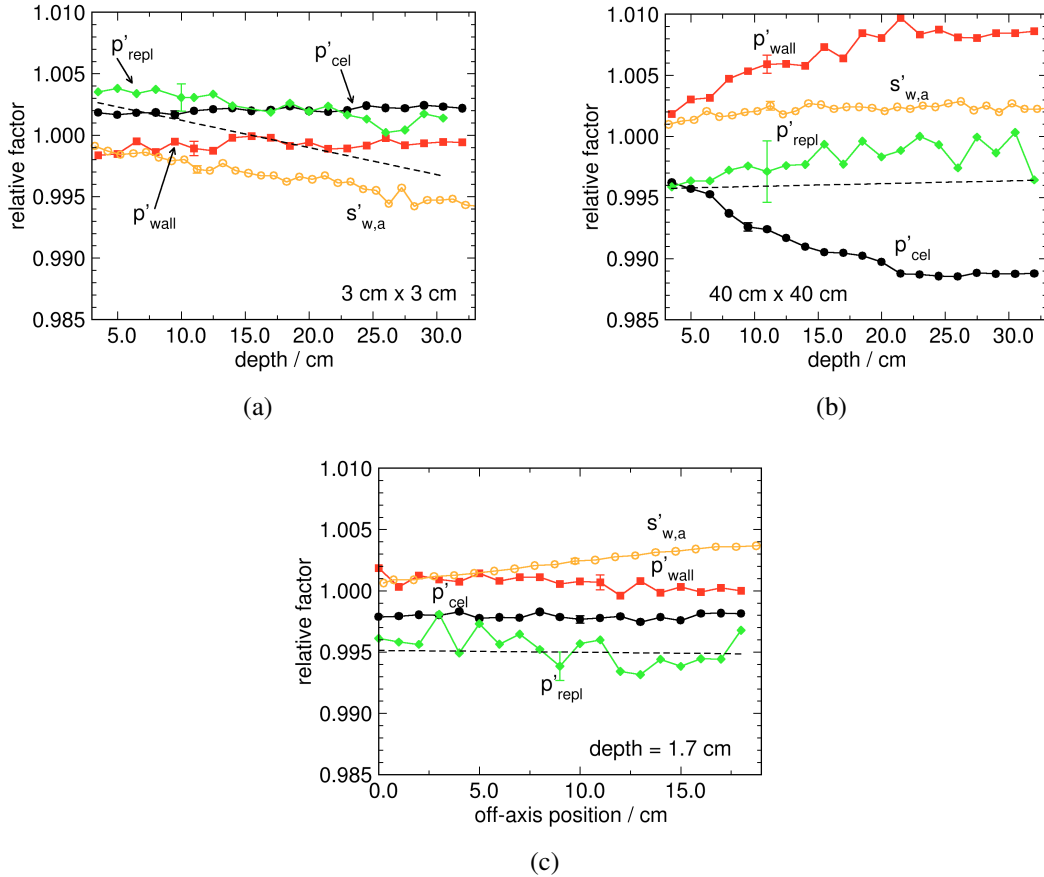


Figure 3.18.: Calculated relative perturbation correction factors and stopping-power ratios between water and air as a function of depth for a 3 cm x 3 cm (a) and a 40 cm x 40 cm field (b). In (c) the individual factors are shown as a function of the off-axis distance in 1.7 cm depth in the 40 cm x 40 cm field. All values are normalized to the 10 cm x 10 cm field at 10 cm depth on the central axis. The broken lines are the linear fits of fig. 3.17. The error-bars indicate the statistical uncertainty and are shown at single values only for better visibility.

overall magnitude of k_{NR} . Therefore the k_{NR} values were recalculated as a function of depth with a slightly enlarged reference volume and with a collimated point source with a published 6 MV spectrum of the Siemens KD (Sheikh-Bagheri and Rogers, 2002a). This simulation setup allowed for smaller statistical uncertainties of $\leq 0.1\%$. The calculated values using the complete treatment head simulation agreed within their statistical uncertainty with these values. Linear regressions as shown in figure 3.17(a) revealed similarly a maximum change for k_{NR} from unity of $\sim 0.5\%$ at highest.

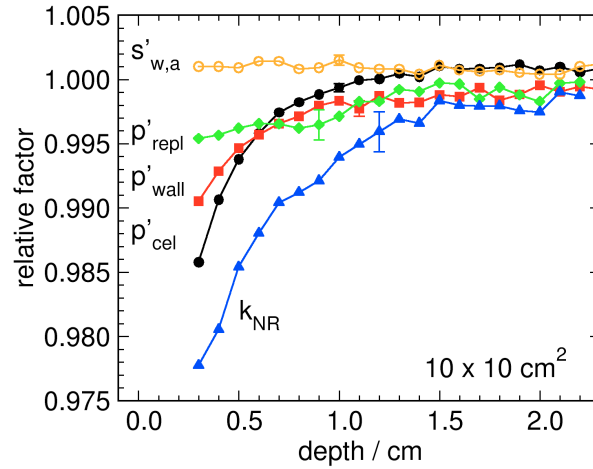


Figure 3.19.: Individual perturbation correction factors, stopping-power ratios and the total correction k_{NR} within the build-up region of the 6 MV-X photon beam. All values are normalized to the 10 cm x 10 cm field at 10 cm depth. Error-bars indicate the statistical uncertainty of the MC calculated values and are shown at single values only for better visibility.

3.3.2.2. Build-up Region and the Effective Point of Measurement for the PTW31010

As shown in figure 3.19, depth dependent perturbations exist which vary by up to $\sim 1.5\%$ (p_{cel}) in the build-up region. The total correction k_{NR} arises from the individual perturbation correction factors which are not constant in the build-up region.

The depth dependent change in k_{NR} can be interpreted as a wrong positioning of the ionization chamber. A χ^2 minimizing as proposed by Kawrakow (2000b) and used in chapter 2.2.2.2 can be applied to the calculated doses inside the ionization chamber and the small reference volume. Table 3.8 shows the result for the χ^2 minimizing for various field sizes and for the complete chamber. For the calculation only the build-up region was used, i.e. depth from 0.3 cm to 2.0 cm. Furthermore it was calculated for the bare cavity and an ionization chamber without the wall as well in the 40 cm x 40 cm. Note that the shift of $0.5 r_{cav}$ recommended by the DIN 6800-2 was already included in the simulations.

The resulting small additional shifts of tenths of a millimeter can be regarded as clinically irrelevant. Still, they demonstrate, that the assumed shift of $0.5 r_{cav}$ is a practical approximation for *relative* depth-dose curves in the build-up region, although not necessarily valid for absolute dosimetry purposes (see chapter 2.2.2.2 for further discussion). However a variation with field size and construction of the ionization chamber exists.

3.3.3. Charged Particle Dis-Equilibrium in the Penumbra

As turned out in the previous section the ionization chamber response stays nearly constant under various conditions, e.g. field sizes, depth and off-axis distance, and thus the

Table 3.8.: Needed shifts as result of the χ^2 minimization according to Kawrakow (2006b). The needed shift is given in mm added to the already applied shift of $0.5 r_{\text{cav}}$. Further the resulting total shift scaled in r_{cav} (with $r_{\text{cav}} = 2.75$ mm) is shown. Uncertainty on last digits is shown in parenthesis.

square field size <i>cm</i>	additional shift away from focus <i>mm</i>	total shift times r_{cav}
3	0.16(4)	0.57(1)
10	0.16(6)	0.58(1)
40	0.22(5)	0.60(2)
40 (no electrode)	0.13(4)	0.56(1)
40 (bare cavity)	0.07(5)	0.54(2)

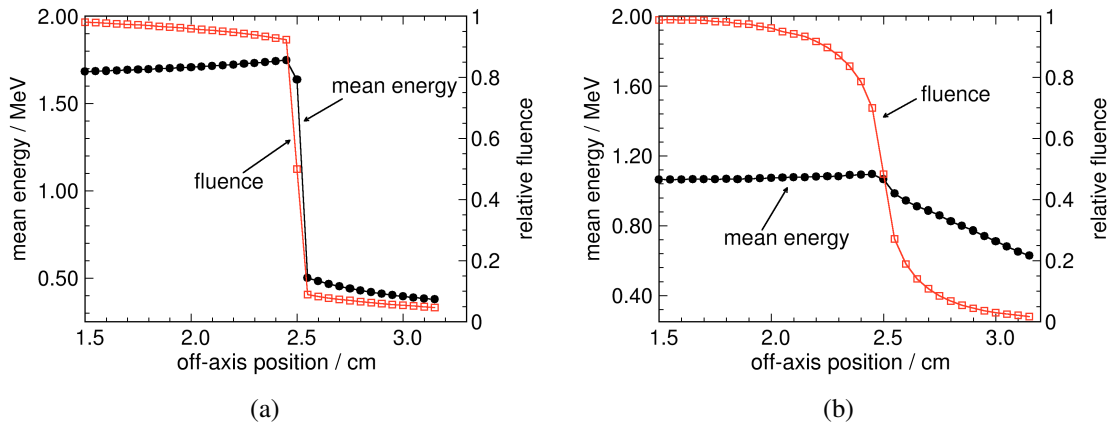


Figure 3.20.: Mean energy and fluence of photons (a) and charged particles (b) within the idealized field edge. The circular beam has a radius of 2.5 cm.

necessary corrections are close to unity as long as charged particle equilibrium conditions can be maintained.

The fluence and mean energy at the idealized field boundary of the circular 6 MV photon beam with large parts of CPD is shown in figure 3.20. Prior to the field boundary at 2.5 cm, the fluence of photons drops slightly, since photons scatter out, while no photons scatter in from outside the field. This causes the mean energy to increase slightly, since the spectrum lacks the low energy scattered photons. The fluence of photons is decreases rapidly and only some scattered photons with low energy can be found in beyond the penumbra (5-10%).

Due to their finite range the fluence of electrons drops before the field edge at 2.5 cm is reached, since the equilibrium is disturbed by lack of electrons scattering in. Electrons are scattered out, causing the sigmoidal shape of the fluence profile. The energy of electrons outside the penumbra decreases linearly. In figure 3.21 the change of the electrons spectrum is further shown as a function of off-axis distance.

In figure 3.22 the resulting individual perturbation correction factors for the PTW31010 ionization chamber (see fig. 1.5) are shown. The central electrode perturbation correction

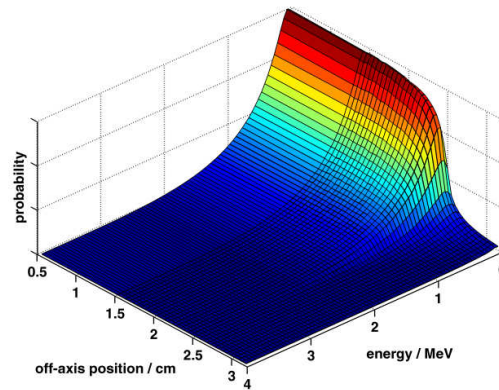


Figure 3.21.: Spectral change for electrons in the field penumbra.

factor p_{cel} and increases beyond the edge, since electrons are absorbed in the aluminum which otherwise still could cross the cavity and deposit their energy. Within the field this loss of electrons is compensated by the generation of secondary electrons inside the electrode, but outside the field the fluence of photons is too small for this compensation effect. The wall perturbation p_{wall} increases outside the field boundary, since, due to its higher density than water, more low energy electrons are absorbed in it. The largest contribution to the overall perturbation is caused by the finite volume and the perturbation of electron fluence by it. Due to the low density electrons are scattered out of the field and the ionization chamber 'sees' the edge due to its size prior to the reference volume of water. Beyond the edge the effect is reverse and the low energy electrons can contribute to the absorbed dose in the air volume. The factor p_{repl} dominates the total correction f_Q , the ratio between dose to water and the ionization chamber and which changes by $\sim \pm 40\%$.

Even practically not useful since not generalizable, these individual perturbation correction factors can be used to calculate the dose to water according to Spencer-Attix theory. This was done according to eq. 1.8 with the individual calculated perturbation factors and the sprs. The ratio of the dose actually deposited in the water and the dose calculated from the Spencer-Attix theory is shown in figure 3.23. Obviously the dose can be predicted by Spencer-Attix theory with all corresponding corrections within $\sim 1\%$ even for the case of charged particle disequilibrium. The factorization has limited meaning since due to the strong variations of the factors not necessarily being independent anymore. Furthermore, these corrections are not generalizable for a real measurement, since for the calculation the properties of the radiation source would be needed. If one is able to include them in a simulation, it seems needles to calculate individual factors, one could simply calculate the complete correction f avoiding the application of Spencer-Attix theory. Still the theory seems to be valid within the $\sim 1\%$.

The above results point out that the volume of the PTW31010 ionization chamber causes a dramatic change in the total correction for this hypothetical situation. Hence, other detectors are compared in the subsequent chapter, being more suitable to measure dose under CPD.

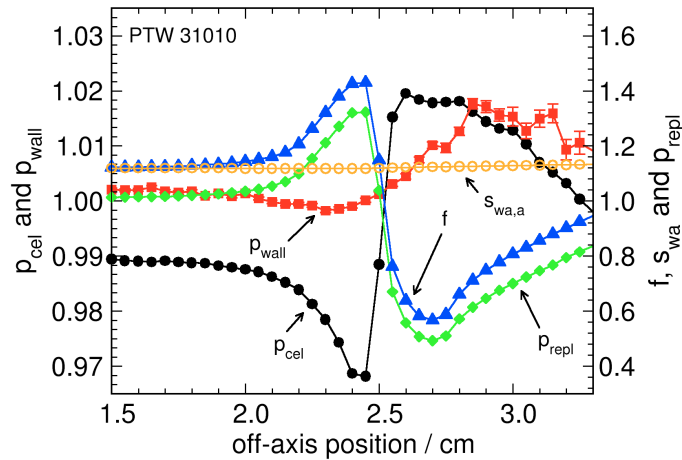


Figure 3.22.: Individual perturbation correction factors and the f -factor (see eq. 1.18) for the PTW31010 in the idealized field boundary. The primary photon beam incident on the small phantom ends at 2.5 cm. The statistical uncertainty is shown for all values, but the error-bars are smaller than the symbols in most cases.

3.3.3.1. Various Detectors

The normalized values of the total correction factor for the various detectors (see tab. 2.1) is given in figure 3.24 as a function of off-axis distance. All detectors show some deviation in the penumbral region, largest for the air-filled ionization chambers. Although having a comparatively small volume, the pinpoint type chambers show deviations of up to $\sim 20\%$. This value is much larger than one might expect, but occurs only at some distinct points where the gradient is largest. The deviation between the dose to water and dose to the ionization chamber was calculated for the penumbra of a 6 MV beam by Gonzales-Castano et al. (2007) to be much smaller. The deviations to their results might be caused by the larger dimensions of the reference volume (1 cm^3 vs. 0.5 cm^3 used here) in water and the overall less steep gradients of the beam causing an increase of the f -factor. The PTW31016 has the largest volume (see tab. 2.1) and hence shows the largest deviation. The PTW31006 is equipped with a steel electrode and is known to overrespond to low energy photon scatter. A slightly higher dose is measured with it causing the smaller relative f -factor at distinct points where only low energy scatter exists (see fig. 3.20(a)).

Diodes are generally preferred for measurements of small fields due to their small sensitive volume, still as can be seen in figure 3.24 a 10% increase in the f -factor is observable. This is mainly caused by the non water equivalent surrounding of the silicon chip and the silicon itself. Low energy electrons scattering from the side are stopped in the high Z / high density material. Since only a small portion of the whole high density and high atomic number chip serves as a sensitive volume, the response is decreased. One must keep in mind that the field edge used here is created for a parallel beam ideally collimated. Hence, the gradient is much larger than in a real penumbra. Due to the larger

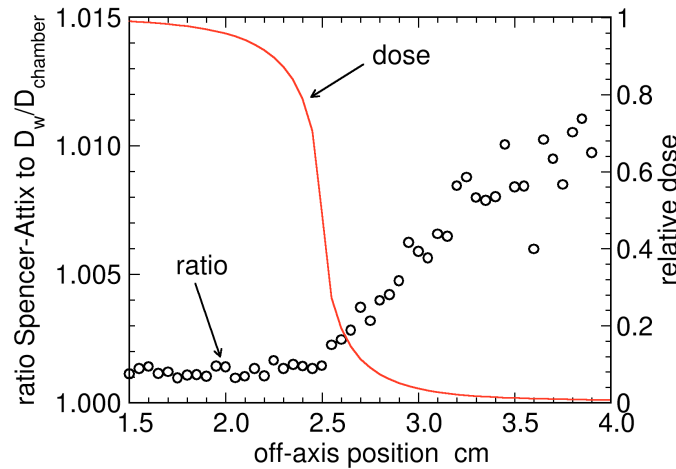


Figure 3.23.: Application of Spencer-Attix theory within the field penumbra. Shown is the dose ratio between the dose according to cavity theory and the dose in water within the idealized field penumbra.

volume, the diode is irradiated more by photons than the reference water volume and close to the boundary within the field more secondary electrons are generated within the higher density silicon and housing, depositing more dose within the detector. Hence, the f -factor drops slightly below unity close to the boundary.

Comparatively the film leads to a small underresponse, caused by absorption of electrons from the side within the film. This fact leads to a small increase of the f -factor by $\sim 3\text{-}4\%$ being in the same order as reported by Paskalev et al. (2003) who investigated the response of silver halide film in small photon fields in a similar manner. Other authors avoided the film for determination of the dose distribution in the penumbra due to its assumed increased response to low energy photons (Martens et al., 2000). As turns out here, the film shows the smallest deviation from the reference and any overresponse to photons plays only a minor role and is even reverse at the points ≥ 2.5 cm.

The calculated f -factor for the TLD rods is larger unity in beyond the field boundary, indicating a smaller dose measured in the TLD than in water. This is surprising since the LiF volume is larger than the reference volume made of water and one could expect an averaging effect as in the case of the ionization chamber. Further, the mass-energy absorption coefficient is larger for LiF at energies below ~ 100 keV. Since the whole rod serves as a sensitive volume, the explanation given for the film or diode does not apply here. The higher scattering power of the dense LiF presumably leads to a perturbation, which decreases the electron fluence and hence to an increased f -factor at distinct points away from the penumbra.

The liquid ionization chamber shows a similar behavior as the ionization chambers due to the dimensions of the sensitive volume leading to some amount of averaging.

The change of response of the different detectors expressed in the f -factor results in a change of the slope of a measured dose profile. This has a more practical consequence, since the shape of profiles might be used to match the primary electron beam parameters in Monte Carlo models of linear accelerators and for the description of primary fluence

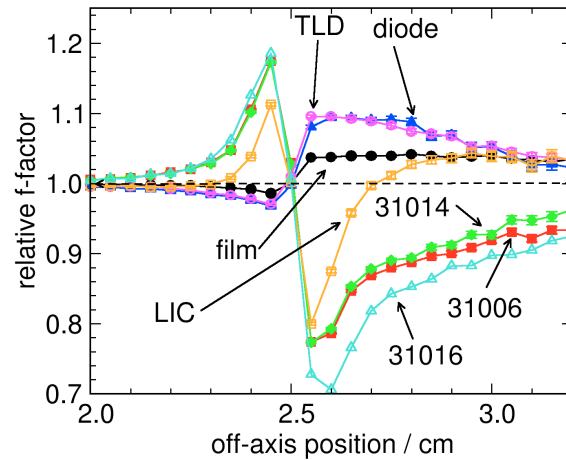


Figure 3.24.: Calculated deviation between dose to water and detector reading for various types of detectors in terms of the relative f -factor, normalized to the central axis value.

Table 3.9.: Penumbra broadening for various detectors (see tab. 2.1) in the hypothetical field of a 6 MV beam. The broadening was calculated for the distance between the 80% and 20% value of the relative dose profile of 2.0 mm. For comparison see fig. 3.24.

detector	broadening <i>mm</i>
SFD	-0.30
TLD	-0.28
film	-0.11
LIC	0.31
PTW31014	+0.72
PTW31006	+0.73
PTW31016	+0.96
PTW31010	+2.71

for other conventional treatment planning algorithms. Table 3.9 summarizes the calculated penumbra broadening between the 80% and 20% value of the relative dose profile. While the air volume of the ionization chambers lead to a broadening of the profiles, the other detectors cause steeper profile. For diodes this effect is known from measurements and called “pseudo-sharpening” (Heydariyan et al., 1996). The penumbra broadening calculated for the pinpoint type chambers is comparable to the measurements of Martens et al. (2000).

3.3.4. Summary

Ion chambers are recommended by all current dosimetry protocols for the determination of absorbed dose. Their behavior under non-reference conditions is mostly unknown. A realistic linear accelerator model, matched to measurements, was used to calculate corrections for non-reference conditions. As long as CPE can be guaranteed, the corrections are generally below 0.5% for a commonly used ionization chamber. In the build-up region deviations might be larger, which can be reduced with a more appropriate positioning of the detector.

Under charged particle dis-equilibrium the perturbations of the detector are much larger. Most importantly, the replacement correction within steep dose gradients, caused by the volume of ionization chambers, leads to an influence of up to 40%, being one order of magnitude higher than other perturbations. No optimal detector exists for the measurement under CPD. The smallest perturbation both in terms of changed response and changed penumbra width can be achieved with film. As long as the detector volume is small enough, the ionization chambers can be used for the determination of the penumbra width within ≤ 1 mm accuracy. One must further keep in mind, that the field boundary investigated here is rather a worst case scenario, since a real penumbra will possibly be less sharp.

4. SUMMARY AND CONCLUSION

This study presents an extensive and consistent investigation of ionization chamber dosimetry in photon beam radiotherapy. Monte Carlo methods have been extended and applied to investigate the current concepts in clinical dosimetry with ionization chambers. These simulations are the most accurate way of calculating radiation transport through medium and allow the calculation needed corrections in ionization chamber dosimetry.

The effects of perturbations due to the presence of ionization chambers are small and hence these simulations require elaborate variance reduction techniques, in order to achieve small statistical uncertainties on the calculated results. Methods to increase the efficiency in ionization chamber calculations were implemented into the established EGSnrc Monte Carlo code environment. These methods include a local cross section enhancement for photons, a range based Russian Roulette for charged particles, a correlated sampling scheme and an intermediate storing of the particles phase-space. These methods are chosen in such a way that minimal time is spend on particles transport where it is unnecessary and increasing the interaction probability at points of interest. A gain in efficiency for a single ionization chamber's cavity dose calculation of up to a factor of 650 compared to simulations without variance reduction techniques could be achieved. The efficiency gain was even higher for the calculation of ionization chamber perturbation correction factors and cavity doses at more than one location, reaching a factor of nearly 10^4 when calculating the p_{cel} perturbation factor within a cross profile. This dramatic increase in efficiency allowed the detailed investigation of ionization chamber dosimetry in photon beams under various conditions.

Furthermore the use of track length estimators was investigated for the calculation of kerma in homogeneous water phantoms. The implementation in its exponential form lead to an increase in efficiency of up to 130 compared to the most efficient way of calculating dose distributions in a homogeneous phantom employing with the EGSnrc code. Hence, this method might be an efficient way of estimating the relative dose distribution during the process of beam commissioning a linear accelerator model as long as the ionization chamber response stays constant and the kerma approximation is a valid assumption.

Perturbation factors were calculated for a NE2571 ionization chamber model which is a commonly used type for clinical absolute dosimetry purposes. The comparison to the data for single perturbation correction factors found in dosimetry protocols revealed some discrepancies. The deviations of the p_{wall} perturbation correction factor in the order of $\geq 0.5\%$ could be addressed to the underlying models used in the dosimetry protocols, since even the appropriate calculations of all quantities as needed in the formulations of Almond-Svensson lead to a disagreement to the direct calculated values, but to an agreement with the ones in the dosimetry protocols. The deviations for the replacement correction was even larger and could be addressed to the measurements available to this point and the definition of this factor itself. A method for the calculation of the p_{Δ} -factor as introduced in the current German dosimetry protocol DIN 6800-2 was developed, but the factor turned out to be less than 0.1% and can therefore regarded as clinically irrelevant. The total correction factors k_Q were calculated for the NE2571 and showed a good agreement with the currently available data based on measurements. Though, depending

on the cross section used in the calculations, a fairly large deviation of $\sim 0.5\%$ compared to the values used in dosimetry protocols results.

This influence of the underlying cross sections, lead to the investigation of the systematic uncertainties for these calculations, despite the promising results of the calculated beam quality correction factors k_Q in a reasonable amount of time. A systematic method for the investigation of the magnitude of these influences (type B uncertainties) were applied to the calculations and revealed a comparatively large possible influence of 1%. No investigation of this type is known up to today, so this important result needs to be kept in mind, given the amount of currently upcoming studies on correction factors based on Monte Carlo simulations.

A virtual linear accelerator model of a Siemens KD was employed to investigate the behavior of a common ionization chamber within the field under non-reference conditions. The accelerator was matched to measurements considering the primary electron parameters. The procedure of this commissioning was based on large field profiles and small field profiles' penumbra. Latter ones turned out to be most sensitive to the spot size of the primary electron beam hitting the target. The inclusion of the ionization chamber model within these simulations was necessary, due to the averaging effect of the air-filled chambers volume. The overall agreement to measurements was excellent and for most points within 1%/1 mm. The calculated monitor chamber backscatter was negligible.

Single perturbation factors and the corresponding factor k_{NR} were calculated for a commonly employed ionization chamber model at single positions inside a water phantom within the field of the 6 MV linear accelerator model. The single perturbation factors turned out to be small and tend to compensate each other. Hence, as long as charged particle equilibrium was maintained, the k_{NR} corrections were $\sim \pm 0.5\%$. In the build-up region higher corrections or a different placement of the ionization chamber deviating from the commonly used $0.5 r_{cav}$ concept were calculated. Still, the change in positioning was in the order of a few tenth of millimeters only.

Within the high dose gradient of an idealized 6 MV beam field boundary where charged particle *dis*-equilibrium exists, the corrections were much larger and up to $\sim 40\%$, dominated by the volume of the ionization chamber and the replacement of water with the air of the cavity. Still, the application of the Spencer-Attix theory was estimated to be valid within 1%, although the nessecary correction are not generalizable for practicable dosimetry.

Other detectors where compared within the idealized field boundary and compared in their ability to measure the penumbra width. The lowest deviations from the ideal profile were given by the film model. Even air-filled micro-ionization chambers with a sensitive volume of 0.015 cm^3 showed a strong perturbation of $\sim 20\%$ for some points within the penumbra. However, if the task of relative dosimetry is to characterize a beam cross profile within an accuracy of 1 mm all small volume detectors were able to fullfil this requirement. Ion chambers will probably remain the most common detector type for now.

As proposed by Das et al. (2008a) "... *it is expected that calculation-aided dosimetry will be available where specific correction and perturbation correction factors are either precalculated for irradiation geometry or calculated on-line ... it is likely that empirical*

corrections will be replaced by calculated correction factors.”. This study presents the application of this idea for the calculation of beam quality correction factors under reference and non-reference conditions. The methods developed are applicable to various situations and all types of radiation detectors. Currently new radiotherapy techniques such as Tomotherapy or the Cyber-knife are introduced to the clinical routine, where the classical reference conditions required by the dosimetry protocols cannot be applied. The behavior of ionization chambers is mostly unknown in these situations. Simulations of the kind presented here will help to develop corresponding corrections to allow appropriate methods for a quality assurance. Currently worldwide all treatment planning system vendors are incorporating Monte Carlo based algorithms for dose calculation. One could envision that in future systems the ionization chamber models employed by the user are part of these systems.

5. Abstract

Practical clinical dosimetry is a fundamental step within the radiation therapy process and aims at quantifying the absorbed radiation dose within a 1-2% uncertainty. To achieve this level of accuracy, corrections are needed for calibrated and air-filled ionization chambers, which are used for dose measurement. The procedures of correction are based on cavity theory of Spencer-Attix and are defined in current dosimetry protocols. Energy dependent corrections for deviations from calibration beams account for changed ionization chamber response in the treatment beam. The corrections applied are usually based on semi-analytical models or measurements and are generally hard to determine due to their magnitude of only a few percents or even less. Furthermore the corrections are defined for fixed geometrical reference-conditions and do not apply to non-reference conditions in modern radiotherapy applications.

The stochastic Monte Carlo method for the simulation of radiation transport is becoming a valuable tool in the field of Medical Physics. As a suitable tool for calculation of these corrections with high accuracy the simulations enable the investigation of ionization chambers under various conditions. The aim of this work is the consistent investigation of ionization chamber dosimetry in photon radiation therapy with the use of Monte Carlo methods.

Nowadays Monte Carlo systems exist, which enable the accurate calculation of ionization chamber response in principle. Still, their bare use for studies of this type is limited due to the long calculation times needed for a meaningful result with a small statistical uncertainty, inherent to every result of a Monte Carlo simulation. Besides heavy use of computer hardware, techniques methods of variance reduction to reduce the needed calculation time can be applied. Methods for increasing the efficiency in the results of simulation were developed and incorporated in a modern and established Monte Carlo simulation environment. The efficiency of ionization chamber calculations could be improved by several orders of magnitude.

Using the developed methods, current clinical dosimetry protocols for the determination of absorbed dose to water under reference conditions in photon beams were reviewed. Calculations of correction factors were performed and compared to the currently existing data. It could be shown that the calculated values are in agreement with recent data, mainly based on calorimetric measurements, but partially deviate from currently used data in dosimetry protocols by $\sim 1\%$. Reason for these discrepancies are outdated theories and measurements for the single underlying perturbations. Sources of uncertainties in the calculated results based on Monte Carlo simulations were investigated, also considering uncertainties in underlying cross sections as input for these calculations. It could be shown that following a conservative estimation, systematic uncertainties of $\leq 1\%$ might be adherent to the calculated results, a fact that is barely considered in recent works.

Ion chambers under non-reference conditions were investigated with the use of a virtual model of a clinical linear accelerator. Besides developing a procedure for commissioning the model i.e. adapting it to measurements with respect to primary electron characteristics, these calculations aimed at answering the question how ionization chambers

behave in non-reference geometrical conditions. It turned out that commonly used ionization chambers show only small changes in response under non-reference conditions when fulfilling the condition of charged particle equilibrium.

In contrast, whenever charged particle disequilibrium and high dose gradients exists, i.e. in the penumbra of a small radiation field, a strong change in detector response might occur. The applicability of the Spencer-Attix theory under these severe conditions was tested. It could be shown that, within a 1% uncertainty, the application of the Spencer-Attix theory with corresponding perturbation factors is valid. A further investigation of these conditions when measuring dose profiles was used to determine the type of detector with minimal change in response for regions of charged particle disequilibrium and high dose gradients. In terms of penumbra broadening, radiochromic film shows the smallest deviation from dose to water.

Monte Carlo simulations will replace or at least extend the existing data in clinical dosimetry protocols in order to reduce the uncertainty in radiotherapy. For corrections under non-reference conditions as occurring in modern radiotherapy techniques, Monte Carlo calculations will be a crucial part. This work and the developed methods accordingly form an important step towards reduced uncertainties in radiotherapy for cancer treatment.

6. Zusammenfassung

Die klinische Dosimetrie ist ein fundamentaler Schritt im Rahmen der Strahlentherapie und zielt auf eine Quantifizierung der absorbierten Energiedosis innerhalb einer Unsicherheit von 1-2%. Um eine entsprechende Genauigkeit zu erreichen, müssen Korrekturen bei Messungen mit luft-gefüllten, kalibrierten Ionisationskammern angewendet werden. Die Anwendung der Korrekturen basiert auf der Hohlraumtheorie nach Spencer-Attix und wird in den jeweiligen, aktuellen Dosimetrieprotokollen definiert. Energieabhängige Korrekturen berücksichtigen die Abweichung von Kalibrierbedingungen und die damit verbundene Änderung des Ansprechvermögens von Ionisationskammern im Therapiestrahle. Die üblicherweise angewendeten Korrekturen basieren auf semi-analytischen Modellen oder auf Vergleichsmessungen und sind auf Grund der Größenordnung von einigen Prozent oder weniger schwierig zu quantifizieren. Weiterhin werden die Korrekturen für feste geometrische Referenzbedingungen definiert, die nicht zwangsläufig mit den Bedingungen in den modernen Strahlentherapie-Anwendungen übereinstimmen.

Das stochastische Monte-Carlo Verfahren zur Simulation von Strahlungstransport gewinnt zunehmend Bedeutung in der Medizinischen Physik. Es stellt ein geeignetes Werkzeug zur Berechnung dieser Korrekturen mit einer prinzipiell hohen Genauigkeit dar und erlaubt die Untersuchung von Ionisationskammern unter verschiedensten Bedingungen. Ziel der vorliegenden Arbeit ist die konsistente Untersuchung der gängigen Ionisationskammer-Dosimetrie in der Strahlentherapie mit Photonen unter Anwendung von Monte-Carlo Simulationen.

Heutzutage existieren Monte-Carlo Algorithmen, die die präzise Berechnung des Ansprechvermögens von Ionisationskammern prinzipiell erlauben. Dem Ergebnis einer Monte Carlo Simulation haftet allerdings immer eine statistische Unsicherheit an. Untersuchungen dieser Art sind damit durch lange Berechnungszeiten, die für ein signifikantes Ergebnis innerhalb kleiner statistischer Unsicherheiten entstehen, nur begrenzt möglich. Neben der Verwendung großer Rechnerkapazitäten, lassen sich so genannte Varianzreduktions-Verfahren anwenden, die die benötigte Simulationszeit verringern. Entsprechende Methoden zur Steigerung der Recheneffizienz um mehrere Größenordnungen wurden im Rahmen der Arbeit entwickelt und in ein modernes und etabliertes Monte-Carlo Simulationspaket implementiert.

Mit Hilfe der entwickelten Methoden wurden Daten aktueller klinischer Dosimetrieprotokolle zur Bestimmung der Wasserenergiedosis unter Referenzbedingungen in Photonenstrahlung untersucht. Korrekturfaktoren wurden berechnet und mit den existierenden Daten in der Literatur verglichen. Es konnte gezeigt werden, dass berechnete Daten in guter Übereinstimmung mit aktuellen Messdaten liegen, allerdings teilweise von den in Dosimetrieprotokollen genutzten Daten um $\sim 1\%$ abweichen. Ursache hierfür sind z.T. überholte Theorien und jahrzehnte alte Messungen zu einzelnen Störungsfaktoren. Quellen von Unsicherheiten in den durch Monte-Carlo Simulationen berechneten Daten wurden untersucht, auch unter Berücksichtigung von Unsicherheiten in den Wirkungsquerschnitten, die den Simulationen zu Grunde liegen. Im Sinne einer konservativen Abschätzung zeigten sich dabei systematische (Typ B) Unsicherheiten von $\leq 1\%$.

Ionisationskammern unter Nicht-Referenzbedingungen wurden mit Hilfe eines virtu-

ellen Linearbeschleuniger-Modells untersucht. Neben der Entwicklung einer Methodik zur Kommissionierung, d.h. dem Anpassen des Modells an Messungen hinsichtlich der Eigenschaften des primären Elektronenstrahls, war das Ziel dieser Berechnungen eine Untersuchung des Verhaltens von Ionisationskammern unter geometrischen Nicht-Referenzbedingungen. Es konnte gezeigt werden, dass die üblicherweise eingesetzten Ionisationskammertypen nur kleine Abweichungen in ihrem Ansprechvermögen zeigen, solange Sekundärelektronen-Gleichgewicht vorausgesetzt werden kann.

Demgegenüber zeigen Detektoren eine starke Änderung ihres Ansprechvermögens in Regionen, in denen kein Sekundärelektronen-Gleichgewicht und damit ein hoher Dosisgradient vorliegt, wie etwa im Feldrand. Die Anwendbarkeit der Spencer-Attix Theorie unter diesen Bedingungen wurde überprüft und es konnte gezeigt werden, dass innerhalb von $\sim 1\%$ die Bestimmung der Wasserenergiedosis mit Hilfe der Korrekturfaktoren möglich ist. Eine weitere Untersuchung dieser Bedingungen bei der Messung von Profilen wurde genutzt, um einen Detektortyp zu bestimmen, der die geringsten Abweichungen in seinem Ansprechvermögen in Regionen mit Sekundärelektronen-Ungleichgewicht und hohen Dosisgradienten zeigt. Hinsichtlich der Verbreiterung des Feldrands zeigt die Filmdosimetrie die geringsten Abweichungen zu einem idealen Profil.

Langfristig werden Monte-Carlo Simulationen die Daten in klinischen Dosimetrie-protokollen ersetzen oder zumindest erweitern, um eine Verringerung der Unsicherheiten bei der Strahlenanwendung am Menschen zu erreichen. Für Korrekturen in Nicht-Referenzbedingungen wie sie in modernen strahlentherapeutischen Anwendungen auftreten, werden Monte-Carlo Simulationen eine entscheidende Rolle spielen. Die in dieser Arbeit entwickelten Methoden stellen dementsprechend einen wichtigen Schritt zur Verringerung der Unsicherheiten in der Strahlentherapie dar.

A. Monte-Carlo Simulation von Strahlungstransport - Eine knappe Einführung

Das Wissen über die elementaren Wechselwirkungsprozesse, erlaubt die Simulation von Strahlungstransport mittels des so genannten Monte-Carlo Verfahrens. Allgemein lässt sich das Monte-Carlo Verfahren als eine statistische Methode zur numerischen Integration unter Verwendung von Zufallszahlen definieren. Erste Beschreibungen dieser Technik reichen zurück ins Jahr 1777 (Buffon's Nadelexperiment (de Buffon, 1777)), erste populäre Beispiele im Zusammenhang mit der computergestützten Simulation von Strahlungstransport finden sich bei der Entwicklung von Nuklear-Waffen am Ende des zweiten Weltkriegs (Kalos and Whitlock, 2004; Eckhardt, 1987). Vor allem die zunehmende Leistungsfähigkeit moderner Computer haben bei der Verbreitung der Technik eine entscheidende Rolle gespielt und machen sie heute zu einem etablierten Werkzeug im Bereich der Medizinischen Physik.

Das Buffon Nadelexperiment

Der französische Naturforscher Comte de Buffon beschrieb 1777 folgendes Experiment: Eine Nadel der Länge L wird zufällig auf den Fußboden geworfen, der in Planken mit dem Abstand d (mit $d \leq L$) unterteilt ist. In Abbildung A.1(a) ist das Experiment schematisch dargestellt.

Wie groß ist nun die Wahrscheinlichkeit P , dass die Nadel die Fuge zwischen zwei Planken berührt? Eine experimentelle Untersuchung zeigt nach einer Vielzahl von einzelnen, zufällig geworfenen Nadeln, dass das Ergebnis nach

$$P = \frac{\text{Treffer}}{\text{geworfeneNadeln}} = \frac{2L}{D\pi} \quad (\text{A.1})$$

konvergiert. Diese Wahrscheinlichkeit ergibt sich aus der Forderung nach $x \leq y = \frac{1}{2}L \sin \theta$ (siehe Abbildung A.1(b)), mit zufälligen Positionen $x[0, D/2]$ und Winkeln $\theta[0, \pi]$, wobei beide Größen gleich verteilt und unabhängig voneinander vorliegen.

Für $D = L$ lässt sich die Kreiszahl π einfach aus einer Monte-Carlo Simulation des Nadelexperiments ableiten, wie bereits Laplace vorschlug (Kalos and Whitlock, 2004). Dazu werden θ und x zufällig gewählt und entsprechend die Treffer bzw. die Anzahl der Versuche gezählt. In Abbildung A.2 ist das Ergebnis einer Computer-Simulation zur Bestimmung von π als Funktion der geworfenen Nadeln als Stichproben gezeigt. Trotz der Einfachheit dieses Beispiels lassen sich einige allgemeine, entscheidende Aussagen aus Abbildung A.2 hinsichtlich einer Monte-Carlo Simulation treffen:

- Das Ergebnis konvergiert mit zunehmender Stichprobenzahl N zum erwarteten Wert, in diesem Fall die Abweichung null. Der Rechenaufwand ist direkt proportional zur Anzahl dieser einzelnen Stichproben.

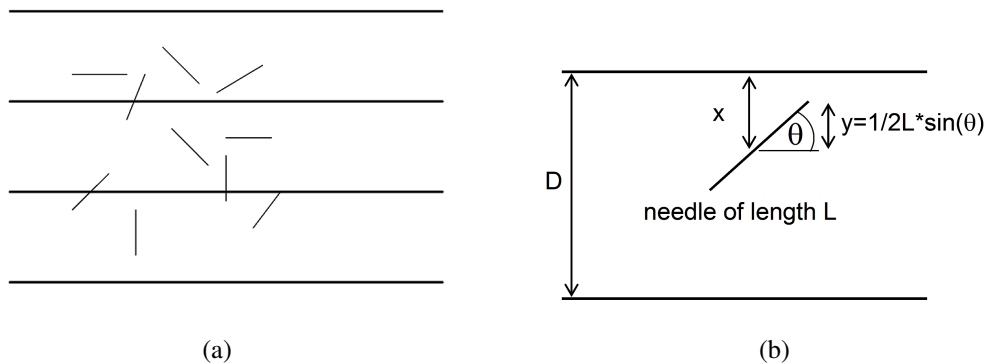


Abbildung A.1.: Darstellung des Buffon Nadelexperiments. Nadeln der Länge L werden zufällig auf die Ebene geworfen, die durch die horizontalen Fugen im Abstand D unterteilt sind. A.1(b): Die Nadeln treffen nur dann die Fuge, wenn gilt $x \leq y$, bei einem Winkel θ zwischen Nadel und Fuge.

- Für unterschiedliche Experimente oder Folgen von Zufallszahlen d.h. zufälligen Werten von θ und x ist das Ergebnis der Simulation unterschiedlich.
- Die Standardabweichung liefert eine gute Schätzung für die Unsicherheit des ermittelten Wertes, allerdings liegen nicht alle Werte innerhalb des $1 \sigma \approx 68.3\%$ Intervalls.

Das Prinzip der Monte-Carlo Integration

Im Folgenden wird nun eine formale Beschreibung der Monte-Carlo Integration eingeführt. Das Integral der Funktion $F(x)$ in den Grenzen a und b

$$I = \int_a^b F(x) dx \quad (\text{A.2})$$

lässt sich einfach umformen zu

$$I = \int_a^b f(x) p(x) dx \quad (\text{A.3})$$

mit der *probability density function* (PDF) $p(x)$, die die Wahrscheinlichkeit widerspiegelt, den Wert x im Intervall $[x, x + dx]$ aufzufinden. Die PDF hat dabei die zwei wichtigen Eigenschaften

$$\int_{x_{\min}}^{x_{\max}} p(x) dx = 1 \quad (\text{A.4})$$

und

$$p(x) \geq 0. \quad (\text{A.5})$$

Mit anderen Worten gibt es keine negative Wahrscheinlichkeit für das Auftreten von x . Weiterhin ist die Gesamtwahrscheinlichkeit, dass innerhalb der Grenzen ein Wert aufzu-

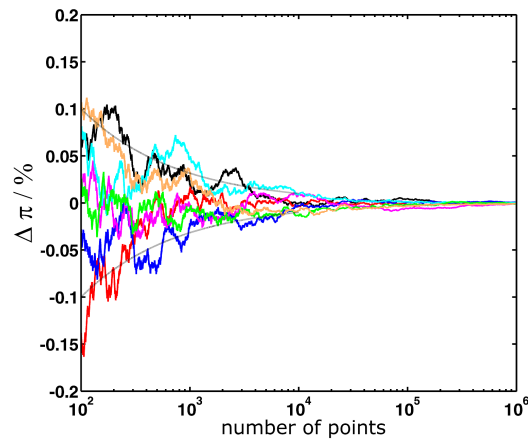


Abbildung A.2.: Berechnung von π mittels Monte-Carlo Simulation des Nadelexperiments nach Buffon. Aufgetragen ist die Abweichung des berechneten Werts von π als Funktion der Versuche. Die einzelnen Kurven entsprechen unterschiedlichen Simulationen mit unterschiedlichen Zufallszahlen. Die durchgezogenen grauen Linien folgen $1/\sqrt{N}$ und sind damit proportional zur Standardabweichung (1σ) des berechneten Werts.

finden ist, gleich eins. Das Integral in Gleichung A.4 liefert das 1. Moment der Funktion $f(x)$ bzw. den Erwartungswert $\langle f \rangle$. In einer Monte-Carlo Integration ersetzt man nun das Integral in Gleichung A.4 durch eine Summe und wählt zufällige Werte $f(x)$ entsprechend $p(x)$ aus, so dass gilt

$$\bar{f} = \frac{1}{N} \sum_i^N f(x_i) \quad (\text{A.6})$$

Die Standardabweichung σ des Mittelwerts \bar{f} bzw. eine entsprechende Schätzung s ergibt sich nach

$$s_{\bar{f}} = \sqrt{\frac{\text{var} \{f(x)\}}{N}} \quad (\text{A.7})$$

mit der (geschätzten) Varianz

$$\text{var} \{f(x)\} = \frac{1}{N} \sum_i^N [f(x_i)]^2 - \left[\sum_i^N f(x_i) \right]^2 \quad (\text{A.8})$$

womit eine entsprechend große Stichprobenzahl N für ein Ergebnis innerhalb von sinnvollen Konfidenz-Intervallen nötig wird. Durch die Wurzelfunktion in Gleichung A.7 muss die Stichprobenzahl vervierfacht werden, um die Standardabweichung zu halbieren!

Für $N \rightarrow \infty$ geht die Summe in Gleichung A.6 dem Gesetz der großen Zahl folgend wieder in das Integral über und der Mittelwert \bar{f} wird zum Erwartungswert $\langle f \rangle$. Nach dem zentralen Grenzwertsatz (*central-limit theorem*) folgt das Ergebnis der Monte-Carlo

Integration immer einer Gauß-Verteilung und der Mittelwert der berechneten Größe liegt innerhalb der Intervalle $\pm\sigma$, *unabhängig* von den einzelnen Wahrscheinlichkeitsverteilungen, die der Berechnung zu Grunde liegen.

Sampling

Häufig sind die PDF's gleichverteilt, wie im Beispiel des Buffon Nadelexperiments (gleichverteilte Zufallszahlen θ und x) oder der einfachen Monte-Carlo Integration. Für die Simulation von Strahlung besteht die Aufgabe jedoch vielmehr darin, die computergenerierten, gleichverteilten Zufallszahlen in die jeweiligen Wahrscheinlichkeitsverteilungen bzw. den entsprechenden Streuquerschnitten zu transformieren. Diese können beispielsweise Gauß-, exponentiell oder diskret verteilt vorliegen. Verschiedene Techniken zur Stichprobenziehung, dem *sampling* existieren (Kalos and Whitlock, 2004); hier sollen prinzipielle Ideen veranschaulicht werden.

Die einfachste und intuitivste Art des *sampling* ist die "direkte Methode". Für eine PDF lässt sich allgemein eine kumulative Wahrscheinlichkeitsverteilung definieren

$$c(x) = \int_{x_{min}}^x p(x') dx' \quad (\text{A.9})$$

womit gilt

$$c(x_{min}) = 0, c(x_{max}) = 1 \quad (\text{A.10})$$

Lässt sich die monoton wachsende Funktion $c(x)$ zu $c^{-1}(\xi)$ invertieren, so kann mit einer Zufallszahl $\xi[0,1]$ eine Größe x entsprechend der Verteilung $p(x)$ als Stichprobe gewählt werden.

Nicht immer lässt sich jedoch für eine Funktion die inverse Funktion c^{-1} bilden. Die *rejection method* lässt sich prinzipiell für jede beliebige Funktion $p(x)$ anwenden, allerdings wird sie bei Funktionen mit extremen Maxima ineffizient. Bei dieser Methode werden zufällige Werte im Funktionsintervall $[a, b]$ mit $x = a + (b - a)\xi_1$ gewählt und mit einer zweiten Zufallsvariablen ξ_2 entschieden, ob der Wert angenommen wird ($\xi_2 \leq p(x)/p_{max}$) oder nicht. In Abb. A.3 ist die Idee veranschaulicht.

Viele Verteilungen liegen als zweidimensionale Funktionen $p(x, y)$ vor. Zufällige Werte x und y lassen sich formal mit Hilfe der *marginalen* Wahrscheinlichkeit

$$m(x) = \int_{y_{min}}^{y_{max}} p(x, y) dy \quad (\text{A.11})$$

beziehungsweise

$$m(y) = \int_{x_{min}}^{x_{max}} p(x, y) dx \quad (\text{A.12})$$

und der *bedingten* Wahrscheinlichkeit

$$p(x|y) = \frac{p(x, y)}{m(y)} \quad (\text{A.13})$$

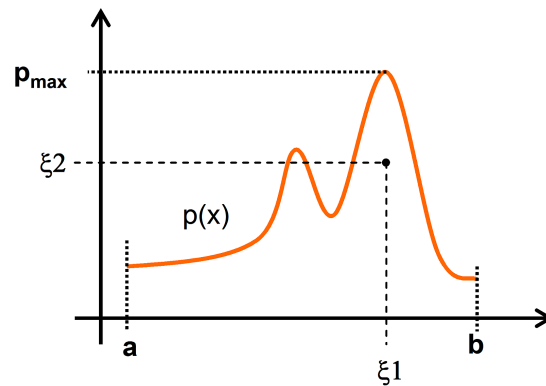


Abbildung A.3.: Rejection method. Die Funktion $p(x)$ im Intervall wird auf ihr Maximum p_{max} normiert. Zufällige Werte im Intervall zwischen a und b werden angenommen, wenn für eine zweite, zufällige Zahl gilt $\xi_2 \leq p(x)/p_{max}$. Dies ist der Fall für alle Punkte unter der Kurve. Andernfalls wird die Prozedur wiederholt.

beziehungsweise

$$p(y|x) = \frac{p(x, y)}{m(x)} \quad (\text{A.14})$$

ermitteln. Die marginale PDF mit der funktionalen Abhängigkeit von einer der beiden Variablen liefert dabei die Möglichkeit, x oder y zu ermitteln und anschließend mit der bedingten PDF, die verbleibende Variable zufällig zu ermitteln. Damit lassen sich unabhängig zwei Werte z.B. mit einer der beiden oben beschriebenen sampling-Methoden oder einer Kombination daraus ermitteln.

Computergenerierte Zufallszahlen

Grundlage einer jeden Monte-Carlo Simulation sind Zufallszahlen, mit denen das stochastische Auftreten natürlicher Prozesse simuliert werden kann. Die Idee, einen Computer-Algorithmus für diese Aufgabe heranzuziehen, führte zur Bezeichnung "pseudorandom number generators"(RNG). Dennoch sind moderne RNGs in der Lage, unkorrelierte Zahlenfolgen zu generieren, die von einer wahren, zufälligen Folge z.B. einem elektrischen Rauschen nicht zu unterscheiden sind. An der Entwicklung entsprechender Algorithmen wurde für Jahrzehnte gearbeitet und auch heute noch wird aktiv an RNGs geforscht (Bielajew, 2001). Besondere Herausforderung ist dabei die Generierung langer Folgen mit bis zu 10^{18} Zufallszahlen und dabei eine fehlende Korrelation in mehreren Dimensionen sicherzustellen. Letztere Forderung ist so zu verstehen, dass zufällige Zahlen in einem Raum z.B. aus drei Dimensionen keine periodischen Strukturen, wie etwa Ebenen darstellen.

Grundsätzlich ließen sich auch natürliche Rauschquellen für eine Monte-Carlo Simulation verwenden, wie z.B. das erwähnte elektrische Rauschen oder der radioaktive Zerfall eines Isotops. Neben der Schwierigkeit bei einer technischen Umsetzung, haben

computergenerierte Zufallszahlen allerdings den Vorteil, exakt reproduzierbar zu sein. Diese Reproduzierbarkeit ist für die Fehlersuche bei der Entwicklung von Monte-Carlo codes hilfreich und kann sogar gezielt genutzt werden, um eine Simulation effizienter zu gestalten.

Die einfachste Klasse von RNGs sind die sogenannten "linear congruential generators" (LCRNG). Eine Zufallszahl ξ im Intervall lässt sich dabei mit

$$\xi_{n+1} = \text{mod}(A \cdot \xi_n + C, M) \quad (\text{A.15})$$

erzeugen, wobei die Modulus-Division (*mod*) oftmals mit $M = 2^{32}$ durchgeführt wird. Der Faktor A stellt in obiger Gleichung einen "magic" Multiplikator dar (z.B. 69069). Die Konstante C als gerade Zahl und der *seed* ξ_0 als Startwert liefern eine Folge von Zufallszahlen zwischen $0 \leq \xi \leq M$, im Fall eines 32bit Systems also ca. 4 Millionen. Das Ergebnis der Modulus-Division als Rest der Division ist dabei stets eine zufällige ganze Zahl. Eine Umrechnung erfolgt anschließend auf eine Fließkommazahl r im Intervall $[0,1]$ mit

$$r = 0.5 + \xi/2^{32} \quad (\text{A.16})$$

Eine Vereinfachung des beschriebenen LCRNG ist der "multiplicative congruential generator" (MCRNG) und kann erreicht werden, wenn C gleich 0 gesetzt wird und die Modulus-Operation entfällt. Mit einer großen Ganzzahl ξ_0 als Startwert und dem Faktor A lässt sich eine Zufallszahl nach

$$\xi_{n+1} = \xi_n \cdot A \quad (\text{A.17})$$

berechnen.

MCRNG und LCRNG können in vielen Fällen die Anforderungen hinsichtlich der Länge und fehlenden Korrelation nicht erfüllen, so dass komplexere Generatoren wie z.B. RANMAR oder RANLUX zum Einsatz kommen (Bielajew, 2001). Allen RNGs ist in der Regel gemein, dass ein Startwert (*seed*) die Folge der Zufallszahlen bestimmt. Durch den zufälligen Charakter einzelner Ergebnisse einer Monte-Carlo Simulation, lässt sich diese prinzipiell auf beliebig vielen Computern parallelisieren. Dabei muss aber vorausgesetzt werden, dass die einzelnen Simulationen tatsächlich unabhängig voneinander sind. Dies wird erreicht, indem jede Simulation mit einem eigenen *seed* des RNG begonnen wird.

Simulation von Strahlungstransport

Allgemein gesprochen wird bei der Monte-Carlo Simulation von Strahlungstransport das Wissen über einzelne *mikroskopische* Wechselwirkungen von Strahlung bzw. Partikeln im Medium mit Hilfe von entsprechenden differentiellen Streuquerschnitten als Wahrscheinlichkeitsverteilungen für Energie- und Impulsänderungen angewendet. Computererzeugte Zufallszahlen werden genutzt, um zufällige Wege eines Teilchens aus entsprechenden Verteilungen "auszuwürfeln". Jedes primäre Teilchen kann viele weitere Teilchen höherer Generationen erzeugen (z.B. δ -Elektronen), womit sich das gesam-

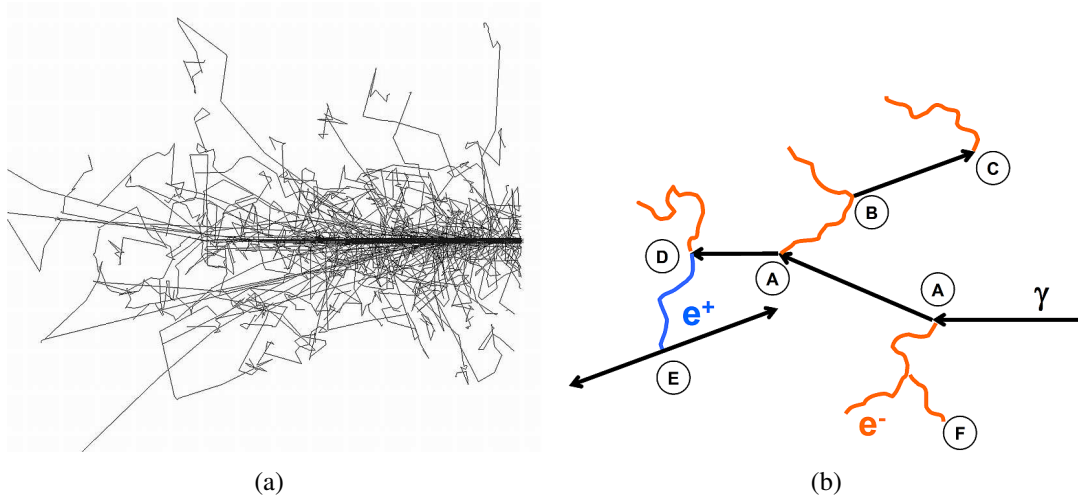


Abbildung A.4.: (a): Mittels Monte-Carlo Simulation berechnete Bahnpuren monenergetischer 10 MeV Photonen. Die Photonen treten in einem dünnen Bündel von rechts auf Wasser. (b): Mögliche Wechselwirkungen von Photonen in einem Teilchenschauer. An den Punkten (A) findet ein Compton-Prozess mit Richtungsänderung des initialen Photons statt und der Generation eines Sekundärelektrons, das wiederum selbst durch Bremsstrahlung an Punkt B ein Photon erzeugen kann, das beim Photo-Effekt absorbiert wird (C). In einer Kaskade von Wechselwirkungen, die das Teilchenschicksal charakterisiert können beispielsweise Paarbildung (D), Positronen-Anihilation (E) oder die Erzeugung von δ -Elektronen stattfinden (F).

te Teilchenschicksal (*history*) oder ein Teilchenschauer (*shower*) ergibt. In Abbildung A.4(a) ist das Ergebnis einer Monte-Carlo Simulation für ein Bündel von Photonen gezeigt, die in Wasser wechselwirken. In Abbildung A.4(b) ist schematisch ein mögliches Teilchenschicksal für eines der primären Photonen dargestellt. Teilchen werden als Folge von Wechselwirkungen “geboren“ und “sterben“, wenn ihre kinetische Energie unter eine definierte Grenze fällt oder wenn sie die Simulationsgeometrie verlassen.

Für eine große Anzahl individueller, unabhängiger Primär-Teilchenschicksale N lassen sich makroskopische Größen Q , wie beispielsweise die absorbierte Energiedosis aus der Simulation als Mittelwert berechnen. Formal lässt sich Q als Integral darstellen mit

$$Q = \int qp(q)dq \quad (\text{A.18})$$

mit der üblicherweise unbekanntenen PDF $p(q)$ (Salvat et al., 2006). Die Simulation einzelner Teilchenschicksale dient dabei als Methode zufällige Werte q_i zu erhalten, die der Wahrscheinlichkeitsverteilung $p(q)$ entstammen. Die Wahrscheinlichkeitsverteilung $p(q)$ ist in diesem Fall als die Kaskade vieler zufälliger Prozesse zu verstehen, die jeweils eigene PDF's wie z.B. für die Richtungsänderung aufweisen. Entsprechend Gleichung A.6

liefert die Monte-Carlo Integration eine Lösung des Integrals Q

$$\bar{Q} = \frac{1}{N} \sum_i^N q_i \quad (\text{A.19})$$

mit einer Standardabweichung entsprechend Gleichung A.7. Dabei ist die Größe Q beispielsweise die absorbierte Dosis in einem Volumenelement, die sich durch alle Energieüberträge im Teilchenschicksal i ergibt. Durch den gekoppelten Transport von Teilchen wie Photonen und Elektronen, kann sich bei einem gestarteten primären Photon die Energiedeposition aus vielen Teilchen höherer Generationen zusammensetzen, eine Tatsache, die eine analytische Beschreibung des Teilchentransports schwierig gestaltet. Neben messtechnisch prinzipiell zugänglichen Größen, wie z.B. die absorbierte Dosis, lassen sich in einer Monte-Carlo Simulation aber auch eher abstrakte Eigenschaften im Strahlungsfeld untersuchen. So kann beispielsweise die Frage beantwortet werden, wie groß der Anteil der Dosis in einem Volumen durch Bremsstrahlungs-Photonen ist, die in einer definierten Region entstanden sind. Für die Simulation von Strahlungstransport ist vor allem das erwähnte central-limit theorem entscheidend, denn unabhängig von der Komplexität des Gesamtproblems und der Wahrscheinlichkeitsverteilungen einzelner Prozesse, lässt sich das Ergebnis als Mittelwert mit einer Standardabweichung auffassen.

Modellierung eines Teilchenwegs

Die Simulation eines ganzen Teilchenschicksals erfolgt sequentiell, so dass jedes Ergebnis der einzelnen Wechselwirkung, wie in Abbildung A.4(b) dargestellt, und der Weg eines Teilchens zum Ort der Wechselwirkung ermittelt werden muss.

Freie Weglänge

Das Konzept des totalen Streuquerschnitts σ definiert den Anteil aller gestreuten Teilchen in einem Streuexperiment. Üblicherweise können im Medium konkurrierende Wechselwirkungen stattfinden, so dass sich beispielsweise bei zwei möglichen Streuprozessen A und B der totale Streuquerschnitt als Summe $\sigma = \sigma_A + \sigma_B$ ergibt. Die totalen Streuquerschnitte lassen sich aus den differentiellen Streuquerschnitten für ein Teilchen der Energie E

$$\frac{d^2\sigma(E; \theta, W)}{d\Omega dW} \quad (\text{A.20})$$

durch Integration über den Raumwinkel Ω und den Energieverlust W bestimmen. Der makroskopische Streuquerschnitt Σ ergibt sich aus $\Sigma = N\sigma$ wobei

$$N = N_A \frac{\rho}{A_M} \quad (\text{A.21})$$

mit der Avogadro-Konstante N_A , der Dichte ρ des Mediums und der Massenzahl A_M die Anzahl der Moleküle je Volumen im Medium darstellt. Im Fall einer Mischung sind ρ , A_M sowie σ als gewichtetes Mittel aus den Anteilen der jeweiligen atomaren Bestand-

teile zu verstehen.

Für ein Teilchen, das sich innerhalb eines solchen Mediums bewegt, lässt sich die Wahrscheinlichkeit $p_s(s)$ einführen, die Strecke s ohne eine Wechselwirkung zurückgelegt zu haben. Dies entspricht also der Wahrscheinlichkeit für das “Überleben“ des Teilchens. Entlang des Weges ändert sich $p_s(s)$ mit

$$dp_s(s) = -p_s(s)\Sigma ds \quad (\text{A.22})$$

wobei das negative Vorzeichen auf der rechten Seite die Abnahme der Wahrscheinlichkeit für das Teilchen widerspiegelt, noch keine Wechselwirkung erfahren zu haben. Mit $p_s(0) = 1$ und einem über den Weg hin konstanten Streuquerschnitt Σ , lässt sich Gleichung A.22 umformen nach

$$p_s(s) = e^{-\Sigma s} \quad (\text{A.23})$$

was dem bekannten, exponentiellen Schwächungsgesetz entspricht. Die Wahrscheinlichkeit, dass das Teilchen innerhalb der Strecke s eine Wechselwirkung erfahren hat, ergibt sich einfach aus $1 - p_s(s)$. Damit lässt sich die PDF $p(s)$ für eine Wechselwirkung *exakt* nach der Strecke s aus der Ableitung $1 - p_s(s)$ nach s bestimmen

$$p(s) = \frac{d}{ds} [1 - p_s(s)] = \Sigma e^{-\Sigma s} \quad (\text{A.24})$$

Die mittlere freie Weglänge λ (*mean free pathlength*) eines Teilchens ergibt sich nach

$$\lambda = \langle s \rangle = \int_0^\infty s \cdot p_s(s) ds = \frac{1}{\Sigma} \quad (\text{A.25})$$

Werden nun Zufallszahlen entsprechend $p(s)$ ermittelt und λ als bekannter Materialparameter vorausgesetzt, so lassen sich zufällig Orte eines Streuereignisses für ein Teilchen mit der Energie E ermitteln (siehe Abschnitt A).

Streumodell

Wie im vorigen Abschnitt beschrieben, können im Medium meist verschiedene Wechselwirkungsprozesse stattfinden. Am Ort der Wechselwirkung lässt sich die Wahrscheinlichkeit für das Auftreten einer Wechselwirkung A oder B aus den totalen Streuquerschnitten mit $p_A = \sigma_A/\sigma_T$ und $p_B = \sigma_B/\sigma_T = 1 - p_A$ bestimmen. Mit einer gleichverteilten Zufallszahl ξ [0,1] kann so zwischen den zwei Prozessen gewählt werden.

Einzelne Energieverluste W oder Streuwinkel θ für Wechselwirkungsprozess A oder B bei der Energie E lassen sich aus dem totalen Streuquerschnitt mit Hilfe einer entsprechenden PDF ermitteln für die gilt

$$p_{A,B}(E; \theta, W) = \frac{2\pi \sin\theta}{\sigma_{A,B}(E)} \frac{d^2\sigma_{A,B}(E; \theta, W)}{d\Omega dW} \quad (\text{A.26})$$

Man beachte, dass in obiger Gleichung der Winkel θ den polaren Winkel bezeichnet, wodurch der Faktor $2\pi \sin\theta$ eingeführt wird. Die Streuung um die Flugrichtung des Teilchens ist stets rotationssymmetrisch, so dass für den Winkel ϕ eine Gleichverteilung

vorliegt und für die entsprechende PDF

$$p(\phi) = \frac{1}{2\pi} \quad (\text{A.27})$$

verwendet werden kann. Nach dem Streueignis wird erneut der Weg zum nächsten Wechselwirkungsort ermittelt werden, wie im vorigen Abschnitt beschrieben. Zuvor müssen allerdings die resultierende Energieänderung noch berücksichtigt sowie mögliche Richtungsänderung durch Koordinatentransformationen durchgeführt werden. Mit Hilfe der sampling-Techniken beschrieben, Zufallszahlen und vor allem den differentiellen Streuquerschnitten, lässt sich das Schicksal eines Teilchens im Medium also simulieren. Neu entstandene Teilchen werden entsprechend behandelt, eine ganze Kaskade von Teilchen wird als dynamischer *particle-stack* sequentiell abgearbeitet.

Der Transport eines einzelnen Teilchens wird fortgesetzt, bis es absorbiert wird (z.B. ein Photon beim Photoeffekt), die Simulationsgeometrie verlassen hat oder unter eine definierte Energiegrenze fällt. Unterhalb dieser mehr oder weniger willkürlichen Schwelle wird die restliche kinetische Energie der Teilchen als lokal absorbiert angenommen. Die zunehmende Wahrscheinlichkeit für Wechselwirkungen mit kleineren Energien erfordert einen hohen Simulationsaufwand, der letztlich bei einer endlichen Größe der Berechnungsgeometrie keinen Informationsgewinn bedeutet. Beispielsweise liegt für ein Elektron von 10 keV die Restreichweite in Wasser bei maximal 10^{-4} cm. Für die übliche Größe eines Volumenelements in einem kartesischen Gitter von 1-5 mm Kantenlänge spielt es also keine Rolle, wo genau die Dosisdeposition im Volumenelement stattfindet, so dass der Transport bei höheren Energien beendet werden kann¹. Die Wahl dieser Grenzenergien ist also problemspezifisch.

Besonderheit bei der Simulation geladener Teilchen

Das oben beschriebene Schema ist bei der Simulation von geladenen Teilchen aufgrund der großen Zahl von Wechselwirkungen, bei denen im Mittel nur wenige 10 eV Energie übertragen wird, in den meisten Fragestellungen nicht praktikabel². Berger (1963) hat bereits 1963 zwei mögliche Lösungen des Problems für Elektronen mit der sogenannten *condensed-history* (CH) Technik vorgeschlagen. Beiden Ansätzen gemein ist die Idee, viele Wechselwirkungen eines geladenen Teilchens, mit kleinen Änderungen in Energie und Richtung, zu einem Elektronenschritt zusammenzufassen. Dieser künstliche Schritt beinhaltet unter der Verwendung einer entsprechenden Beschreibung der Vielfachstreuung die gesamte Winkel-, Energie- und Positionsänderung (siehe Abb. A.5(a)).

Im CH Klasse II Ansatz, der beispielsweise im EGS-Code Verwendung findet, werden mehrere elastische und inelastische Streueignisse zusammengefasst, während oberhalb einer definierten Energiegrenze katastrophale Wechselwirkungen (Erzeugung von Bremsstrahlung und δ -Elektronen) explizit modelliert werden. Die Unterscheidung in harte und weiche Stößen bzw. Wechselwirkungen ist dabei mehr oder weniger willkürlich, bestimmt jedoch sowohl die Genauigkeit des Ergebnisses als auch die Geschwin-

¹Weiterhin sind die zu Grunde liegenden Streuquerschnitte bzw. die Beschreibung des Teilchentransports lediglich bis zu einer gewissen Grenzenergie gültig.

²Eine Ausnahme stellen Algorithmen zur Simulation auf Nanometer-Ebene dar.

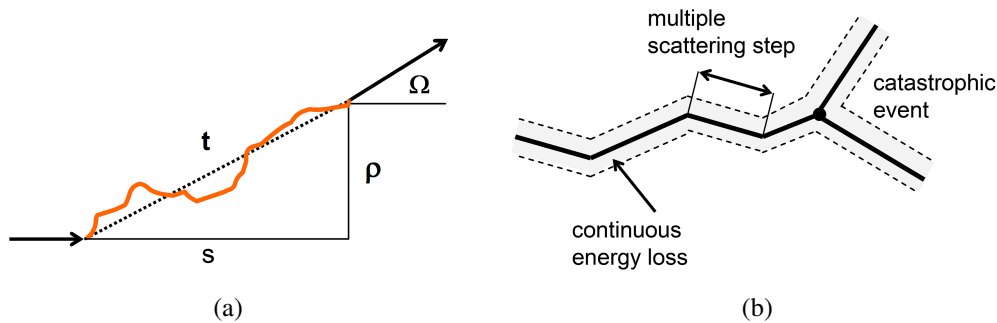


Abbildung A.5.: Grundidee *condensed history*. (a): Der Weg eines geladenen Teilchens durch das Medium wird in geraden Schritten vorgenommen, die jeweils mehrere Streuereignisse mit kleinen Winkel- und kleinen bzw. keinen Energieänderungen zusammenfassen (multiple scattering). Die Weglänge t und der Winkel Ω am Ende des Schritts werden aus einer entsprechenden Verteilung ermittelt. Die laterale Verschiebung ρ und die longitudinale Änderung des geraden Schritts gegenüber der gekrümmten Bahn müssen dabei korrigiert werden. (b): Klasse II Algorithmus. Der kontinuierliche Energieverlust unterhalb einer definierten Energieschwelle umfasst die Energieabgabe in unmittelbarer Umgebung der Teilchenbahn einzelner CH Schritte (grauer Bereich). Am Ort einer diskreten, katastrophalen Wechselwirkung oberhalb der Grenzenenergie entsteht ein Sekundärteilchen.

digkeit der Simulation. Die Energiedeposition auf dem Weg zwischen zwei harten Stößen wird kontinuierlich mit Hilfe der beschränkten Bremsvermögen L in einer CSDA-Näherung (continuous-slowing-down-approximation) ermittelt, beschränkt auf Depositionen kleiner der definierten Energiegrenze (siehe Abb. A.5(b)). Allerdings muss dabei berücksichtigt werden, dass $L(E)$ als Funktion der Energie nicht konstant ist und sich somit über den Weg ändert.

Im Grunde wird ein CH Schritt durch den Weg zur nächsten diskreten Wechselwirkung bestimmt. Dieser Weg ergibt sich letztlich auch aus einer Verteilung des Energieverlusts zum katastrophalen Streuereignis. Allerdings stellen sowohl geometrische Grenzen als auch die Anwendbarkeit der Vielfachstreu-Modelle eine Beschränkung dar, die die Schrittweite eines geladenen Teilchens limitieren. Für die Gültigkeit der Vielfachstreu-Theorie nach Molière sind beispielsweise eine Mindestanzahl an Streuereignissen nötig, gleichzeitig gilt die Theorie nur für kleine Winkel. Daher mussten für die modernen Monte-Carlo codes entsprechende Vielfachstreu-Modelle entwickelt werden (Kawrakow, 2000b; Salvat et al., 2006).

Der künstliche Schritt entlang einer Geraden berücksichtigt nicht die möglichen gekrümmten Wege eines Elektrons über die Grenzfläche hinaus in ein anderes Medium und der damit verbundenen Veränderung der Trajektorie. Besonders dramatisch wirkt sich dieser Effekt bei Materialien unterschiedlicher Dichte aus, wie z.B. an der Grenzfläche zu Luft. Die Wahl einer maximalen Schrittweite ist daher ein kritischer Parameter für ei-

ne artefaktfreie Simulation. Im EGSnrc (Kawrakow, 2000*b*) System wird in der Nähe zu Grenzflächen daher die condensed history Simulation durch die analoge Beschreibung des Elektronentransports abgelöst.

Bibliography

- Aird, E. G. and Farmer, F. T. (1972), 'The design of a thimble chamber for the Farmer dosimeter.', *Phys. Med. Biol.* **17**(2), 169–174.
- Alfonso, R., Andreo, P., Capote, R., Huq, M. S., Kilby, W., Kjäll, P., Mackie, T. R., Palmans, H., Rosser, K., Seuntjens, J., Ullrich, W. and Vatnitsky, S. (2008), 'A new formalism for reference dosimetry of small and nonstandard fields.', *Med. Phys.* **35**(11), 5179–5186.
- Almond, P. R., Biggs, P. J., Coursey, B. M., Hanson, W. F., Huq, M. S., Nath, R. and Rogers, D. W. O. (1999), 'AAPM's TG-51 protocol for clinical reference dosimetry of high-energy photon and electron beams.', *Med. Phys.* **26**, 1847–1870.
- Almond, P. R. and Svensson, H. (1977), 'Ionization Chamber Dosimetry for Photon and Electron Beams.', *Acta Radiol. Ther. Phys. Biol.* **16**, 177 – 186.
- Andreo, P. (1993), Improved calculations of stopping-power ratios and their correlation with the quality of therapeutic beams., in IAEA, ed., 'Measurement Assurance in Dosimetry (Proc. Symp. Vienna)', Vienna, pp. 335–359.
- Andreo, P. (2000), 'A comparison between calculated and experimental kQ photon beam quality correction factors.', *Phys. Med. Biol.* **45**(9), L25–L38.
- Andreo, P., Burns, D. T., Hohlfield, K., Huq, M., Kanai, T., Laitano, F., Smyth, V. and Vynckier, S. (2001), 'TRS-398: Absorbed Dose Determination in External Beam Radiotherapy: An International Code of Practice for Dosimetry based on Standards of Absorbed Dose to Water.', *International Atomic Energy Agency* .
- Attix, F. H. (2004), *Introduction to Radiological Physics and Radiation Dosimetry*, New York: Wiley-VCH.
- Berger, M., Coursey, J., Zucker, M. and Chang, J. (1998), *Stopping-Power and Range Tables for Electrons, Protons, and Helium Ions (online)*, NIST Standard Reference Database 124.
URL: <http://physics.nist.gov/PhysRefData/Star/Text/contents.html>
- Berger, M., Hubbell, J., Seltzer, S., Chang, J., Coursey, J., Sukumar, R. and Zucker, D. (1999), *XCOM: Photon Cross Sections Database (online)*, NIST Standard Reference Database 8 (XGAM).
URL: <http://physics.nist.gov/PhysRefData/Xcom/Text/XCOM.html>
- Berger, M. J. (1963), Monte Carlo Calculation of the penetration and diffusion of fast charged particles, in B. Alder, S. Fernbach and M. Rotenberg, eds, 'Methods in Comput. Phys.', Academic, New York, pp. 135–215.
- Bichsel, H. and Hiraoka, T. (1992), 'Energy loss of 70 MeV protons in elements.', *Nucl. Instrum. Methods Phys. Res.* **B 66**, 345–351.

- Bielajew, A. F. (2001), *Fundamentals of the Monte Carlo method for neutral and charged particle transport*, The University of Michigan.
- Borg, J., Kawrakow, I., Rogers, D. W. O. and Seuntjens, J. P. (2000), 'Monte Carlo study of correction factors for Spencer-Attix cavity theory at photon energies at or above 100 keV.', *Med. Phys.* **27**, 1804 – 1813.
- Bortfeld, T. (2006), 'IMRT: a review and preview.', *Phys. Med. Biol.* **51**(13), R363–R379.
- Bouchard, H. and Seuntjens, J. (2004), 'Ionization chamber-based reference dosimetry of intensity modulated radiation beams.', *Med. Phys.* **31**(9), 2454–2465.
- Boyer, A. L. and Schultheiss, T. (1988), 'Effects of dosimetric and clinical uncertainty on complication-free local tumor control.', *Radiother Oncol* **11**(1), 65–71.
- Buckley, L. A., Kawrakow, I. and Rogers, D. W. O. (2004), 'CSnrc: correlated sampling Monte Carlo calculations using EGSnrc.', *Med. Phys.* **31**(12), 3425–3435.
- Buckley, L. A. and Rogers, D. W. O. (2006a), 'Wall correction factors, Pwall, for parallel-plate ionization chambers.', *Med. Phys.* **33**(6), 1788–1796.
- Buckley, L. A. and Rogers, D. W. O. (2006b), 'Wall correction factors, Pwall, for thimble ionization chambers.', *Med. Phys.* **33**(2), 455–464.
- Capote, R., Sánchez-Doblado, F., Leal, A., Lagares, J. I., Arráns, R. and Hartmann, G. H. (2004), 'An EGSnrc Monte Carlo study of the microionization chamber for reference dosimetry of narrow irregular IMRT beamlets.', *Med. Phys.* **31**(9), 2416–2422.
- Chetty, I. J., Curran, B., Cygler, J. E., DeMarco, J., Ezzell, G., Faddegon, B. A., Kawrakow, I., Keall, P. J., Liu, H., Ma, C. M., Rogers, D. W. O., Seuntjens, J., Sheikh-Bagheri, D. and Siebers, J. V. (2007), 'Report of the AAPM Task Group No. 105: issues associated with clinical implementation of Monte Carlo-based photon and electron external beam treatment planning.', *Med. Phys.* **34**(12), 4818–4853.
- Chibani, O. and Ma, C. M. (2007), 'On the discrepancies between Monte Carlo dose calculations and measurements for the 18 MV varian photon beam.', *Med. Phys.* **34**(4), 1206–1216.
- Chibani, O. and Williamson, J. F. (2005), 'MCPI: a sub-minute Monte Carlo dose calculation engine for prostate implants.', *Med. Phys.* **32**(12), 3688–3698.
- Cunningham, J. R. and Sontag, M. R. (1980), 'Displacement corrections used in absorbed dose determination.', *Med. Phys.* **7**(6), 672–676.
- Das, I. J., Ding, G. X. and Ahnesjö, A. (2008a), 'Small fields: nonequilibrium radiation dosimetry.', *Med. Phys.* **35**(1), 206–215.

- Das, I. J., W., C., Cheng, Watts, R. J., Ahnesjö, A., Gibbons, J., Li, X. A., Lowenstein, J., Mitra, R. K., Simon, W. E. and Zhu, T. C. (2008b), 'Accelerator beam data commissioning equipment and procedures: report of the TG-106 of the Therapy Physics Committee of the AAPM.', *Med. Phys.* **35**(9), 4186–4215.
- de Buffon, G. C. (1777), 'Essai darithm etique morale', *Supplement a l'Histoire Naturelle* **4**.
- de Carlan, L., Price, R., Chartier, J., Kodeli, I., Siebert, B., Henninger, J., Posselt, J., Gualdrini, G., Agosteo, S., Bedogni, R., Bordy, J., Cassette, P., Ferrari, P., Ros, J. G., Großwendt, B., Lacoste, V., Pola, A., Rollet, S., Schultz, F., Simakov, S. P., Tanner, R., Terrissol, M. and Zankl, M. (2008), 'Analysis of computational problems expressing the overall uncertainties: photons, neutrons and electrons.', *Radiat. Prot. Dos.* **131**(1), 15–23.
- DIN-EN-10088-1 (2005), 'Nichtrostende Stähle Teil 1: Verzeichnis der nichtrostenden Stähle Deutsche Fassung EN 100881:2005.', *DIN Deutsches Institut für Normung e.V.*
- DIN6800-2 (2008), 'Dosismessverfahren nach der Sondenmethode für Photonen- und Elektronenstrahlung - Teil 2: Dosimetrie hochenergetischer Photonen- und Elektronenstrahlung mit Ionisationskammern.', *DIN Deutsches Institut für Normung e.V.*
- Ding, G. X., Duggan, D. M. and Coffey, C. W. (2006), 'Commissioning stereotactic radiosurgery beams using both experimental and theoretical methods.', *Phys. Med. Biol.* **51**(10), 2549–2566.
- Ding, G. X., Duggan, D. M. and Coffey, C. W. (2008), 'A theoretical approach for non-equilibrium radiation dosimetry.', *Phys. Med. Biol.* **53**(13), 3493–3499.
- Ding, G. X., Rogers, D. W. and Mackie, T. R. (1995), 'Calculation of stopping-power ratios using realistic clinical electron beams.', *Med. Phys.* **22**(5), 489–501.
- Dohm, O. S., Fippel, M., Christ, G. and Nüsslin, F. (2005), 'Off-axis chamber response in the depth of photon dose maximum.', *Phys. Med. Biol.* **50**(7), 1449–1457.
- Eckhardt, R. (1987), 'Stan Ulam, John von Neumann, and the Monte Carlo Method', *Los Alamos Science - Special Issue* pp. 131–137.
- Faddegon, B. A., Asai, M., Perl, J., Ross, C., Sempau, J., Tinslay, J. and Salvat, F. (2008), 'Benchmarking of Monte Carlo simulation of bremsstrahlung from thick targets at radiotherapy energies.', *Med. Phys.* **35**, 4308–4317.
- Faddegon, B. A., Egley, B. and Steinberg, T. (2004), 'Comparison of beam characteristics of a gold x-ray target and a tungsten replacement target.', *Med. Phys.* **31**(1), 91–97.
- Faddegon, B. A., O'Brien, P. and Mason, D. L. (1999), 'The flatness of Siemens linear accelerator x-ray fields.', *Med. Phys.* **26**(2), 220–228.

- Fano, U. (1954), 'Note on the Bragg-Gray cavity principle for measuring energy dissipation.', *Radiat. Res.* **1**(3), 237–240.
- Fogliata, A., Vanetti, E., Albers, D., Brink, C., Clivio, A., Knöös, T., Nicolini, G. and Cozzi, L. (2007), 'On the dosimetric behaviour of photon dose calculation algorithms in the presence of simple geometric heterogeneities: comparison with Monte Carlo calculations.', *Phys. Med. Biol.* **52**(5), 1363–1385.
- Francescon, P., Cavedon, C., Reccanello, S. and Cora, S. (2000), 'Photon dose calculation of a three-dimensional treatment planning system compared to the Monte Carlo code BEAM.', *Med. Phys.* **27**(7), 1579–1587.
- Gillin, M. T., Kline, R. W., Niroomand-Rad, A. and Grimm, D. F. (1985), 'The effect of thickness of the waterproofing sheath on the calibration of photon and electron beams.', *Med. Phys.* **12**(2), 234–236.
- Gonzales-Castano, D., Pena, J., Sanchez-Doblado, F., Hartmann, G. H., Gomez, F. and Leal, A. (2007), 'The change of response of ionization chambers in the penumbra and transmission regions: impact for IMRT verifications.', *Med. Bio. Eng. Comput.* .
- Hanson, W. F. and Tinoco, J. A. (1985), 'Effects of plastic protective caps on the calibration of therapy beams in water.', *Med. Phys.* **12**(2), 243–248.
- Henkner, K. and Jäkel, O. (2007), Monte Carlo depth-dose calculations for different I-values in heavy ion therapy., in J. Debus, K. Henrichs and G. Kraft, eds, '11th Workshop of Heavy Charged Particles in Biology and Medicine', pp. 37–38.
- Heydarian, M., Hoban, P. W. and Beddoe, A. H. (1996), 'A comparison of dosimetry techniques in stereotactic radiosurgery.', *Phys. Med. Biol.* **41**(1), 93–110.
- Hubbell, J. H. (2006), 'Review and history of photon cross section calculations.', *Phys. Med. Biol.* **51**, R245–R262.
- Huq, M. S., Andreo, P. and Song, H. (2001), 'Comparison of the IAEA TRS-398 and AAPM TG-51 absorbed dose to water protocols in the dosimetry of high-energy photon and electron beams.', *Phys. Med. Biol.* **46**(11), 2985–3006.
- Huq, M. S., Das, I. J., Steinberg, T. and Galvin, J. M. (2002), 'A dosimetric comparison of various multileaf collimators.', *Phys Med Biol* **47**(12), N159–N170.
- IAEA (2004), 'Commissioning and Quality Assurance of Computerized Planning Systems for Radiation Treatment of Cancer', *TECHNICAL REPORTS SERIES No. 430* .
- ICRU (1984), *Stopping powers for electrons and positrons, ICRU Report 37.*, Washington DC: ICRU.
- ISO (1995), *Guide to the Expression of Uncertainty in Measurement.*, Geneva: International Organization for Standardization (ISO).

- Johansson, K. A., Mattson, L. O., Lindborg, L. and Svensson, H. (1977), Absorbed-dose determination with ionization chambers in electron and photon beams having energies between 1 and 50 MeV., in 'IAEA Symposium Proceedings', IAEA-SM-222/35, pp. 243–270.
- Kalach, N. I. and Rogers, D. W. O. (2003), 'Which accelerator photon beams are "clinic-like" for reference dosimetry purposes?', *Med. Phys.* **30**(7), 1546–1555.
- Kalos, M. H. and Whitlock, P. A. (2004), *Monte Carlo Methods*, Weinheim: Wiley VCH.
- Kawrakow, I. (2000a), 'Accurate condensed history Monte Carlo simulation of electron transport. I. EGSnrc, the new EGS4 version.', *Med. Phys.* **27**(3), 485–498.
- Kawrakow, I. (2000b), 'Accurate condensed history Monte Carlo simulation of electron transport. II. Application to ion chamber response simulations.', *Med. Phys.* **27**(3), 499–513.
- Kawrakow, I. (2005), 'On the efficiency of photon beam treatment head simulations.', *Med. Phys.* **32**(7), 2320–2326.
- Kawrakow, I. (2006a), 'EGSnrc C++ class library; Report PIRS-898.', *National Research Council of Canada* .
- Kawrakow, I. (2006b), 'On the effective point of measurement in megavoltage photon beams.', *Med. Phys.* **33**(6), 1829–1839.
- Kawrakow, I. and Fippel, M. (2000), 'Investigation of variance reduction techniques for Monte Carlo photon dose calculation using XVMC.', *Phys. Med. Biol.* **45**(8), 2163–2183.
- Kawrakow, I. and Rogers, D. W. O. (2006), 'The EGSnrc Code System: Monte Carlo Simulation of Electron and Photon Transport; NRCC Report PIRS-701.', *National Research Council of Canada* .
- Kawrakow, I., Rogers, D. W. O. and Walters, B. R. B. (2004), 'Large efficiency improvements in BEAMnrc using directional bremsstrahlung splitting.', *Med. Phys.* **31**, 2883–2898.
- Kawrakow, I. and Walters, B. R. B. (2006), 'Efficient photon beam dose calculations using DOSXYZnrc with BEAMnrc.', *Med. Phys.* **33**(8), 3046–3056.
- Loevinger, R. (1981), 'A formalism for calculation of absorbed dose to a medium from photon and electron beams.', *Med. Phys.* **8**(1), 1–12.
- Ma, C. M. and Jiang, S. B. (1999), 'Monte Carlo modelling of electron beams from medical accelerators', *Phys. Med. Biol.* **44**, R157–R189.
- Ma, C. M. and Nahum, A. E. (1993a), 'Calculation of absorbed dose ratios using correlated Monte Carlo sampling.', *Med. Phys.* **20**(4), 1189–1199.

- Ma, C. M. and Nahum, A. E. (1993*b*), 'Effect of size and composition of the central electrode on the response of cylindrical ionization chambers in high-energy photon and electron beams.', *Phys. Med. Biol.* **38**, 267–290.
- Ma, C. M. and Nahum, A. E. (1995), 'Monte Carlo calculated stem effect correction for NE2561 and NE2571 chambers in medium-energy x-ray beams.', *Phys. Med. Biol.* **40**(1), 63–72.
- Mackie, T. R. (2006), 'History of tomotherapy.', *Phys. Med. Biol.* **51**(13), R427–R453.
- Mainegra-Hing, E., Kawrakow, I. and Rogers, D. W. O. (2003), 'Calculations for plane-parallel ion chambers in ⁶⁰Co beams using the EGSnrc Monte Carlo code.', *Med. Phys.* **30**(2), 179–189.
- Marsaglia, G., Zaman, A. and Tsang, W. W. (1990), 'Toward a universal random number generator', *Statistics and Probability Letters* **8**, 35–39.
- Martens, C., Wagter, C. D. and Neve, W. D. (2000), 'The value of the PinPoint ion chamber for characterization of small field segments used in intensity-modulated radiotherapy.', *Phys. Med. Biol.* **45**(9), 2519–2530.
- McCaffrey, J. P., Mainegra-Hing, E., Kawrakow, I., Shortt, K. R. and Rogers, D. W. O. (2004), 'Evidence for using Monte Carlo calculated wall attenuation and scatter correction factors for three styles of graphite-walled ion chambers.', *Phys. Med. Biol.* **49**, 2491 – 2501.
- McEwen, M. R., Kawrakow, I. and Ross, C. K. (2008), 'The effective point of measurement of ionization chambers and the build-up anomaly in MV x-ray beams.', *Med. Phys.* **35**(3), 950–958.
- McKerracher, C. and Thwaites, D. I. (2006), 'Notes on the construction of solid-state detectors.', *Radiother. Oncol.* **79**(3), 348–351.
- Mohan, R., Chui, C. and Lidofsky, L. (1985), 'Energy and angular distributions of photons from medical linear accelerators.', *Med. Phys.* **12**(5), 592–597.
- Mora, G. M., Maio, A. and Rogers, D. W. O. (1999), 'Monte Carlo simulation of a typical ⁶⁰Co therapy source.', *Med. Phys.* **26**(11), 2494–2502.
- Nahum, A. E. (1978), 'Water/air mass stopping power ratios for megavoltage photon and electron beams.', *Phys. Med. Biol.* **23**(1), 24–38.
- Nahum, A. E. (1988), Simulation of Dosimeter Response and Interface Effects., in T. M. Jenkins, W. R. Nelson, A. Rindi, A. E. Nahum and D. W. O. Rogers, eds, 'Monte Carlo Transport of Electrons and Photons', Plenum Press, New York, pp. 523–547.
- Nahum, A. E. (1996), 'Perturbation effects in dosimetry: Part I. Kilovoltage x-rays and electrons.', *Phys. Med. Biol.* **41**(9), 1531–1580.

- Neuenschwander, H., Mackie, T. R. and Reckwerdt, P. J. (1995), 'MMC—a high-performance Monte Carlo code for electron beam treatment planning.', *Phys. Med. Biol.* **40**(4), 543–574.
- Paelinck, L., Reynaert, N., Thierens, H., Wagter, C. D. and Neve, W. D. (2003), 'The value of radiochromic film dosimetry around air cavities: experimental results and Monte Carlo simulations.', *Phys. Med. Biol.* **48**(13), 1895–1905.
- Palm, A. and Mattsson, O. (1999), 'Experimental study on the influence of the central electrode in Farmer-type ionization chambers.', *Phys. Med. Biol.* **44**(5), 1299–1308.
- Papanikolaou, N., Battista, J. J., Boyer, A. L., Kappas, C., Klein, E., Mackie, T. R., Sharpe, M. and Dyk, J. V. (2004), *TISSUE INHOMOGENEITY CORRECTIONS FOR MEGAVOLTAGE PHOTON BEAMS: Report of AAPM Task Group No.65*, Madison, USA: Medical Physics Publishing.
- Paskalev, K. A., Seuntjens, J. P., Patrocinio, H. J. and Podgorsak, E. B. (2003), 'Physical aspects of dynamic stereotactic radiosurgery with very small photon beams (1.5 and 3 mm in diameter).', *Med. Phys.* **30**(2), 111–118.
- Paul, H. (2007), 'The mean ionization potential of water, and its connection to the range of energetic carbon ions in water', *Nuc. Instr. and Meth. B* **255**, 435–437.
- Pena, J., González-Castaño, D. M., Gómez, F., Sánchez-Doblado, F. and Hartmann, G. H. (2007), 'Automatic determination of primary electron beam parameters in Monte Carlo simulation.', *Med. Phys.* **34**(3), 1076–1084.
- Pena, J., Sánchez-Doblado, F., Capote, R., Terrón, J. A. and Gómez, F. (2006), 'Monte Carlo correction factors for a Farmer 0.6 cm³ ion chamber dose measurement in the build-up region of the 6 MV clinical beam.', *Phys. Med. Biol.* **51**(6), 1523–1532.
- Podgorsak, E. B. (2006), *Radiation Physics for Medical Physicists*, Berlin, Heidelberg: Springer.
- Poon, E., Seuntjens, J. and Verhaegen, F. (2005), 'Consistency test of the electron transport algorithm in the GEANT4 Monte Carlo code.', *Phys. Med. Biol.* **50**(4), 681–694.
- Reich, H. (1990), *Dosimetrie ionisierender Strahlung.*, Stuttgart: B. G. Teubner.
- Rogers, D. W. O. (1993), 'How accurately can EGS4/PRESTA calculate ion-chamber response?', *Med. Phys.* **20**(2 Pt 1), 319–323.
- Rogers, D. W. O. (2006), 'Fifty years of Monte Carlo simulations for medical physics.', *Phys. Med. Biol.* **51**(13), R287–R301.
- Rogers, D. W. O. and Bielajew, A. F. (1990), Monte Carlo Techniques of Electron and Photon Transport for Radiation Dosimetry (Chapter 5), in K. R. Kase, B. E. Bjärngard and F. H. Attix, eds, 'The Dosimetry of Ionizing Radiation', Academic Press, pp. 427–539.

- Rogers, D. W. O., Ewart, G. M., Bielajew, A. F. and van Dyk, G. (1988), Calculation of Electron Contamination in a ^{60}Co Therapy Beam., in J. P. Seuntjens and P. Mobit, eds, 'Proceedings of the IAEA International Symposium on Dosimetry in Radiotherapy', p. 25 – 312.
- Rogers, D. W. O., Faddegon, B. A., Ding, G. X., Ma, C. M., We, J. and Mackie, T. R. (1995), 'BEAM: a Monte Carlo code to simulate radiotherapy treatment units.', *Med. Phys.* **22**(5), 503–524.
- Rogers, D. W. O. and Kawrakow, I. (2003), 'Monte Carlo calculated correction factors for primary standards of air kerma.', *Med. Phys.* **30**(4), 521–532.
- Rogers, D. W. O., Kawrakow, I., Seuntjens, J. P., Walters, B. R. B. and Mainegra-Hing, E. (2005), 'NRC User Codes for EGSnrc; NRCC Report PIRS-702(revB).', *National Research Council of Canada* .
- Rogers, D. W. O., Walters, B. R. B. and Kawrakow, I. (2006), 'BEAMnrc Users Manual PIRS-0509(A)revK.', *National Research Council of Canada* .
- Russa, D. J. L., McEwen, M. and Rogers, D. W. O. (2007), 'An experimental and computational investigation of the standard temperature-pressure correction factor for ion chambers in kilovoltage x rays.', *Med. Phys.* **34**(12), 4690–4699.
- Russa, D. J. L. and Rogers, D. W. O. (2008), 'Accuracy of EGSnrc calculations at [sup 60]Co energies for the response of ion chambers configured with various wall materials and cavity dimensions.', *Med. Phys.* **35**(12), 5629–5640.
- Salvat, F., Fernandez-Varea, J. M. and Sempau, J. (2006), *PENELOPE-2006: A Code System for Monte Carlo Simulation of Electron and Photon Transport*, France: OECD Nuclear Energy Agency.
- Sánchez-Doblado, F., Andreo, P., Capote, R., Leal, A., Perucha, M., Arráns, R., Núñez, L., Mainegra, E., Lagares, J. I. and Carrasco, E. (2003), 'Ionization chamber dosimetry of small photon fields: a Monte Carlo study on stopping-power ratios for radiosurgery and IMRT beams.', *Phys. Med. Biol.* **48**(14), 2081–2099.
- Sánchez-Doblado, F., Hartmann, G. H., Pena, J., Capote, R., Paiusco, M., Rhein, B., Leal, A. and Lagares, J. I. (2007), 'Uncertainty estimation in intensity-modulated radiotherapy absolute dosimetry verification.', *Int J Radiat Oncol Biol Phys* **68**(1), 301–310.
- Sauer, O. A. and Wilbert, J. (2007), 'Measurement of output factors for small photon beams.', *Med. Phys.* **34**(6), 1983–1988.
- Sawkey, D. L. and Faddegon, B. A. (2009), 'Determination of electron energy, spectral width, and beam divergence at the exit window for clinical megavoltage x-ray beams.', *Med. Phys.* **36**(3), 698–707.

- Schmidt, R., Wulff, J., Kästner, B., Jany, D., Heverhagen, J. T., Fiebich, M. and Zink, K. (2009), Monte Carlo based calculation of patient exposure in X-ray CT-examinations., in '4th European Conference of the International Federation for Medical and Biological Engineering', pp. 2487–2490.
- Schreiber, E. C. and Faddegon, B. A. (2005), 'Sensitivity of large-field electron beams to variations in a Monte Carlo accelerator model.', *Phys. Med. Biol.* **50**(5), 769–778.
- Scott, A. J. D., Nahum, A. E. and Fenwick, J. D. (2008), 'Using a Monte Carlo model to predict dosimetric properties of small radiotherapy photon fields', *Med. Phys.* **35**, 4671–4684.
- Selvam, T. P., Saull, P. R. B. and Rogers, D. W. O. (2005), 'Monte Carlo modelling of the response of NRC's $^{90}\text{Sr}/^{90}\text{Y}$ primary beta standard.', *Med. Phys.* **32**, 3084 – 3094.
- Sempau, J. and Andreo, P. (2006), 'Configuration of the electron transport algorithm of PENELOPE to simulate ion chambers.', *Phys. Med. Biol.* **51**(14), 3533–3548.
- Sempau, J., Andreo, P., Aldana, J., Mazurier, J. and Salvat, F. (2004), 'Electron beam quality correction factors for plane-parallel ionization chambers: Monte Carlo calculations using the PENELOPE system.', *Phys. Med. Biol.* **49**(18), 4427–4444.
- Seuntjens, J. P., Kawrakow, I., Borg, J., Hobeila, F. and Rogers, D. W. O. (2002), Calculated and measured air-kerma response of ionization chambers in low and medium energy photon beams., in J. P. Seuntjens and P. Mobit, eds, 'Recent developments in accurate radiation dosimetry, Proc. of an Int'l Workshop', Medical Physics Publishing, Madison WI, pp. 69 – 84.
- Seuntjens, J. and Verhaegen, F. (2003), 'Comments on 'ionization chamber dosimetry of small photon fields: a Monte Carlo study on stopping-power ratios for radiosurgery and IMRT beams''.', *Phys. Med. Biol.* **48**(21), L43–5; author reply L46–8.
- Sham, E., Seuntjens, J., Devic, S. and Podgorsak, E. B. (2008), 'Influence of focal spot on characteristics of very small diameter radiosurgical beams.', *Med. Phys.* **35**(7), 3317–3330.
- Sheikh-Bagheri, D. and Rogers, D. W. O. (2002a), 'Monte Carlo calculation of nine megavoltage photon beam spectra using the BEAM code.', *Med. Phys.* **29**(3), 391–402.
- Sheikh-Bagheri, D. and Rogers, D. W. O. (2002b), 'Sensitivity of megavoltage photon beam Monte Carlo simulations to electron beam and other parameters.', *Med. Phys.* **29**(3), 379–390.
- Smedt, B. D., Reynaert, N., Flachet, F., Coghe, M., Thompson, M. G., Paelinck, L., Pittomvils, G., Wagter, C. D., Neve, W. D. and Thierens, H. (2005), 'Decoupling initial electron beam parameters for Monte Carlo photon beam modelling by removing beam-modifying filters from the beam path.', *Phys. Med. Biol.* **50**(24), 5935–5951.

- Spencer, L. V. and Attix, F. H. (1955a), 'A cavity ionization theory including the effects of energetic secondary electrons.', *Radiology* **64**(1), 113.
- Spencer, L. V. and Attix, F. H. (1955b), 'A theory of cavity ionization.', *Radiat. Res.* **3**(3), 239–254.
- Tantot, L. and Seuntjens, J. (2008), 'Modelling ionization chamber response to nonstandard beam configurations.', *Journal of Physics: Conference Series* **102**.
- Taylor, R. E. P. and Rogers, D. W. O. (2008), 'An EGSnrc Monte Carlo-calculated database of TG-43 parameters.', *Med. Phys.* **35**(9), 4228–4241.
- Tonkopi, E., McEwen, M. R., Walters, B. R. B. and Kawrakow, I. (2005), 'Influence of ion chamber response on in-air profile measurements in megavoltage photon beams.', *Med. Phys.* **32**(9), 2918–2927.
- Tzedakis, A., Damilakis, J. E., Mazonakis, M., Stratakis, J., Varveris, H. and Gourtsoyiannis, N. (2004), 'Influence of initial electron beam parameters on Monte Carlo calculated absorbed dose distributions for radiotherapy photon beams.', *Med. Phys.* **31**(4), 907–913.
- Ubrich, F., Wulff, J., Kranzer, R. and Zink, K. (2008), 'Thimble ionization chambers in medium-energy x-ray beams and the role of constructive details of the central electrode: Monte Carlo simulations and measurements.', *Phys. Med. Biol.* **53**(18), 4893–4906.
- Verhaegen, F. and Das, I. J. (1999), 'Monte Carlo modelling of a virtual wedge.', *Phys. Med. Biol.* **44**(12), N251–N259.
- Verhaegen, F. and Seuntjens, J. (2003), 'Monte Carlo modelling of external radiotherapy photon beams.', *Phys. Med. Biol.* **48**(21), R107–R164.
- Walters, B. R. B., Kawrakow, I. and Rogers, D. W. O. (2007), 'DOSXYZnrc Users Manual PIRS-0794revB.', *National Research Council of Canada* .
- Wang, L. L. W. and Leszczynski, K. (2007), 'Estimation of the focal spot size and shape for a medical linear accelerator by Monte Carlo simulation.', *Med. Phys.* **34**(2), 485–488.
- Wang, L. L. W. and Rogers, D. W. O. (2007), 'Monte Carlo study of si diode response in electron beams.', *Med. Phys.* **34**(5), 1734–1742.
- Wang, L. L. W. and Rogers, D. W. O. (2008), 'Calculation of the replacement correction factors for ion chambers in megavoltage beams by Monte Carlo simulation.', *Med. Phys.* **35**, 1747–1755.
- Wang, L. and Rogers, D. (2009), 'The replacement correction factors for cylindrical chambers in high-energy photon beams.', *Phys Med Biol* **54**(6), 1609–1620.

- Wickman, G. (1974), 'A liquid ionization chamber with high spatial resolution.', *Phys Med Biol* **19**(1), 66–72.
- Williamson, J. F. (1987), 'Monte Carlo evaluation of kerma at a point for photon transport problems.', *Med. Phys.* **14**(4), 567–576.
- Yi, C.-Y., Hah, S.-H. and Yeom, M. S. (2006), 'Monte Carlo calculation of the ionization chamber response to ⁶⁰Co beam using PENELOPE.', *Med. Phys.* **33**(5), 1213–1221.
- Zink, K. and Wulff, J. (2008), 'Monte Carlo calculations of beam quality correction factors k_Q for electron dosimetry with a parallel-plate Roos chamber.', *Phys. Med. Biol.* **53**(6), 1595–1607.

List of Tables

1.1. Reference conditions for calibration and measurement.	22
2.1. Characteristics of detectors used for investigation in the field boundary.	59
3.1. Optimum cylindrical shell thickness and XCSE factor for dose and perturbation correction factor calculations	63
3.2. Calculated beam quality specifiers for the various spectra.	65
3.3. Estimated factors p_{Δ} and k_{Δ}	72
3.4. Parameters of fits to calculated data of k_Q as a function of beam quality.	72
3.5. Calculated sensitivity and final uncertainty in calculated k_Q factors. . . .	76
3.6. Differences of calculated and measured depth-dose curves.	81
3.7. Comparison of calculated and measured output-factors.	83
3.8. Needed shifts for the PTW31010 chamber as result of the χ^2 minimization.	88
3.9. Penumbra broadening for various detectors in the field of a 6 MV beam.	92

List of Figures

1.1. Tumour control probability (TCP) and the probability of normal tissue complication (NTCP).	9
1.2. Photon mass attenuation coefficient for water.	12
1.3. Illustration of the relationship between absorbed dose D and collisional kerma K_{col}	14
1.4. Concept of clinical dosimetry in radiation therapy.	15
1.5. Models of typical thimble chambers.	16
1.6. Schematic illustration of perturbation effects.	19
1.7. Illustration of geometrical reference conditions.	21
1.8. Principle of the EGSnrc system.	28
1.9. Linear accelerator head.	34
2.1. Mean free path of photons and CSDA-range of electrons in water.	38
2.2. Combination of the IPSS and XCSE techniques for the simulation of two ionization chamber positions inside a phantom.	42
2.3. Different methods for the calculation of kerma.	45
2.4. Chain for the determination of perturbation correction factors.	47
2.5. Setup for the investigation of detectors in the idealized beam penumbra.	58
3.1. Efficiency gain by the use of the XCSE-technique	61
3.2. Efficiency gain for dose and perturbation correction factor calculations as a function of beam quality.	62
3.3. Calculated distributions of kerma employing the track length estimator and dose distributions as result of DOSXYZnrc calculations.	64
3.4. Calculated perturbation correction factor p_{cel} for the central electrode of a NE2571 chamber.	66
3.5. Perturbation factor p_{stem} for the presence of a chamber stem in the NE2571 model.	67
3.6. Wall perturbation correction factor p_{wall} as a function of beam quality for the NE2571 model.	68
3.7. The product of the p_{dis} and p_{cav} factors for the NE2571.	69
3.8. Calculation of the effective point of measurement for the cavity of the NE2571	70
3.9. Relationship between the range and energy of monoenergetic electrons in air.	71
3.10. The overall perturbation and beam quality correction factors for the NE2571.	73
3.11. Influence of transport parameter settings and the simulation setup on the calculated beam quality correction factors k_Q	74
3.12. Variation of OAFs due to changes of primary electron beam parameters.	78
3.13. Difference between calculated and measured off-axis profiles for different energy spot size combinations.	79
3.14. Relative dose distribution within the 3 cm x 3 cm field.	80

3.15. Comparison of calculated and measured dose distribution of the 6 MV photon beam.	82
3.16. Changed mean energy of photons and charged particles within the 6 MV field of the Siemens KD.	84
3.17. Total correction k_{NR} in the field of the Siemens KD 6 MV beam as a function of depth and as a function of off-axis distance.	85
3.18. Calculated relative perturbation correction factors and sprs as a function of depth and of off-axis distance.	86
3.19. Perturbation factors within the build-up region.	87
3.20. Mean energy and fluence of photons and charged particles at the field boundary under CPD.	88
3.21. Spectral change for electrons in the field penumbra.	89
3.22. Individual perturbation correction factors and the f -factor for the PTW31010 in the idealized field boundary	90
3.23. Application of Spencer-Attix theory within the field penumbra.	91
3.24. Calculated deviation between dose to water and detector reading.	92
A.1. Darstellung des Buffon Nadelexperiments	102
A.2. Berechnung von π mittels Monte-Carlo Simulation	103
A.3. Rejection method bei der Stichprobenwahl	105
A.4. Monte-Carlo Simulation von Bahnspuren	107
A.5. Grundidee <i>condensed history</i>	111

List of Abbreviations

CEP	charged particle equilibrium
CPD	charged particle dis-equilibrium
CS	correlated sampling
CSDA	continious slowing down approximation
GUM	Guide to the expression of uncertainty in measurement
IMRT	intensity modulated radio-therapy
IPSS	intermediate phase-space scoring
MC	Monte Carlo
mfp	mean free path
OAF	off-axis factor
PDD	percentage depth dose
RR	Russian Roulette
rr	range rejection
sprs	stopping-power ratios
VRT	variance reduction technique
XCSE	photon cross section enhancement

Danksagung

Mein Dank gilt Prof. Dr. Dr. Johannes T. Heverhagen für seine Unterstützung und Betreuung. Mit der Übernahme des Referats und der entsprechenden Vertretung der Arbeit vor der Fakultät, ist mir der Weg hierhin erst ermöglicht worden. Ich danke ihm für sein Vertrauen in meine Arbeit und seine Offenheit gegenüber der Thematik.

Herrn Prof. Dr. Klemens Zink danke ich besonders für seine Art, mir auf dem Weg der Promotion wirklich alles zu ermöglichen. Er hat für ein Umfeld gesorgt, in dem ich frei und unbeschwert der wissenschaftlichen Arbeit nachgehen konnte. Neben der fachlichen Betreuung, war vor allem sein Optimismus und sein Tatendrang eine große Hilfe. Seinem Einsatz verdanke ich im Wesentlichen mein bisheriges wissenschaftliches Vorankommen in der Welt der Medizinischen Physik.

Durch Dr. Iwan Kawrakow habe ich die in jeder Hinsicht 'effiziente' Arbeitsweise kennengelernt. Den durch ihn ermöglichten und angenehmen Aufenthalt am National Research Council in Kanada betrachte ich fachlich wie auch persönlich als die große Bereicherung für meine wissenschaftliche Tätigkeit. Dem EGS-Team in Ottawa danke ich für die herzliche Aufnahme in die Arbeitsgruppe während der Zeit am IRS.

Meinem Freund und Kollegen Ralph Schmidt (GM) möchte ich für eine schöne Zeit in Gießen danken. Oft genug war er mir eine Hilfe, wenn ich nicht mehr weiter wusste. Die gemeinsame Arbeit am GMctdospp-Projekt war eine große Freude.

Dem Freund und Kollegen David Jany verdanke ich, dass ich nicht noch weitere Jahre auf die Simulationsergebnisse warten muss. Seine ständige und bedingungslose Hilfsbereitschaft hat viel zu meiner Arbeit beigetragen.

Frank Ubrich danke ich für eine erfolgreiche Zusammenarbeit während seiner Diplomarbeit am IMPS und vor allem seinem kritischen Blick auf diese Arbeit.

Allen anderen Kollegen aus dem IMPS und der Marburger Arbeitsgruppe danke für schöne gemeinsame Zeit. Viele lustige Stunden verdanke ich Logi Tsogtbatat. Prof. Martin Fiebich bewundere ich nach wie vor für die gute Laune um 7 Uhr morgens. Auch den vielen Diplomanden, die mir in den letzten Jahren über den Weg gelaufen sind, sei gedankt. Christian Müller war bei den initialen Versionen des KD Modells eine sehr große Hilfe. Weitere Diplomanden, die ich während der Zeit betreut und von denen ich eine Menge gelernt habe: Iva Cenova, Steve Braun, Petar Penchev, Rainer Mett, Florian Rosam, Jakob Tertel, Andre Toussaint.

Rafael Kranzer und Dr. Edmund Schüle danke ich für die Beantwortung aller Fragen zu PTW-Ionisationskammern und das damit verbundene Vertrauen. Heiko Karle gilt besonderer Dank für die Messungen am KD und die Abfahrten in Pichl. Dr. Kapsch sei für die Bereitstellung des berechneten Co60-Spektrums der PTB Anlage gedankt.

Herrn Prof. Jacob und Herrn Prof. Lill vom Institut für Zytobiologie danke ich für ihre Bereitschaft, mir den Zugang zum Kern- und Fachmodul zu ermöglichen. Der von ihnen gewährte, sehr schöne Einblick in die Welt der Zellbiologie wird mir in sehr guter Erinnerung bleiben. Ich danke weiterhin Frau Dr. Kutschenreuter bei ihrer Hilfe, die organisatorischen Hürden zu bewältigen.

Jill danke ich für viel Geduld und Verständnis, vor allem an Wochenenden abseits der Teilchen. Meinen Eltern und meiner Familie danke ich für alles bis hierher.

Publikationsliste

Teile dieser Arbeit, sowie methodische Ansätze wurden in wissenschaftlichen Artikeln und auf Konferenzen vorgestellt:

peer-reviewed journals

Wulff J., Heverhagen J.T. & Zink K. Monte-Carlo-based perturbation and beam quality correction factors for thimble ionization chambers in high-energy photon beams. *Phys. Med. Biol.*, 2008, 53, 2823-2836

Wulff J., Zink K. & Kawrakow I. Efficiency improvements for ion chamber calculations for high energy photon beams. *Med. Phys.*, 2008, 35(4), 1328-1336

Wulff J., Jany D. & Zink K. Quantitative determination of cutoff perturbation factor p_{Δ} in the DIN 6800-2 (2008) by means of Monte Carlo simulations. *Z. Med. Phys.*, 2008, 18, 203-210

Wulff J., Karle H., Heverhagen J.T. & Zink K. Investigation of correction factors for non-reference conditions in ion chamber photon dosimetry with Monte-Carlo simulations *Z. Med. Phys.*, 2009, *accepted for publication*

Wulff J., Heverhagen J.T., Kawrakow I. & Zink K. Investigation of systematic uncertainties in Monte Carlo calculated beam quality correction factors, *Phys. Med. Biol.*, 2009, *accepted*

conference proceedings

Wulff J., Schmidt R., Fiebich M., Zink K., & Heverhagen J.T. Fast kerma-based patient dose calculations in diagnostic radiology using EGSnrc, *American Association of Physicists in Medicine 51st Annual Meeting*, 2009

Wulff J., Heverhagen J.T., Kawrakow I. & Zink K. Investigation of systematic uncertainties in Monte Carlo calculated beam quality correction factors, *European Workshop on Monte Carlo Treatment Planning*, 2009, *accepted*

Wulff J., Heverhagen J.T. & Zink K. 2008 Simulationsbasierte Methoden zur Ermittlung des Messorts von zylindrischen Ionisationskammern in der Referenzdosimetrie. *Medizinische Physik 2008 - Tagungsband*, Oldenburg, 2008

Wulff J., Ubrich F., Heverhagen J.T. & Zink K. Monte Carlo based investigation of ionization chamber wall perturbation factors for high energy photon beams. *Radioth. Oncol.*, 2007, 84, 113

Wulff J., Heverhagen J.T. & Zink K. Simulation der Tiefendosis im Aufbaubereich hochenergetischer Photonenstrahlung mit luft- und flüssigkeitsgefüllten Ionisationskammern *Medizinische Physik 2007 - Tagungsband*, Bern, 2007

weitere Publikationen im Zusammenhang mit der bearbeiteten Thematik

Zink K., Altintas S., Poppe B. & **Wulff J.** Positioning recommendations for parallel-plate ionization chambers in clinical electron beams according to different dosimetry protocols - a Monte Carlo study for three different chamber types. *AAPM 51st Annual Meeting*, 2009

Tertel J., **Wulff J.**, Karle H., & Zink K. Verification of a commercial implementation of the Macro Monte-Carlo electron dose calculation algorithm using the virtual accelerator approach. *Z. Med. Phys.*, 2009, *under review*

Zink K. & **Wulff J.** Positioning of a plane-parallel ionization chamber in clinical electron beams and the impact on perturbation factors. *Phys. Med. Biol.*, 2008, 54, 2421-2435

Schmidt R., **Wulff J.**, Kästner B., Jany D., Heverhagen J.T., Fiebich M. & Zink K. Monte Carlo based calculation of patient exposure in X-ray CT-examinations, *IFMBE Proceedings 22*, 2008, pp. 2487-2490

Keil B., **Wulff J.**, Schmidt R., Auwanis D., Danova D., Heverhagen J.T., Fiebich M., Madsack B., Leppek R., Klose K.J. & Zink K. Protection of eye lens in computed tomography-dose evaluation on an anthropomorphic phantom using thermo-luminescent dosimeters and Monte-Carlo simulations. *RöFo*, 2008, 180, 1047-1053

Zink K. & **Wulff J.** Monte Carlo calculations of beam correction factors k_Q for electron dosimetry with a parallel plate Roos chamber. *Phys. Med. Biol.*, 2008, 53, 1595-1607

Ubrich F., **Wulff J.**, Kranzer R. & Zink K. Thimble ionization chambers in medium energy X-rays and the role of constructive details of the central electrode: Monte Carlo simulations and measurements. *Phys. Med. Biol.*, 2008, 53, 4893-4906

Wulff J., Keil B., Auwanis D., Heverhagen J.T., Klose K.J. & Zink K. Dosimetrische Evaluation von Augenlinsen-Protektoren in der Computertomographie - Messungen und Monte Carlo Simulationen. *Z. Med. Phys.*, 2008, 18, 19-26

Wulff J. Monte Carlo Simulationen für die Dosimetrie in der Strahlentherapie. XX. *Winterschule für Medizinische Physik, Pichl*, 2008 (*eingeladener Vortrag*)

Wulff J. & Zink K. Dosimetrie unter Nicht-Referenzbedingungen: Untersuchungen mittels Monte-Carlo Simulationen. 242. *PTB-Seminars "Klinische Dosimetrie mit Ionisationskammern nach der neuen Norm DIN6800-2 (2008)"*, Braunschweig, 2008 (*eingeladener Vortrag*)